

MAGYAR ÁLLAMI
EÖTVÖS LORÁND
GEOFIZIKAI INTÉZET

GEOFIZIKAI KÖZLEMÉNYEK

ВЕНГЕРСКИЙ
ГЕОФИЗИЧЕСКИЙ
ИНСТИТУТ
ИМ Л. ЭТВЕША

ГЕОФИЗИЧЕСКИЙ
БЮЛЛЕТЕНЬ

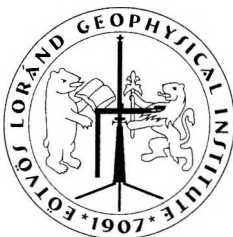
GEOPHYSICAL

TRANSACTIONS
EÖTVÖS LORÁND GEOPHYSICAL INSTITUTE OF HUNGARY

CONTENTS

- Well-logging methods to investigate a granitic site for radioactive waste deposition *L. Zilahi-Sebess* 51
- Theoretical and statistical investigation of elemental concentration distributions determined by laser-induced plasma atom emission spectra on geological samples *L. Andrassy, L. Zilahi-Sebess, L. Vihar* 95

VOL. 44. NO. 2. FEBRUARY 2003. (ISS N0016-7177)



TARTALOMJEGYZÉK

Mélyfúrás-geofizikai módszerek a gránitba telepített radioaktív hulladék-tároló vizsgálatára	<i>Zilahi-Sebess L.</i>	92
Geológiai mintákon mért lézer-indukált plazma atom emissziós spektrumokból számított szelvény illetve terület menti elem koncentráció eloszlások elméleti és statisztikai vizsgálata	<i>Andrássy L., Zilahi-Sebess L., Vihar L.</i>	135

Well-logging methods to investigate a granitic site for radioactive waste deposition

László ZILÁHI-SEBESS*

In this study the facilities of well logging methods will be presented in a geological investigation of a possible site for the deposition of low and intermediate level nuclear waste. The well logging measurements were accomplished in sedimentary cover in granite, in the weathered crust of granite, and in fresh granite. Apart from the conventional well logging methods two new measurement methods in Hungary (outside the oil sector) — Acoustic Borehole Televiwer (BHTV) and Heat Pulse Flowmeter (HPF) — are introduced. In the sedimentary cover of the granite the cyclic variation of electrical resistivity in the Pleistocene loess sequences are linked with paleoclimatic changes. Within the loess sequences, identification of paleosoil horizons is based on magnetic susceptibility. In granite the grade of consolidation may be described by the depth trends of geophysical parameters such as I_p and I_s , which depend on the elastic parameters and resistivity. Characterization of fractured zones and the lower part of the weathered crust of granite is based on the statistical and spatial distribution of physical parameters and the fracture indications (dips and azimuths) of the BHTV. The heat pulse flow measurement may indicate small inflows not susceptible to the sensitivity of conventional flowmeters (under 1/min). The geological correlation between the wells was demonstrated within the Quaternary sequence and in the weathered crust of granite. In the weathered part of the granite the correlation is less characteristic for the thickness of the correlation units between the wells than it is in sediments, because the zones of it are not really defined layers: they do not have sharp and slowly changing boundaries in space, and their thickness may fluctuate to a considerable extent between any given two wells.

Keywords: well-logging, radioactive waste, granites, fracture zones

1. Introduction

The deposition of hazardous wastes, especially of radioactive waste is a worldwide problem. To prevent environmental contamination dangerous waste must be isolated by means of natural and artificial barriers — a so called multibarrier system. First of all, *natural barrier* means the geological environment, in which the main task is to investigate the hydrogeological properties of the chosen radioactive waste disposal site. With the aid of

* Eötvös Loránd Geophysical Institute of Hungary, H-1145 Budapest, Kolumbusz u. 17-23
Manuscript received: 8 Nov. 2000.

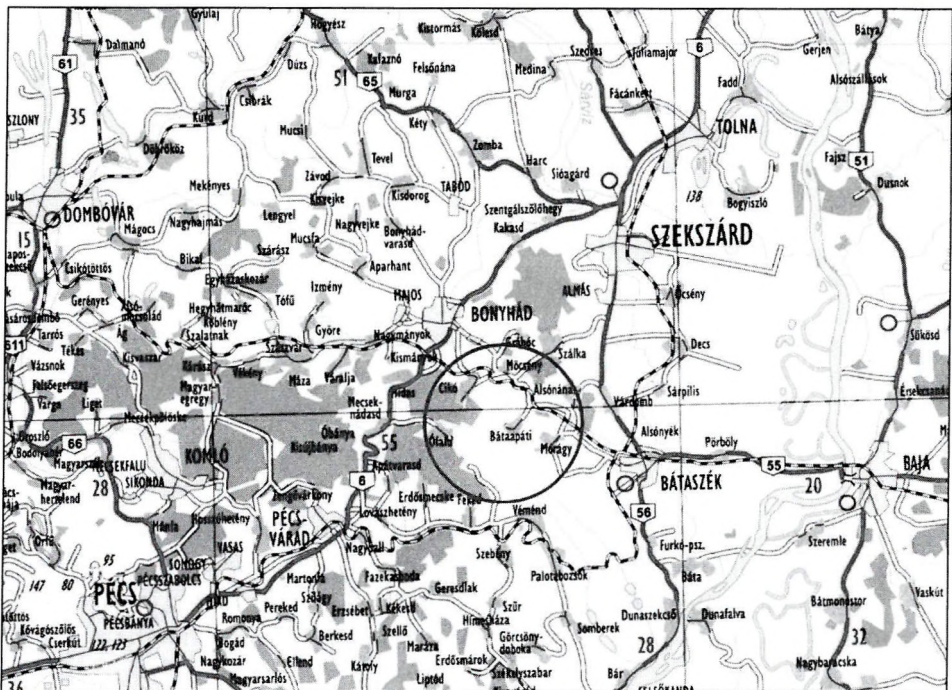
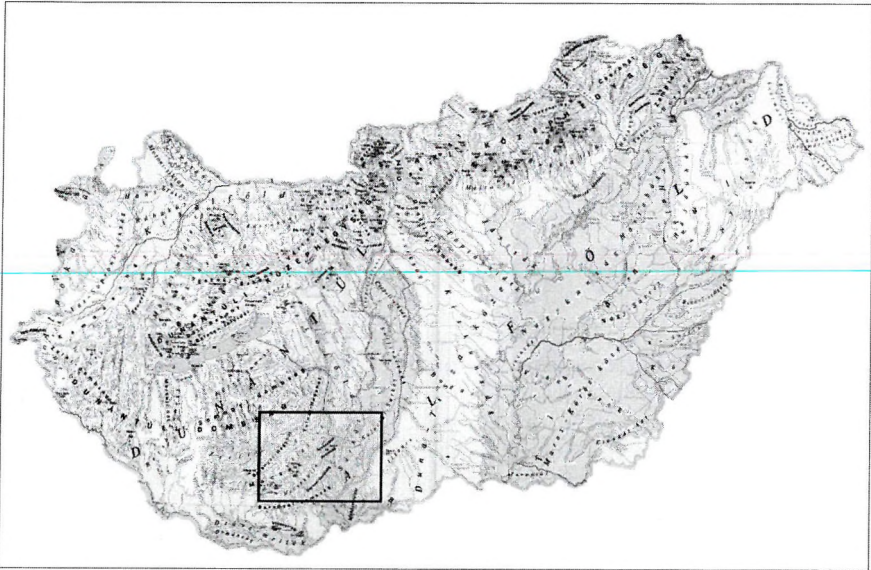


Fig. 1. Location of the investigated area for low and intermediate nuclear waste repository
 1. ábra. A kis és közepes radioaktivitású erőművi hulladék elhelyezésére irányuló földtani kutatás területe

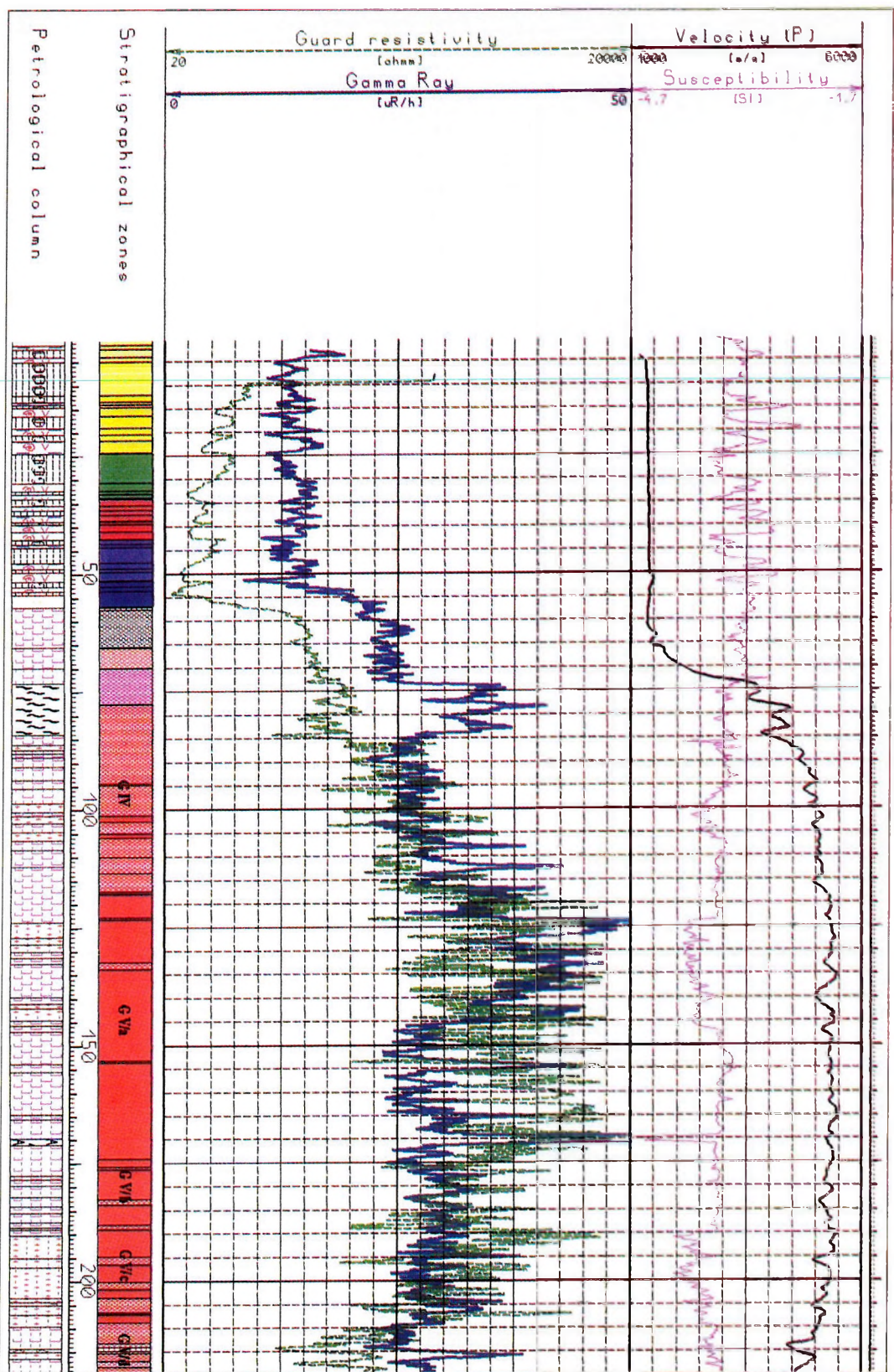


Fig. 2. Average lithological column with four characteristic logs
2. ábra. Átlagos rétegsor négy jellemző mérésgörbével

well logging methods information can be gained on the in situ fracturization and on the elastic parameters of the local rock.

Hungary's only nuclear power plant (situated at Paks) provides a significant part of the country's energy production. In addition to the plant's safe operation there is the problem of the safe disposal of the radioactive waste. After completing a regional screening survey for suitable disposal sites the southern part of the country was chosen for further investigations.

According to the technical literature four types of geological formations may be suitable for the deposition of radioactive waste: salt rocks, crystalline rocks, volcanic tuffs and clays. Most of Hungary's territory is covered by Tertiary and Quaternary sediments. The basement outcrops are mainly carbonates, which are not suitable for waste disposal. Recent investigations show that a crystalline rock—the so called Mórág granite—is the most suitable place in Hungary to locate a radioactive waste repository (*Fig. 1*). Loess which was deposited during Pleistocene covers the Mórág granite to a depth of 40–60 m. The granite outcrops can be found only in the valleys of the survey area. The average thickness of weathered granite is about 60 m beneath the sedimentary overburden. In contrast to northern Europe which was covered by ice in the Pleistocene there was no glacial erosion here and the uppermost 10–20 m thick part of the weathered zone consists of autochthonous sand, gravel, debris and breccia. Therefore in this area three potential fluid conducting zones should be considered: porous zones in loess, the weathered zone in the upper part of the crystalline rock, and the fractured zones within fresh crystalline rock (*Fig. 2*).

During the geological investigation of the Üveghuta site for the disposal of low and intermediate level (L/IL) radioactive waste, ELGI and Geo-Log Ltd. were commissioned to carry out well-logging measurements and their interpretation. Borehole Üh-1 was the first borehole in the area investigated by well logging methods for surveying granitoid rocks [BUCSI et al. 1997]. When carrying out this work we succeeded in developing a well-detailed image on the Quaternary loess sequence, the alteration cover of the granite, and the fissured zones of the fresh granite.

Sectioning of the granite's weathered crust and fresh granite from the geotechnical viewpoint was primarily based on acoustic and electric measurements [ZILAHÍ-SEBESS et al. 1998].

2. Short lithological descriptions of the formations

As was mentioned in the Introduction the main units of the simplified lithological column are:

- a) Sedimentary rocks above Palaeozoic granite
- b) Weathered zone of granite
- c) Fresh granite

Following is a short description of the zones penetrated by the borehole from the viewpoint of well logging parameters (*Fig. 3*):

0.0–53.0 m Loess layers of Pleistocene age (A1 – D) (yellow, green, red, and blue)

Resistivity and neutron-porosity vary periodically as a function of depth; the density increases downwards as a consequence of consolidation. These cycles on logs may be related to the climatic variations in the Ice Age.

53.0–56.0 m Terrestrial clay (E) (dark blue)

*

Based on the well logging parameters the weathered zone of the granite can be divided into four subzones:

- G I granite gravel, granite sand (grey)
- G II fragments and breccia (light orange)
- G III chemically altered and highly fractured granitoid rocks (pink)
- G IV granite with weak alterations caused by weathering (light red)

56.0–77.6 m Upper part of the weathered zone (G I–G III)

The crystalline rock was exposed and weathered during a period of geological history. The physical parameters in this weathered zone show a downward variation similar to the compaction trend of unconsolidated sediments though these changes in parameters are certainly more abrupt and they are not so closely correlated with depth like the compaction trend of unconsolidated sediments.

In subzone G III resistivity and shear wave velocity vary relatively rapidly with depth.

77.6–114.0 m Lower part of the weathered zone (G IV)

Rocks in the subzone G IV are only slightly affected by surficial weathering. The lower part of the subzone is a hard, fractured and altered formation where shear waves may also be generated. Shear wave velocity and resistivity increase slowly downwards: this increase demonstrates that it belongs to the weathered zone.

Petrological column

Stratigraphical zones

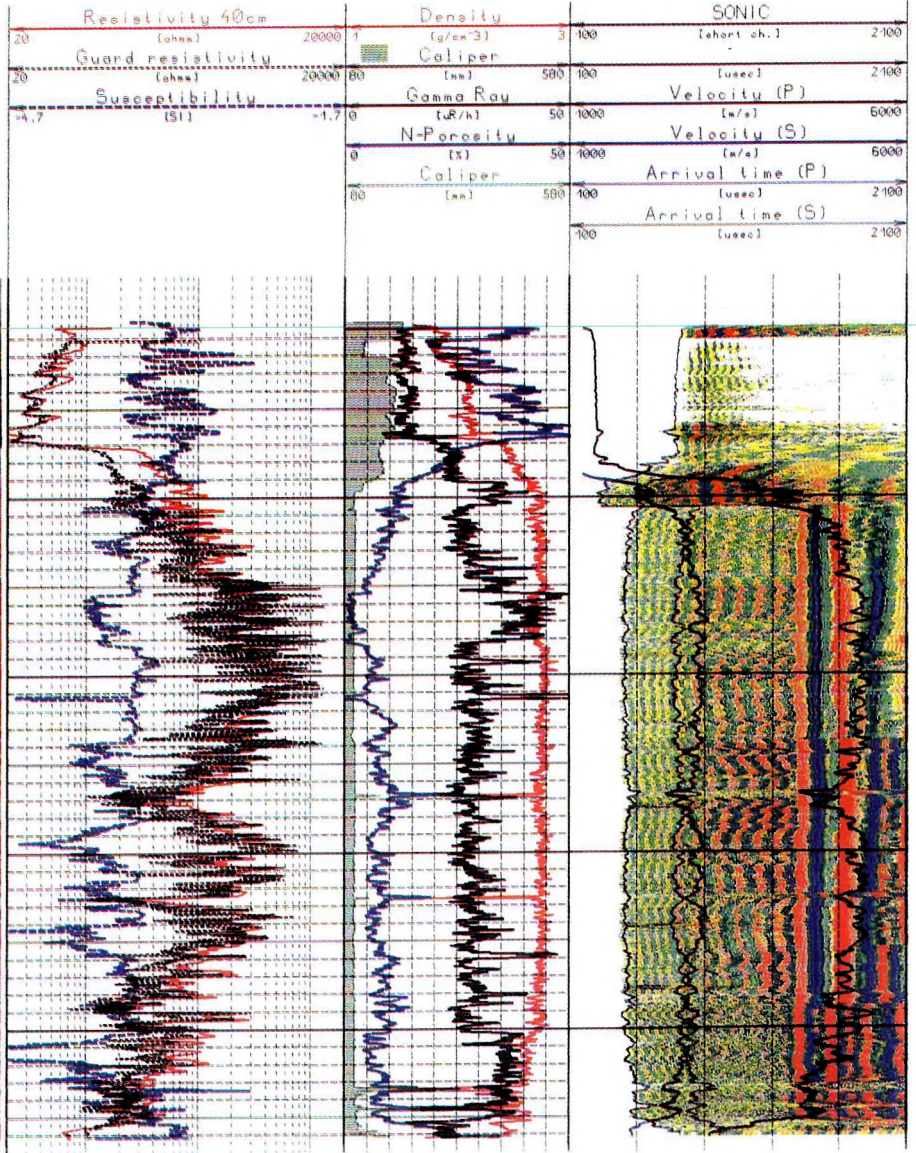
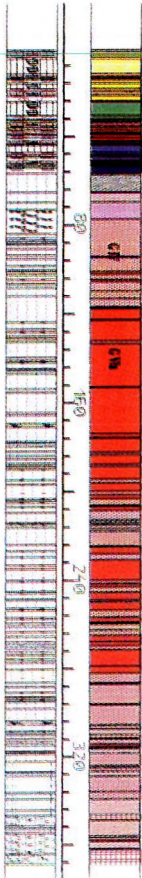


Fig. 3. The most important well logs and a simplified lithological column
3. ábra. A legfontosabb mérések és az egyszerűsített litológiai oszlop

114.0–365.0 m Fresh granite formation (G V) (red)

This granite is free of surface effects, in which physical parameters do not depend on depth. Fractured and crumbled zones are the primary targets of investigation in subzone G V. Characteristic of the faults associated with a crumbled zone is that both resistivity and acoustic velocities tend to decrease at a distance of more than 10 m away from the fault. BHTV logs verified that the number of closed fractures decreases with increasing distance from the fault. The statistical distribution of dip azimuths is characteristic of the fault zone.

3. Well logging investigations

The following measurements were performed in each borehole: SP, 10 cm and 40 cm resistivity, IP, natural gamma, density, neutron-porosity, full waveform acoustic (the sonde length was 100 and 150 cm in the overburden, 200 and 250 cm in the granite), acoustic borehole televiewer (BHTV), caliper, temperature, inclinometry, differential temperature and Heat Pulse Flowmeter (HPF). Only the most important logs are shown in the figure (Fig. 3).

Acoustic borehole televiewer measurement, which outside the oil industry is considered a new method in Hungary, allows high resolution, in situ study of the fissure system. With the borehole televiewer the travel time and amplitude of the signal from a rotating sonar (sonic transmitter) is measured in minimum 72, maximum 288 directions. In order to plot the result with a colour code the borehole wall's image is obtained laid out in a plane. In the image constructed from the travel times of the reflections only the fractures open from the acoustic viewpoint can be recognized, while in the image constructed from the amplitudes of reflections all those forms can be seen which have elastic parameters different from their surroundings, thus the filled in fractures as well. Therefore the amplitude image is a more variegated travel time image (Fig. 4).

In general, the amplitude image is richer in detail, the fissures — closed from the acoustic viewpoint — appear as white sinusoids in this image only (right column), while in the travel time there is no indication of them (Fig. 4). The larger open fissures appear in the travel time image (left column) as black sinusoids and as white sinusoids on the amplitude image

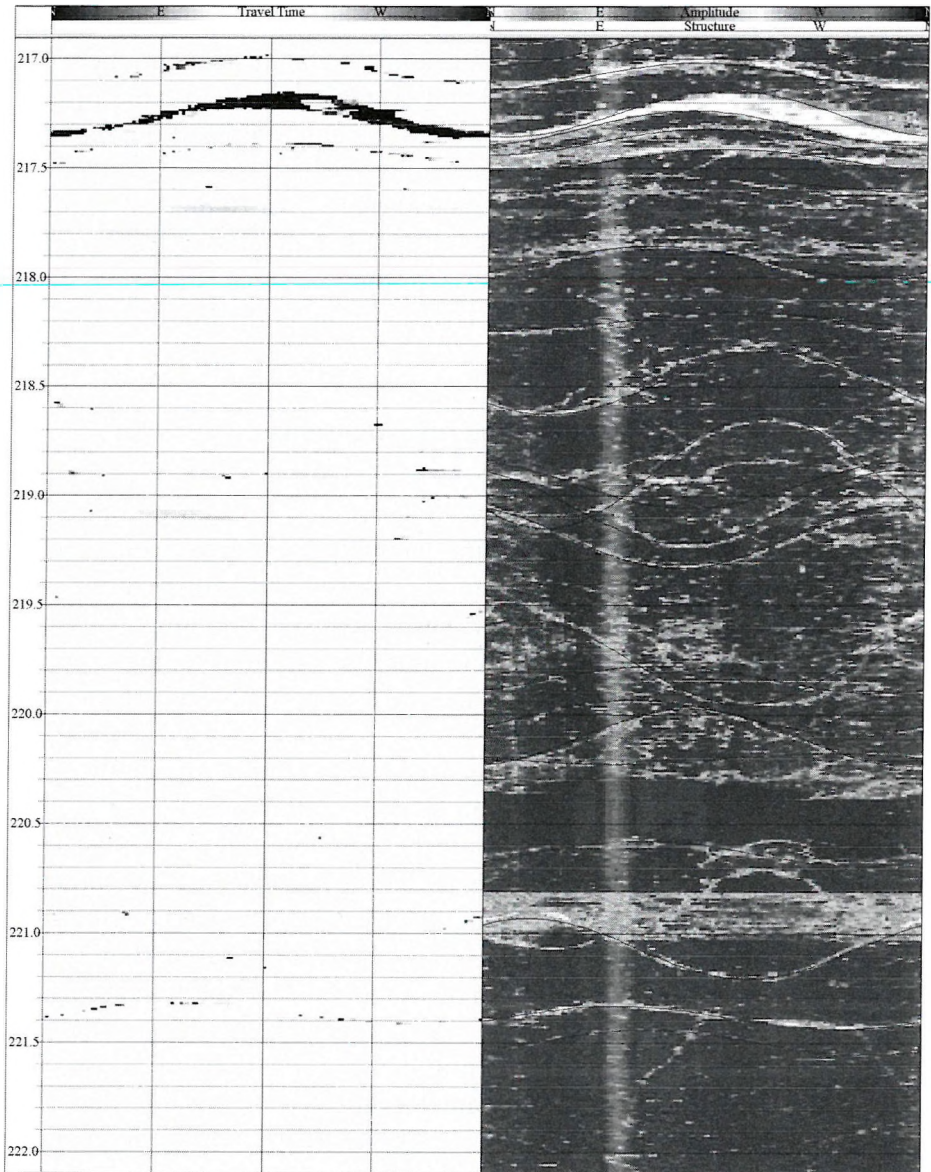


Fig. 4. BHTV travel time and amplitude images

4. ábra. BHTV reflexió idő és amplitudó kép

between 217.0 and 217.5 m. Some other narrow open fissures can be seen in the travel time image as a row of black dots and as continuous white sinusoids in the amplitude image (e.g. at 221.35 m)

Fissures are ranked into the following four categories based on the BHTV images:

- closed fissures providing a complete sinusoidal;
- open fissures providing a complete sinusoidal;
- thin (intersected) fissures providing an incomplete sinusoidal;
- patch-like and thick short sinusoidal parts.

These categories were used for statistical processing of fissure directions obtained from BHTV measurements. Only those fissured zones are considered real fracture zones where a large number of open fissures can be seen on the BHTV reflection time image.

The Heat Pulse Flowmeter is a special tool which operates with heat pulses emitted by a transmitter as a means of determining small influxes. The arrival time of a given heat pulse is measured at two (upper and lower) detectors. From the travel time of the heat pulse, the logging speed can be calculated; from the caliper of the borehole, the influx can be calculated. These measurements were performed at every meter. The accuracy of this tool is about 0.1–0.2 l/min (*Fig. 5*).

The HPF logs were recorded in each borehole, the locations of the inflow and the rate of inflow were determined by means of the log. In addition to the HPF log, the most important fracture indicators — caliper, electrolog, full waveform acoustic log, BHTV — are shown in this figure. It can be seen that the inflows are not from the largest fractures. For example, the wide fracture at 214 m, does not produce any inflow, although it is an open fracture according to *Fig. 6*.

3.1. Well logging in the sedimentary cover of granite

The study of sedimentary rocks above Paleozoic granite as a part of the hydrologic system is of considerable importance. The log set measured in the wells drilled in the sedimentary environments was: self potential, resistivity measured with 10 cm and 40 cm long normal tools, guard laterolog, natural gamma ray, neutron-porosity, gamma-gamma density, longitudinal and transversal wave velocities (V_p and V_s), full waveform acoustic (SONIC), magnetic susceptibility, temperature, differential temperature, and caliper. Because of the groundwater level (approximately 80–85 m depth) in the weathered zone of the granite some of the measurements encountered difficulties. The resistivity logs proved to be the best tools for tracing the large scale paleoclimatic cycles and the porous zones within the

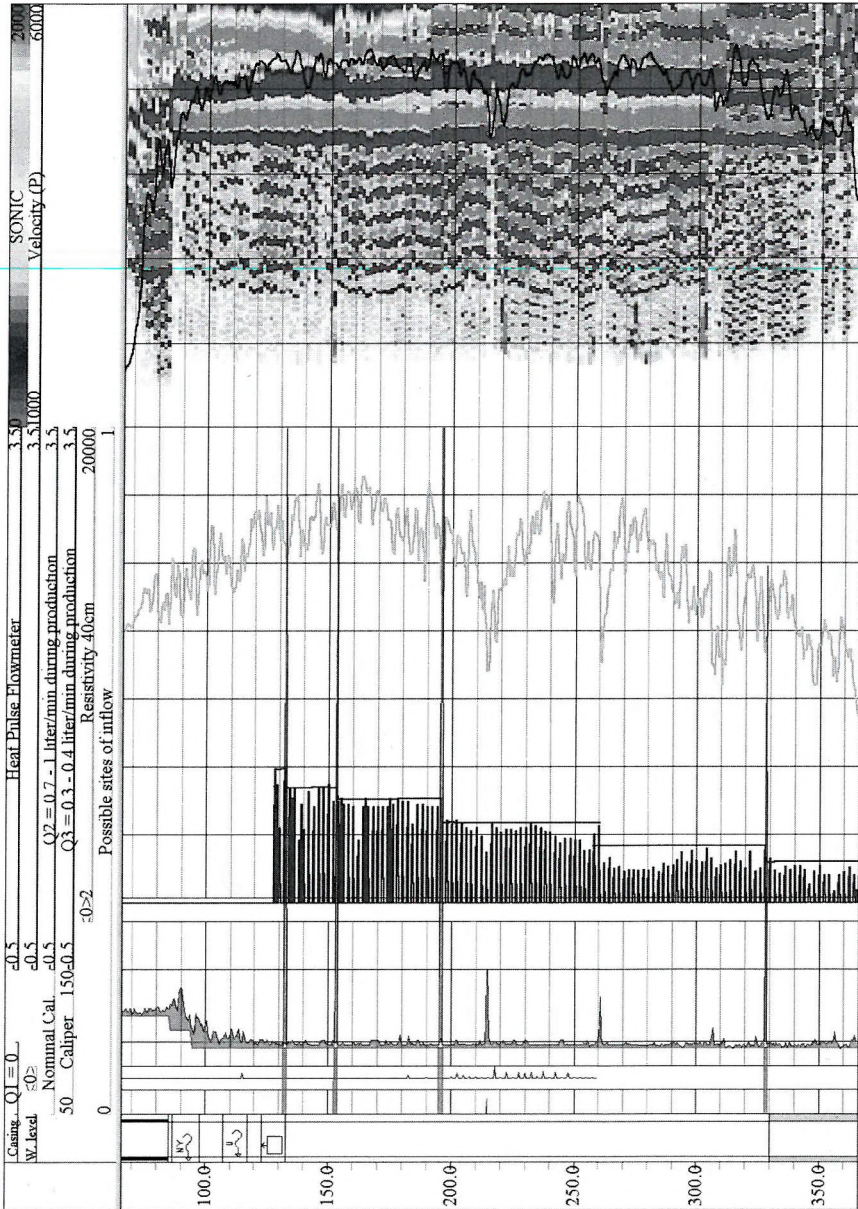


Fig. 5. The evaluated result of heat pulse flowmeter with resistivity and full acoustic waveform

5. ábra. A hőimpulzusos áramlásmérő szonda kiértékelt mérése az elektromos ellenállással és az akusztikus hullámképpel

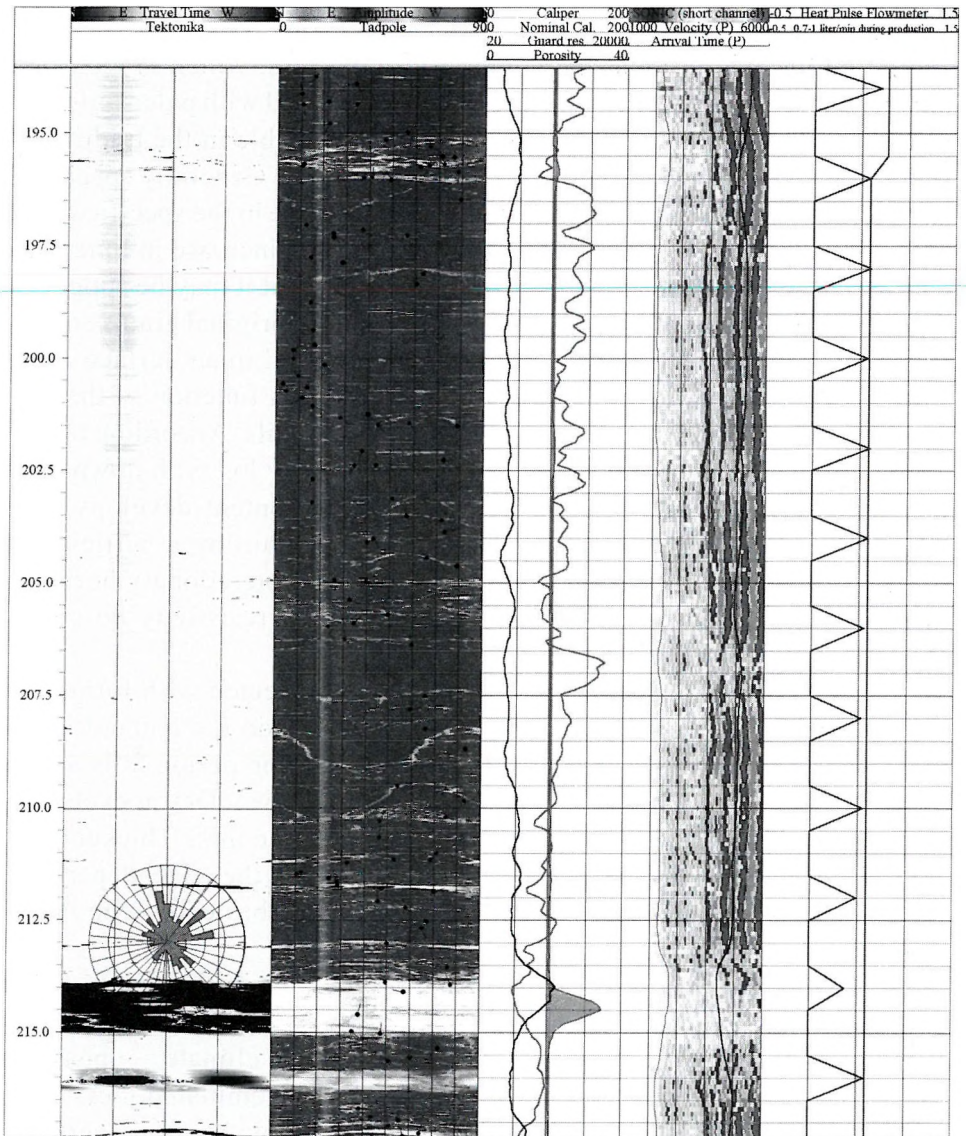


Fig. 6. Inflows and fracture sensitive measurements

6. ábra Beáramlások és repedés-érzékeny mérések

sediments. Paleosoil zonation can be done most effectively by means of magnetic susceptibility.

The electric resistivity in the Pleistocene loess sequence shows cyclic variations as a function of depth at several places [ZILAHY-SEBESS et al. 2000], thus at Üveghuta as well (Fig. 7). The shape of these cycles re-

sembles regression cycles because the electrical resistivity increases with depth. Taking into account the eolian origin of loess, which is modified only by subsequent geochemical alterations associated with paleosoils, upward coarsening of grain size distribution is impossible in the traditional sense of the term (as in the case of regression cycles). Generally speaking, any increase in resistivity is connected with a decrease in the specific internal surface. In this case it can also be linked with an increase in lime content. Because of the easy solubility of the lime content it may be supposed that a significant part of it forms a coating around the original grains and intergranular cementing material. It makes the original inner surface more smooth. The lime content decreases downwards as a function of the distance from the lime accumulation horizon of fossil soils. According to this a complete cycle recognizable in electrical resistivity log with downward increasing clayey character and decreasing lime content develops only when the paleosol concretionary horizon is underlain by a sufficiently thick loess sequence. Otherwise, if the calcareous concretionary horizons in paleosol were underlain by clay, due to its low resistivity no cyclic change similar to the experienced one could be seen.

Cyclic changes in electrical resistivity are connected with formation periods of thicker loess layers, but their boundaries do not coincide with them. While the lower boundary of the loess formation period falls on the top of a paleosol horizon, the lower boundary of a geoelectric cycle follows the surface of the lime accumulation belonging to this. Thicker loess sequences accumulated in periglacial areas during the glacial periods, therefore cyclic changes in resistivity are connected basically with large-scale climate changes in the Pleistocene age.

For stratigraphic division of Pleistocene loess identification of fossil soils as climate indicators is important [FLORINDO et al. 1999]. Paleosoils developed during the interglacial periods of milder climate — possibly during the interstadial phases — over the earlier accumulated loess, thus each of them can be considered as a chronostratigraphic horizon, therefore their identification is essential from the viewpoint of tectonic interpretation as well.

Magnetic susceptibility of sedimentary rocks is very diversified depending on the fraction which is the main carrier of magnetizability. In sedimentary rocks, thus in soils too, hematite occurring in the clay fraction is frequently the main magnetizable mineral and not the magnetite in the silt fraction. Hematite grains of micron size constitute superparamagnetic

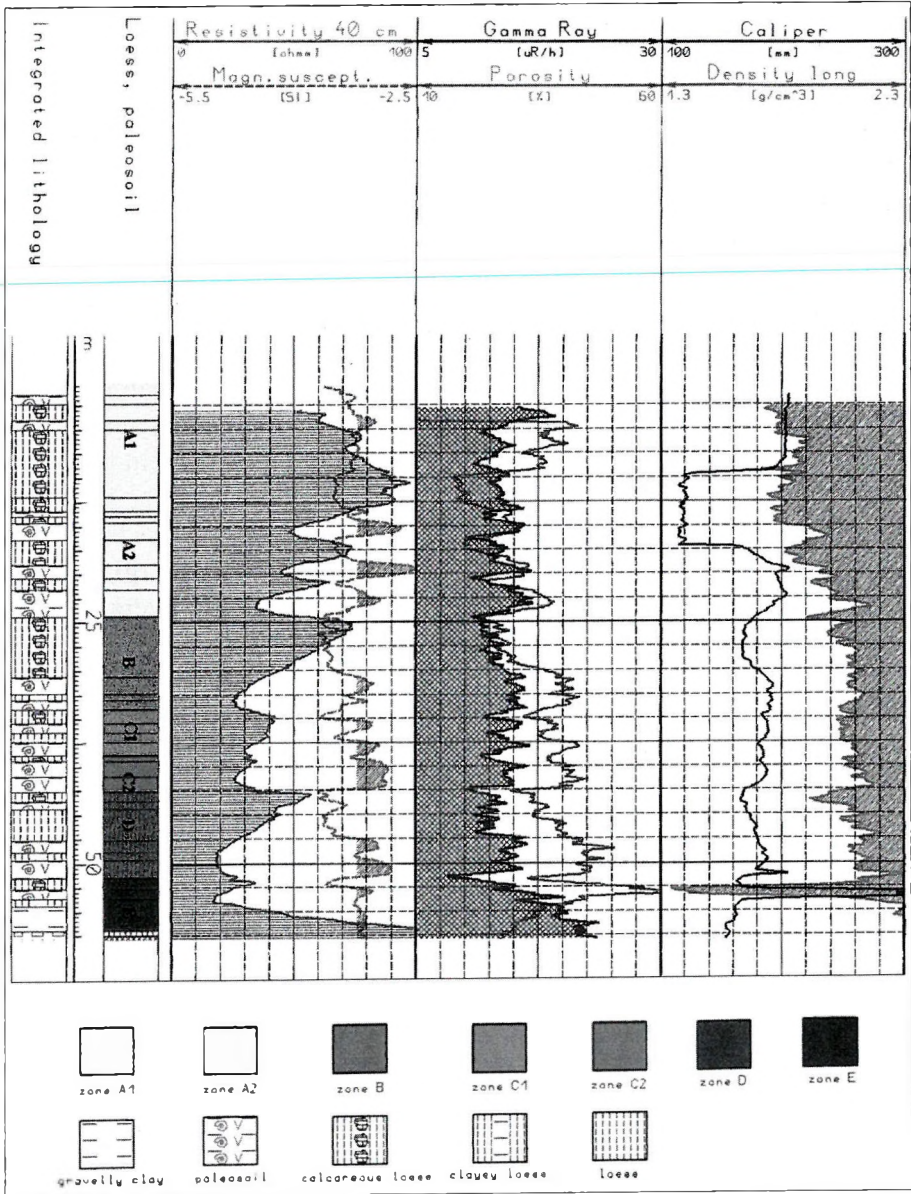


Fig. 7. Cyclic variations of electrical resistivity in Pleistocene loess sequence and paleosol identification based on magnetic susceptibility

7. ábra. Az elektromos ellenállás ciklikus változásai a Pleisztócén lösz összetételben és a paleotalaj azonosítása mágneses szuszceptibilitás alapján

particles of single-domain in clay therefore its magnetizability is relatively high [O'REILLY 1984]. Based on comparison with the geological layer sequences upper, 'A' and 'B' horizons of fossil soils (soil genetic horizons) in the loess sequence give a positive magnetic anomaly; the magnetizability of horizon 'C' — which is the horizon of lime accumulation — does not differ from that in other part of loess.

Loess itself hardly contains magnetic minerals (its magnetizability is about $3-5 \cdot 10^4$ SI unit), thus paleosoils magnetizable to almost one order of magnitude higher degree give in magnetic susceptibility log a characteristic positive anomaly (Fig. 7).

The cyclic repetition identifiable in the resistivity logs can be recognized with more difficulty or cannot be identified at all in the magnetic susceptibility log, although it is precisely this kind of measurement that is the most suitable for detecting fossil soils. There may be as many as 15–18 paleosoils, i.e. many more than those of the major periods of loess formation, because more soil forming cycles might exist within one interglacial period. Due to climatic fluctuations it could be interrupted by several more or less cooler, short periods of loess accumulation which were unfavourable for soil formation, thus soil formation within the same interglacial period was not continuous. The phenomenon might be associated with the quick changes in climate (flip-flop mechanism) within the interglacial and interstadial periods (such changes might take place partly during the glacial periods as well) [MAZAUD et. al 1999]. If the loess falling period was short and meanwhile erosion also occurred, the loess that had accumulated over the older soil might be completely soilified during the next break in loess formation. As a result, the paleosoils formed within the same interglacial period practically directly overlie each other due to the soilification during erosion and represent the lower, low resistivity part of the period identifiable on the electric resistivity log.

The situation is made more complicated by the fact that the paleosoils may also overlie each other when the layer sequence is not completely continuous due to landslides or to a hidden erosion horizon. These latter layer disturbances can frequently be deduced only from correlation between the wells. Summarizing, magnetic susceptibility measurement is suitable for identifying such changes of short period which otherwise could be only hardly or absolutely not distinguished by other measurement.

The calcareous concretionary horizons (Fig. 8) in loess may be thought of as analogous with the calcareous soil genetic horizons 'C' of pa-

Integrated lithology

Loess, paleosol

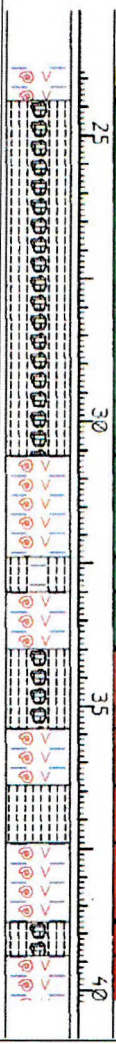
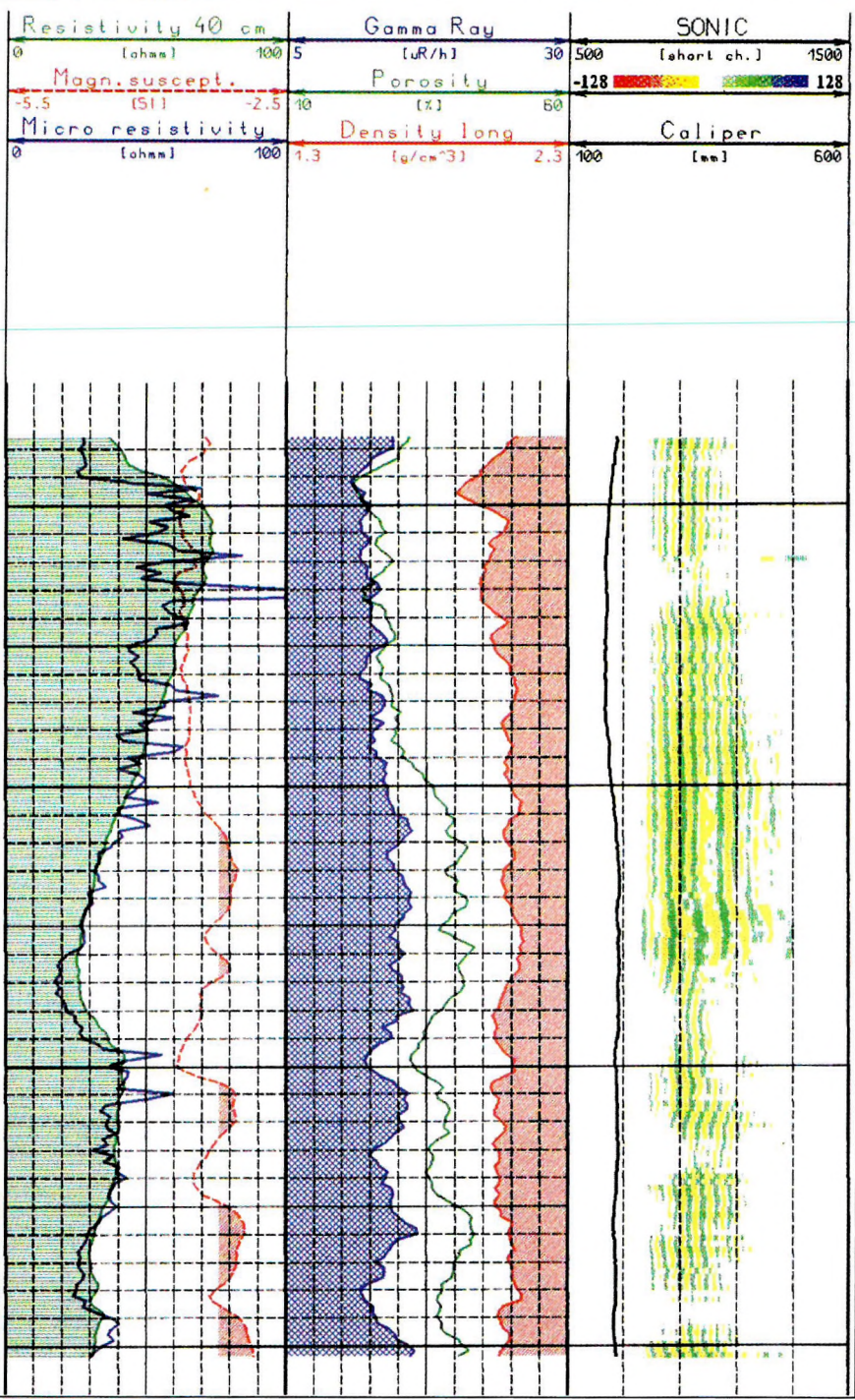


Fig. 8. Identification of calcareous horizons of loess with microresistivity tool
8. ábra. A lösz mészkonkréciós szintjeinek azonosítása mikroellenállás mérés alapján

leosoils. The effective porosity of the calcareous concretionary horizons closing the cycle is relatively high therefore it is possible that the changes in density are opposite to those of electrical resistivity. Supposedly, compaction within one cycle is stronger in less calcareous formations. This difference in compaction can be explained by the density increasing downwards in some cases within one and the same cycle. This effect can be observed in spite of the fact that increase in diameter and cavern formation at clayey sections have just the opposite effect, because due to these the measured apparent density could be lower than a real one, and the effect of the larger caverns cannot be successfully corrected completely.

Similarly to electrical resistivity neither can the individual paleosoil horizons be identified based on neutron porosity. Neutron porosity is higher in the moisture-holding layers than in the more easily drying-out calcareous layers. Due to the clay content of paleosoils their natural gamma radiation level is relatively higher than that of loess; the clay content, however, cannot always be separated easily from the non-calcareous-concretionary loess.

Sequences containing calcareous concretionary horizons separate from their vicinity with a negative anomaly of the gamma ray intensity. The very thin horizons, however, can be detected solely by microresistivity measurement (sonde length of 2.5 cm) (Fig. 8). The calcareous concretionary horizons separate from their vicinity with their higher resistivity. It turns out from the microresistivity curve that the lime content decreases downwards unevenly, but this is not the case: it only seems to be so due to the averaging effect of the larger sonde spacing of other methods. The significance of this finding is that the water-conducting ability of non-paleosoil loess may also be anisotropic.

In sandy-clayey sequences deposited in water, positive anomalies of natural gamma are caused by the accumulation of clayey sediment rich in radioactive materials at the expense of the inactive coarser fraction. The connection with the grain size is the result of selective physical and chemical alteration processes taking place during transportation. In loess of eolic deposition there is no such selection, therefore in our opinion loess can be characterized by a uniform natural gamma level in which negative anomalies are caused by the leaching phenomenon associated with the formation of calcareous concretionary horizons, i.e. they have developed as a consequence of a destructive process. The natural radioactivity level of non-soilified clayey loess residues between the individual soils is very similar

to that of paleosoils, therefore natural gamma is a less effective distinguishing tool in relation to paleosoils than is magnetic susceptibility.

For every well it can be seen that the average resistivity of cycles decreases with depth, this phenomenon is caused by the increasing of water saturation of the space around the borehole. Based on the neutron porosity, density and natural gamma logs in well Űh-2 a three-component (clay content, porosity, coarse or sandy silt) lithological composition was calculated (fourth column in Fig. 9**). Within the individual cycles the highest values of clay content are associated with the resistivity lows, although the resistivity not only of sand but of layers classified as clay also decreases as a function of depth. From radiometric measurements we calculated the apparent fluid density (third column in Fig. 9), and from this the water saturation as well (S_w , third column in Fig. 9, $1-S_w$ curve). (Water saturation does not include the irreducible adsorption water content of clay [Clavier et al. 1977] and its apparent water content resulting from its OH^- content,

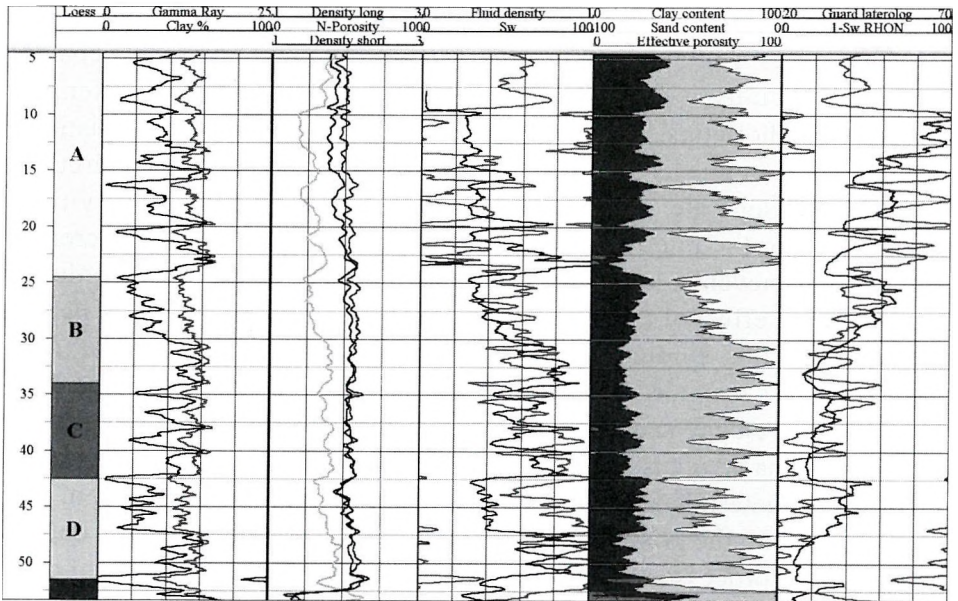


Fig. 9. Quantitative well log evaluation of Pleistocene loessic sequence

9. ábra. A pleisztocén lösz kvantitatív mélyfúrás-geofizikai kiértékelése

** From GR, N-Por, and Density measurement the effective porosity and apparent water saturation were calculated as follows:

$$1-S_wRHON=100-(FIN*0.55*SH)/(Fie/100)$$

$$Fie=(FIN /100)*(DEN+2.67-0.0102*sh)/0.0267$$

because these were taken into account as matrix features: depending on the type of clay mineral these two could account for up to 50% apparent porosity.) It can be seen in the figure that the apparent fluid density and the water saturation calculated from it — bearing in mind the average of the individual cycles — increase with depth. To the top of cycle B it can also be observed that within one cycle the water saturation of low resistivity (guard laterolog) clayey formations is higher than that of calcareous concretionary loess. From the above we can draw the conclusion that the clayey formations are also permeable, although to a lesser degree than other parts of loess. At depths of less than 25 m the clayey formations seem to be less water saturated: this suggests that their permeability is too low to allow considerable invasion during the drilling operations and time of measurement. It is very likely that the same holds true for the sequence below 25 m. From this the conclusion can be drawn that the clays at depths below 25 m were originally close to complete water saturation, while above this the clay layers also dried out.

Omitting the density we have calculated the water saturation (S_w)^{***} in well Űh-2 from resistivity, neutron porosity and natural gamma set, too, and this resulted in similar, but slightly different values than in the previous calculation (Fig. 9). The major difference between them is that the water saturation of the permeable layers with high ‘sand content’ is relatively low in cycles **B**, **C**, **D** and it increases with depth to a smaller degree. The main reason for the difference is that the penetration of the applied focused resistivity measurement (guard laterolog) is larger — it yields information on the borehole’s vicinity of larger diameter — than that of the nuclear measurements, the effect of invasion the diameter of which increases due to the increasing hydrostatic pressure with depth is stronger on the latter ones. In the case of cycle **A** the algorithm automatically brings the water saturation close to 100% because we took the *cementation factor*^{****} as be-

$$*** \left(S_w = \sqrt{\frac{FR_w}{R_f}}; \text{ where } F = \frac{a}{\Phi^m} \right)$$

S_w — water saturation (meaning the water saturation of the effective pore volume)

Φ — effective porosity (can be filled with not bound water)

R_w — resistivity of pore fluid

R_f — real rock resistivity, free of the effect of drilling fluid

a — constant, its value for loose sediments is between 0.6 and 0.8, otherwise its accurate value around 1.0 can be determined either by laboratory tests or by optimizing the parameters of the water saturation model

F — formation resistivity reducing factor (formation factor)

**** *Cementation factor*: this is based on the rock’s cementation and, as a consequence, on the windings of the current path (i.e. tortuosity): its value is about 2

ing constant along the whole borehole, therefore the calculation was carried out with a too small resistivity reducing factor.

The resistivity of cycle **A** is also higher in resistivity curves of engineering geophysical sounding than the electrical resistivity level of the other cycles, even the general decreasing trend with depth can be observed, which suggests that the increasing of water saturation with depth exists independently of the disturbing effect of drilling. According to laboratory studies the clay content increases with depth, which means at the same time deteriorating permeability, an increase in specific surface and together with this — because clay dries out with more difficulty than materials of high permeability — it means an increase in water saturation as well (even above 90%, to complete saturation). Well-logging measurements provide systematically lower values than electrical resistivity measurements of engineering geophysical sounding, but this difference decreases with depth, supposedly due to the general increase in water saturation with depth independently of saturation with drilling fluid. Within the Quaternary sequence, the upper, calcareous parts of all loess cycles can be marked out. Based on the resistivity log they are good water conducting zones.

3.2. Log results in granite body

Geophysical interpretation of siliceous crystalline (magmatic and metamorphic) rocks differs from that of sedimentary rocks in several respects.

The former rocks have practically no interconnected matrix or primary porosity, the whole pore volume depends on secondary mechanical or chemical alteration. Distribution of pore volume is linked with the strongly inhomogeneous fissure system. In the vicinity of cracks and especially of subsequently filled in cracks — due to the contact effects, including the non-hydrothermal, low temperature argillaceous alterations as well — one may not reckon with a uniform matrix from the viewpoint of physical parameters, in contrast to the sedimentary rocks in which the rock matrix is macroscopically speaking relatively uniform due to the deposition. (Fissures may develop at the boundary between two rock bodies of different physical parameters where the density and neutron porosity were originally inhomogeneous.) A consequence of this is that nuclear geophysical measurements (neutron porosity, gamma-gamma density measurement) primarily reflect changes in rock quality and only in second place do they

reflect changes in porosity. In other words, the traditional porosity sensitive methods used in sedimentary rocks — except for the cavernous sections — indicate changes in petrography (Fig. 3 second column).

Fissures cause significant changes primarily in the mechanical parameters of rock and in the internal specific surface of rock. Changes in porosity (whose absolute value is low) are of a smaller degree, therefore below a porosity of 3–5% porosity calculation basically means an estimation of the order of magnitude only. (An increase in neutron porosity indicates occasional chemical alteration in rock material.)

A common feature of fractured zones is — in contrast to fresh rock sections — the inhomogeneity of those physical parameters that are sensitive to break up of rock and to the extent of its internal surface. Acoustic and first of all electric measurements are sensitive to the fissure system and the fluid filling it in. Because of these factors we base the geotechnical characterization of granite on acoustic (acoustic waveform and acoustic borehole televiewer) and electrical (normal resistivity, focused resistivity) methods.

The parameters of the fractured zones are related to those of fresh granite. It is characteristic of fresh granite that it has only closed fissures in it, the velocity of its longitudinal waves is high, relatively constant, and the average resistivity is also high.

Because the rock itself is a non-conductor, fractures or argillaceous alteration tend to be the reasons for all decreases in resistivity; according to our knowledge the occurrence of semiconductor ore minerals is so rare in this area that it is negligible even from the viewpoint of fissure identification (argillaceous alteration also attacks the rock starting from fractures). Ion concentration of the bound water present in the rock fissures is high, thus its conductivity is orders of magnitude higher than that of the free fluid, therefore the electric resistivity is inversely proportional to the specific surface of rock. Fissures representing a porosity of only 0.1% in the measured rock volume reduce the apparent resistivity of rock to about 1000 Ωm , thus it causes at least one order of magnitude decrease in resistivity compared to fresh rock — while the rock's density and neutron porosity are practically unchanged — thus resistivity shows the presence of fractures in a strongly blown up form. (The real decrease in resistivity — taking into account the non-conducting nature of the rock — is five–six orders of magnitude, thus the measured decrease in resistivity depends really on the measuring range of the instrument.) It is noted that in a rock of about

1000 Ωm resistivity the propagation velocity of the acoustic wave is still around 5000 m/s, or rather above this value.

The propagation velocity of acoustic waves is proportional to the original state of the rock, therefore in the loosened, tectonized zones the degree of decrease in velocity may be especially high (Fig. 3). In the more strongly fissured and therefore loosened sections propagation — both velocity of the compressional wave (V_p) and velocity of the shear wave (V_s) — strongly decreases although the ratio V_p/V_s , significantly increases. (In high velocity rock just the opposite might happen at small fracture thickness, i.e. the ratio V_p/V_s decreases with decreasing V_p velocity.) It is mentioned that in the more strongly fractured zones the transversal wave cannot always be marked out in the acoustic waveform record due to the high attenuation. The non-cavernous, fissured sections are characterized by an increase in travel time and acoustic damping. Any kind of altered state of rocks can clearly be distinguished from the petrographical variety because alteration typically reduces the velocity below 5000 m/s, while the amplitude's attenuation — closely related to the increased energy absorption — increases.

3.3. Zoning the granite body (Fig. 10)

The main objective of geological exploration was to gain information on the hydrologic status in the area. Division of rocks into sections was an important means of doing this.

The weathered granite — at least its upper part — may form a uniform aquifer, therefore it must be excluded when planning the waste deposit site. However, its structure should be considered when calculating possible migration paths and the migration time from the repository to the surface. Acoustic and electric logs are the most effective means of examining the mechanical state and alteration of these zones. Acoustic wave propagation is sensitive to the presence of fissures. In our experience, when the fissures generate only a low porosity the acoustic waves propagating through the rock slow down slightly, but their amplitudes strongly decrease and the high frequency components disappear from the full waveform.

Zone **G I** can be characterized by a heavy amplitude attenuation in the full waveform acoustic log. The sonic velocity varies between 1500 and 3000 m/s, while its average is approximately 1700 m/s. It is obvious from the full waveform acoustic log that only the low frequency waves can

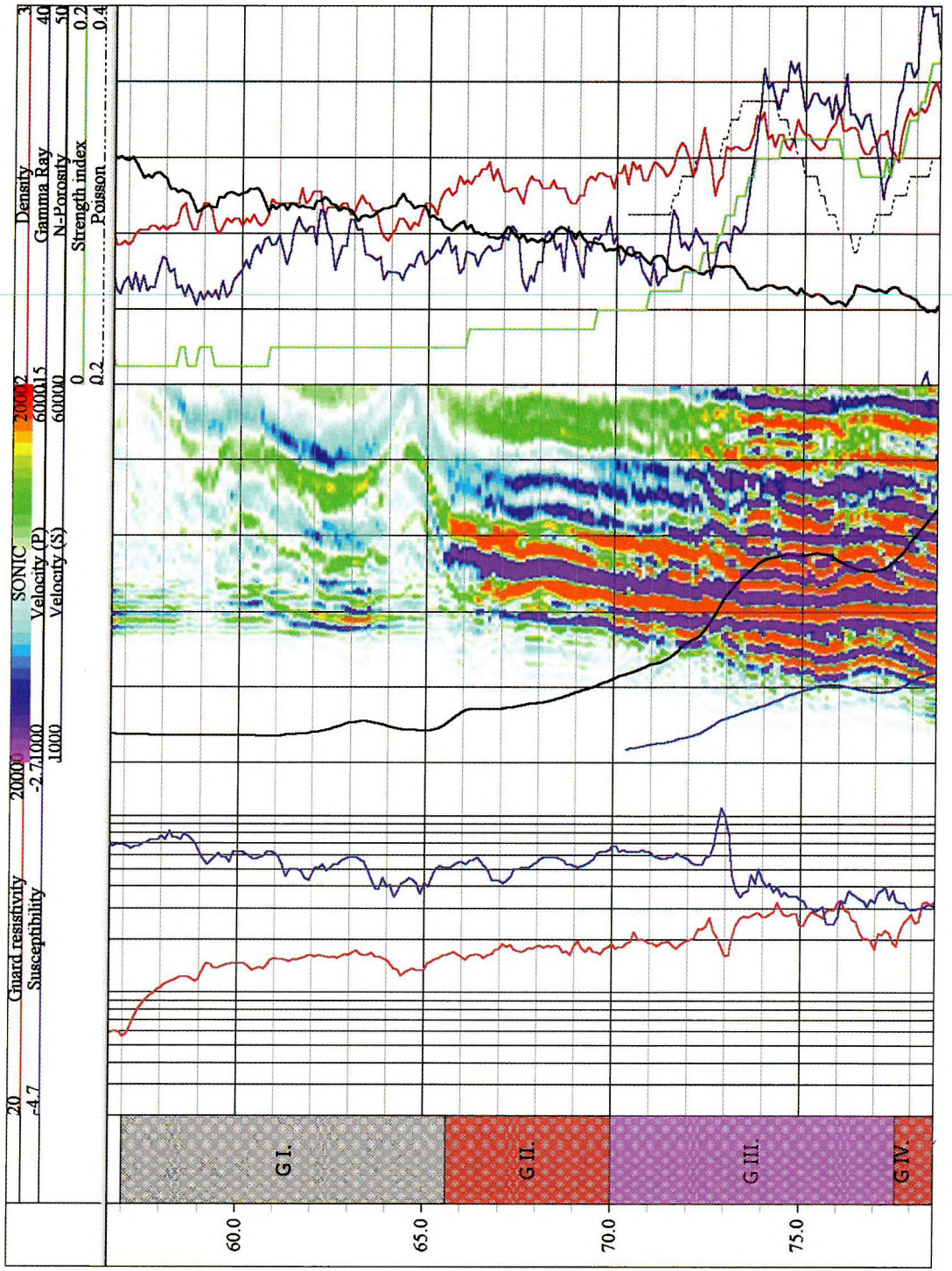


Fig. 10. Physical parameters of the upper part of the weathered granite
10. ábra. A gránit mállási kéreg felső részének fizikai paraméterei

propagate through the coarse granite sand and gravel, although at the bottom of the loess overlying it higher frequencies can also be observed in spite of the lower velocity. Therefore, it might be assumed that zone **G I** is less cemented than the loess and clay overburden but its porosity is lower. Within this subzone the longitudinal velocity definitely increases as a function of depth, this is a characteristic feature of loose, poorly consolidated rocks. No shear wave arrivals can be seen, even the Stoneley wave group can hardly be detected.

The measurements in subzone **G II** show that the proportion of coarse fragments and the cementation increase while the porosity decreases downwards. Stoneley wave velocity increases with depth at a lower rate showing a compaction similar to that observed in sedimentary rocks. The lowest part of this subzone practically does not show any compaction trend in Stoneley arrivals and no shear waves can be seen in the full waveform acoustic log. There is a rather good correlation between the compression wave velocity and the density, this indicates some similarity to sediments. The appearance of higher frequencies can be seen downwards in the weathered zone. The border between subzones **G II** and **G III** can be marked out at the depth where the first shear wave appears at about 70 m (Fig. 10).

Subzone **G III** consists of chemically altered, fractured but solid rocks and the top of it seems to be the starting level of the real hard formation from the viewpoint of acoustic logging. The shear wave arrival can be seen in the full waveform acoustic log, and high frequency components also appear. The V_p/V_s ratio decreases with depth within the subzone due to the rapid increase in V_s versus depth. V_p changes from 2500 to 4500 m/s. The Stoneley wave velocity is almost constant (the Stoneley wave arrivals can be seen after 1000 μ s with low frequency and high amplitudes). The resistivity is more variable due to the varying grade of chemical alteration and fracturing. Chemical alteration means dissolution of fracture filling material and that is why it has an influence on shear wave velocity.

Surface weathering effects have had only a relatively weak impact on the rocks of zone **G IV** (granite showing weak surface effects). A slow increase in shear wave velocity and electrical resistivity with depth is characteristic of this part of the weathered zone. Weak depth trend in porosity- and fracturing sensitive parameters and the direct contact with the overlying weathered sections suggest that surface effects still hit it; based on this, it is ranked among the weathered zones. In some boreholes (e.g. in $\ddot{U}h-2$), supposedly as a consequence of the argillization which decreases with

depth, the neutron porosity decreases downwards. In conformity with the mechanical condition of zone **G IV** it is very similar to zone **G V** of solid rocks. The longitudinal wave velocity is somewhat lower than in the solid parts of the depth interval **G V**. The rocks in zone **G IV** are hard enough for BHTV investigation. In the BHTV record more open fissures can be seen in zone **G IV** than in sub-zone **G V** (*Fig. 11*).

In granite which is free of surface effects — zone **G V** — physical parameters do not depend on depth: these parameters are primarily linked with fissures and alteration in rocks, secondly with rock composition (*Fig. 3*). Acoustic and first of all electric measurements are sensitive to the fissure system and the fluid filling it in. Because of the above factors we base geotechnical characterization of granite on acoustic (acoustic waveform and acoustic borehole televiewer) and electrical (normal resistivity, focused resistivity) methods.

From the hydrologic viewpoint fissured zones can be characterized by the volume of infiltrating water. In what follows we first discuss the peculiarities of geophysical well-logging interpretation of fissured granitoid rocks; we then deal with the sectioning of fresh granite from the geotechnical viewpoint; next the fissured zones are characterized based on the distribution of their physical parameters; the methods for determining fissured zones dip are briefly discussed; a hydrologic characterization of fissured zones is given; and infiltrations are introduced; finally our results are summarized.

The more heavily fissured fracture zones have been characterized by physical parameters proportional to the number of fissures (i.e. fissure density), and by their position (dip, dip direction).

It is pointed out that determination of the position of fissured zones is rather uncertain because the geophysical well-logging information refers to a small volume. The position of fissured zones was determined in three ways:

- from reflections identifiable in the full acoustic waveform;
- from the direction statistics of the BHTV;
- from the position of the edges of fissured zones detected by the BHTV.

Velocity and resistivity begin to decrease at a distance from the fractured zone because of the secondary fractures and the tiny cracks. It can clearly be seen in the BHTV records that the open fractures are more fre-

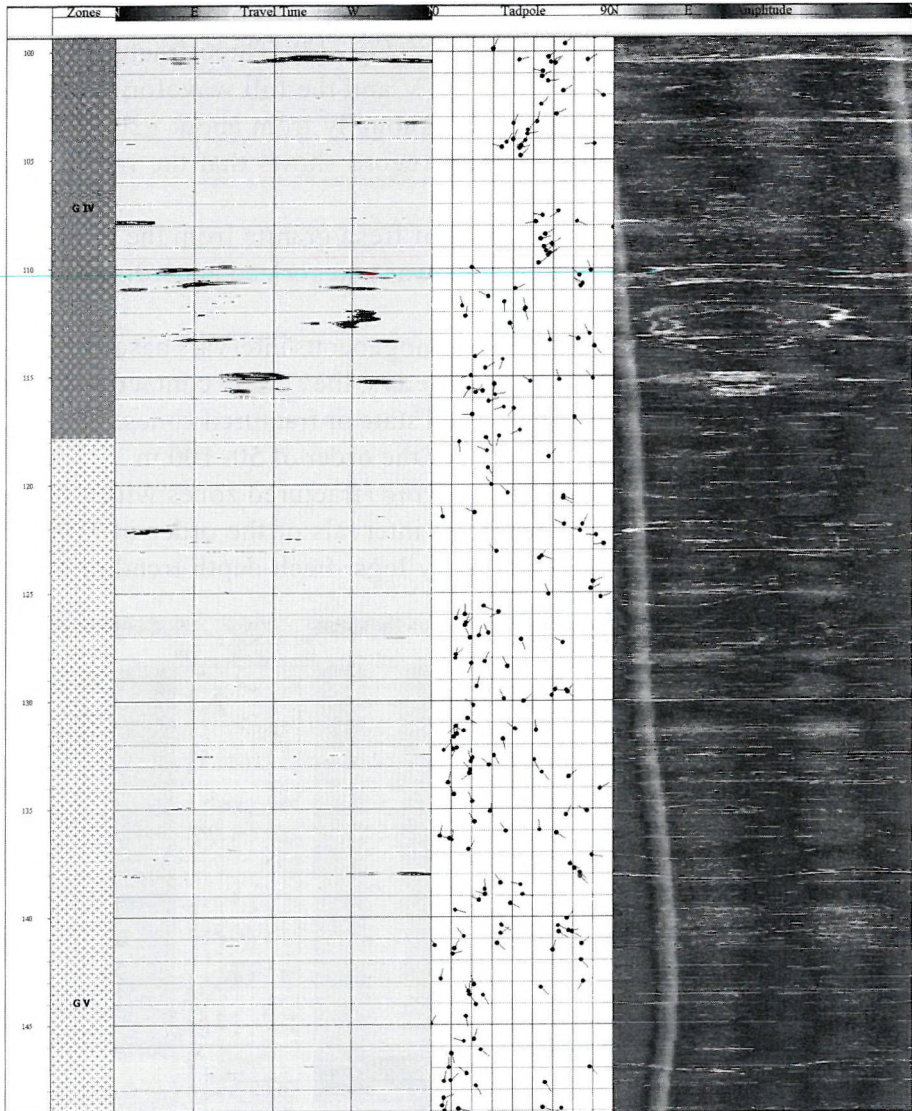


Fig. 11. Boundary between zones **G IV** and **G V** on BHTV images
 11. ábra. A **G IV** and **G V** zóna közti határ a BHTV képeken

quent on approaching the fractured zone (214 m). The most frequent tectonic directions can be seen on a rose diagram.

It is very interesting that the large open fracture at 214 m does not produce any inflow and the less fractured zone at 196 m gives a few tenths of a

liter per minute (Fig. 6. fifth column). The lower part of the borehole penetrated a more strongly weathered zone (Fig. 12). Three fractured zones can be distinguished based on the BHTV and the full waveform acoustic log. Velocity and resistivity decrease gradually from about 320 m downwards. The light colour of the BHTV record shows that the rock at this depth is looser than that over it.

To interpret the extent of fracture of fresh granite from the viewpoint of its geotechnical state, the **G V** zone was categorized according to three kinds of units of different scale:

- *Large blocks* mean relatively homogeneous intervals based on average values of geophysical parameters, they are in contact with each other along zones of deteriorated state or fractured zones. The large blocks are located at intervals of the order of 50–100 m.
- *Zones with depth trends in fissuring* (fractured zones with their associated fissures) are located at intervals of the order of 10–30 m identifiable in electric resistivity logs. Each depth trend ends in a

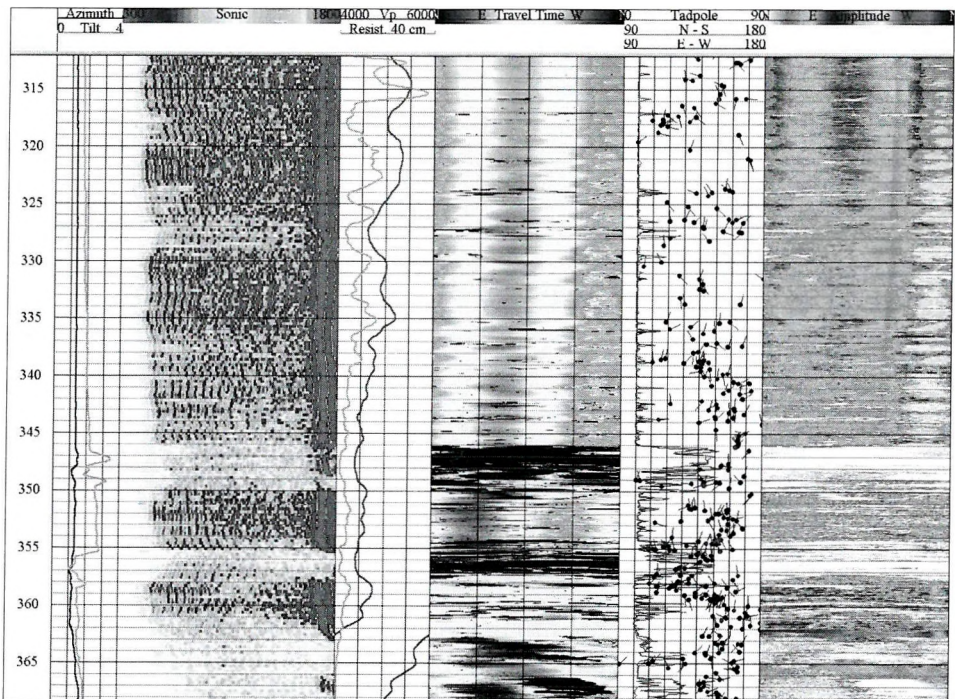


Fig. 12. Highly fractured depth interval and its vicinity in a well
12. ábra. Egy erősen töredezett mélység szakasz és környezete

more heavily fissured or smaller fractured zone, these represent the low resistivity end of the depth trend. A large block can be divided into several intervals with independent depth trends in fracturing.

—*Fractured zones* are at intervals of the order of magnitude of 1–10 m that can be marked out within the resistivity depth trends based on the acoustic waveform and the BHTV. These fracture zones may be simple, at the same time sharply separated from their surroundings or have complex, poorly defined edges (*Fig. 13*).

It is mentioned that strongly cavernous, tamped sections of boreholes are ranked among the fractured zones based on technical and geological information; it is, however, impossible to obtain quantitative information within them.

4. Characterization of fractured zones

Fractured zones can be characterized both by the statistics (average, standard deviation, most frequent value) and spatial distribution (shape of log) of the physical parameters. Inhomogeneity of the physical parameters in the fissured, fractured zones is reflected by their larger scattering, the latter in itself suggesting a more altered state of rock.

In *Fig. 14*, it can be seen that in the low resistivity, supposedly fractured zones the differential resistivity (d Resistivity) values and differential V_p (dV_p) logs (logs of changes over a unit interval of depth) show higher values.

Inhomogeneity of rock in a given interval can be characterized by the most frequent value, scattering and shape of the physical parameters' empirical distribution (histogram). In fissured rocks, thus especially in fractured zones, the distribution of parameters depending on fracturing is mostly asymmetric, log normal or inverse log normal. For example, the conductivity (calculated from guard resistivity) in well Üh–2 between 210 and 225 m (*Fig. 15*) shows log normal distribution, which suggests that the statistical weight of the fissures is relatively small. The fractured zone in well Üh–23 between 168 and 173 m (*Fig. 16*) is similar to this, but the greater statistical weight and the bimodal shape of the distribution of high conductivity values indicate the strongly fissured, fractured character of this zone.

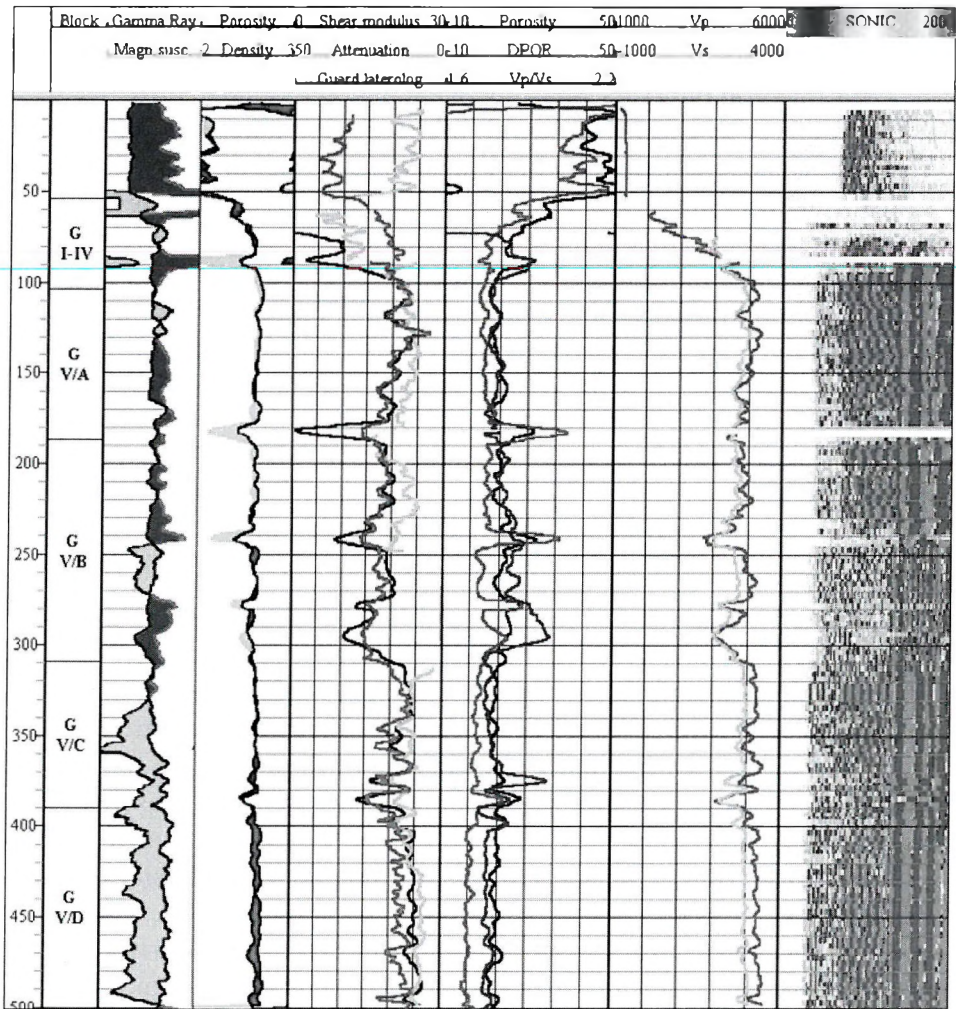


Fig. 13. Petrophysical quick look interpretation in comparison with geotechnical interpretation

13. ábra. Petrofizikai gyors kiértékelés összehasonlítása a geotechnikai interpretációval

Spatial inhomogeneity also characterizes the fissured zones. Fissuring gets weaker further from the plane of fracture or fault. This weakening, however, does not take place as a monotonic decrease, but it appears as an average trend in the electric resistivity and acoustic velocity logs. In general, several subsequent depth trends of identical direction can be observed, this very likely suggests rock stresses of the same character.

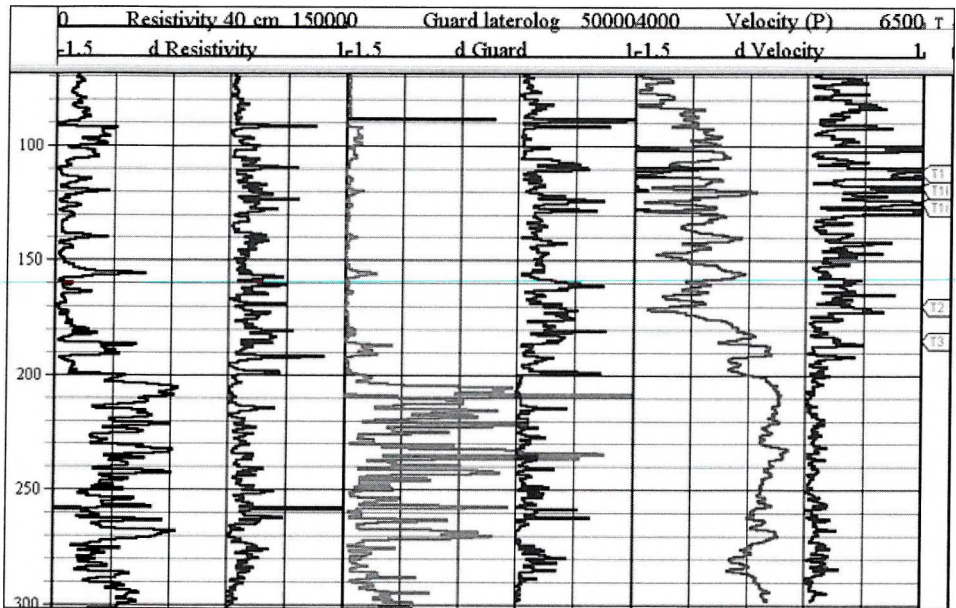


Fig. 14. Differential logs of resistivity and of acoustic-wave velocity
 14. ábra. Ellenállás és akusztikus hullámsebesség derivált szelvények

In Fig. 17 the most characteristic acoustic properties of fissure zones can be observed:

- gradually increasing velocity moving away from the fracture (downwards from the fractures at 99.8 and at 123 m in the figure),
- decrease in characteristic frequency with the decrease of the acoustic wave's propagation velocity,
- increase in acoustic attenuation with decrease in velocity (marked with fainter colours in the figure),
- increase in ratio V_p/V_s with increasing fracturing, frequency dependence of the ratio V_p/V_s and absorption.

In what follows we attempt to throw light on the connection between the parameters by studying cross plots, deducing from this the integrity of the rock matrix; then the separation of open and closed fissures based on BHTV measurements is discussed.

The connection between the individual parameters is — just like in the case of the parameters of the weathered crust [ZILAHÍ-SEBESS et al. 2000] — characteristic of the individual fractured zones.

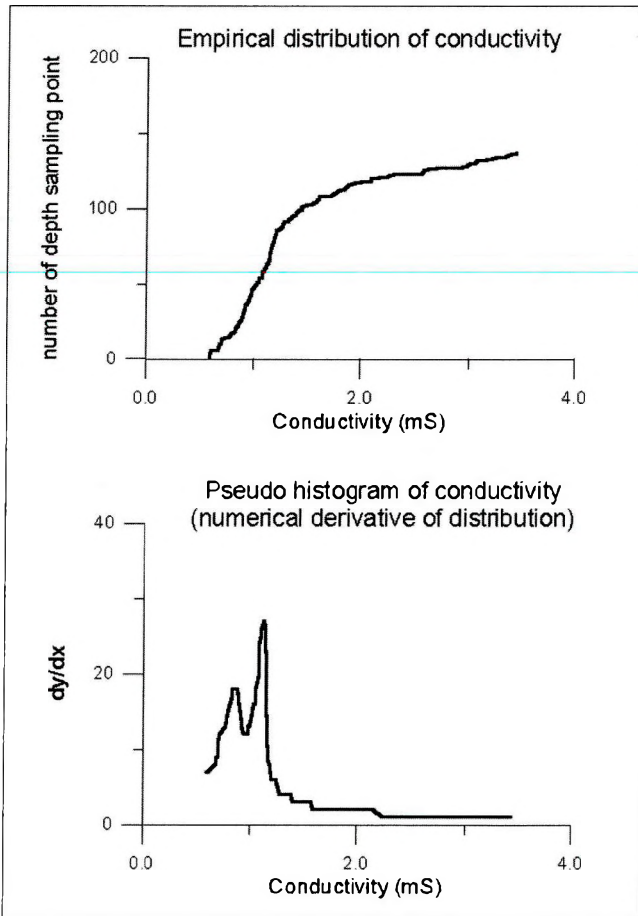


Fig. 15. Empirical distribution and pseudo histogram of conductivity (calculated from guard resistivity) between 210 and 225 m in a fissured depth interval (210–225 m) in borehole Űh-2

15. ábra. Empirikus vezetőképesség (guard ellenállásból számítva) eloszlás és pszeudo-hisztogram egy repedezett mélység szakaszon (210–225 m) az Űh-2 fúrásban

In studying the connections between the geomechanical parameters for the whole rock the aim is to characterize the fissured zones. This connection is basically controlled by the structure of fissure system. In this respect, we consider the fissure zone as an element of a larger structure. If, therefore, we investigate the connection between the parameters themselves at different scales it means investigating the relationship between the whole fissure system and the larger fracture zones. In other words the relationships represented by the cross plot valid for the individual fissured

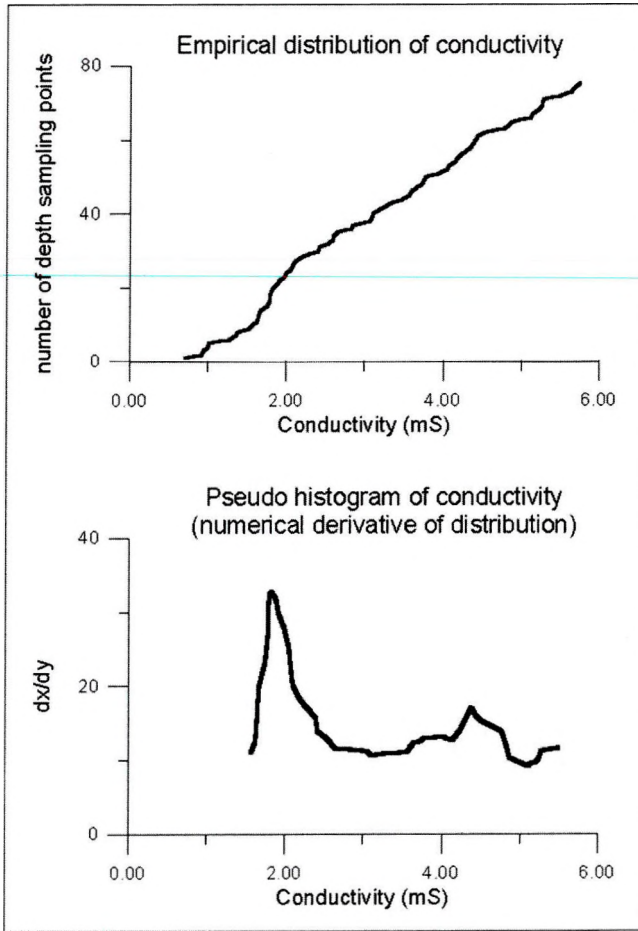


Fig. 16. Empirical distribution and pseudo histogram of conductivity (calculated from guard resistivity) in a strongly fissured depth interval (168–173 m) in borehole Üh–23

16. ábra. Empirikus vezetőképesség (guard ellenállásból számítva) eloszlás és pszeudo-hisztogram egy erősen repedezett mélység szakaszon (168–173 m) az Üh–23 fúrásban

zones separately can significantly differ from the connection determined from all depth points for the whole rock. Among the main reasons for this is that the pressure increasing with depth is critical — which even in the case of surfaces in contact and considered constant is able to increase the shear resistance alone without any kind of cementation, but not the electrical resistivity, if the specific surface otherwise does not change.

In our experience the logarithm of electric resistivity is directly proportional to shear modulus (Fig. 18). If one studies the sections separately

it turns out that the connections differ from each other according to depth sections; this explains the relatively high scattering of the connection taken for the whole borehole. The most probable explanation for this is the following: The shear modulus is directly proportional to the integrity of the rock matrix, or to fissure density and fissure aperture; electric conductivity is proportional at least to the second power of pore volume according to Archie's formula ($R_t = R_w / \Phi$). Electric conductivity is proportional to the specific internal surface because the conductivity of the bound ion-rich water [CLAVIER et al. 1977] is by one–two orders of magnitude higher than that of free fluid. It follows from this that the more complicated the internal surface, the higher the conductivity. In borehole Üh–22 (Fig. 18) considering all the depth points the increase in resistivity as a function of shear modulus is stronger than exponential, this derives from the fact that the smaller the aperture size of a fissure the higher the probability that from a certain portion of the planes in contact the electrolyte is squeezed out, and the tortuosity of the pore volume represented by the fissure also increases. Where the conductive fluid is squeezed out, i.e. in a capillary crack system of micron size, the resistance to shear force approximates the parameters of the fissure-free rock depending on pressure. MESKÓ [1995] discusses in detail the connection between the propagation velocity of elastic waves and microcracks; this connection is closely linked with the shear modulus.

In well Üh–3 (Fig. 19) at high shear moduli — in the interval of 200–300 m (brown) — large changes in resistivity coincide with small changes in shear modulus, which can be explained by a large change in tortuosity. This situation exists at fissures of very small aperture, where most of the opposite surfaces of a fissure fit into each other. This ensures high shear strength, but the volume that can be filled in with electrolyte and the associated tortuosity can change by orders of magnitude, whereas the effective surface in contact changes only very slightly. In the depth interval of 105–200 m (red), when the shear modulus changes to a great extent, the logarithm of electric resistivity changes in a smaller degree than in the lower section, suggesting that the fissures are generally thicker and they may contain free fluid, too. In the fissure system the relative amount of conducting surfaces is higher in comparison with the nonconducting joints than that of deeper zones.

Acoustic attenuation is roughly inversely proportional to electric resistivity (Fig. 20). Acoustic attenuation is calculated from the longitudinal wave trains, thus it is less sensitive to microfissuring than the conductivity

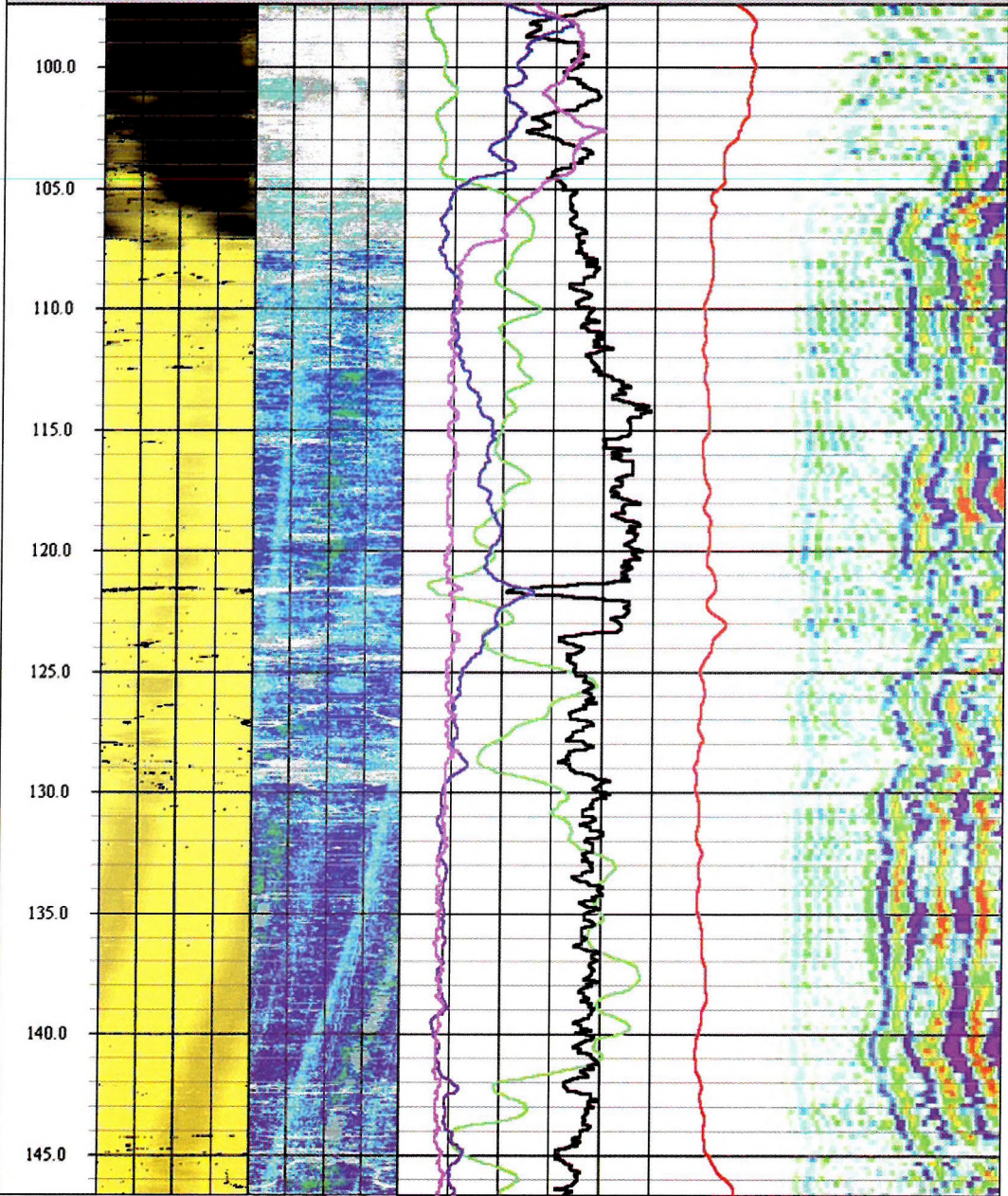
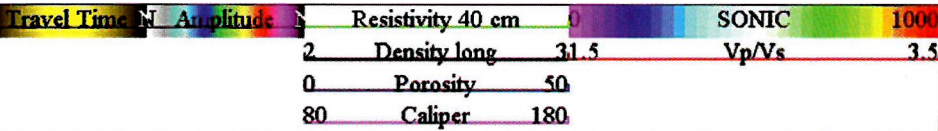


Fig. 17. Acoustic borehole televiwer and full acoustic waveform records in the vicinity of a fault

17. ábra. Akusztikus lyukfal televízió és teljes akusztikus hullámkép felvételek egy töréses vető környezetében

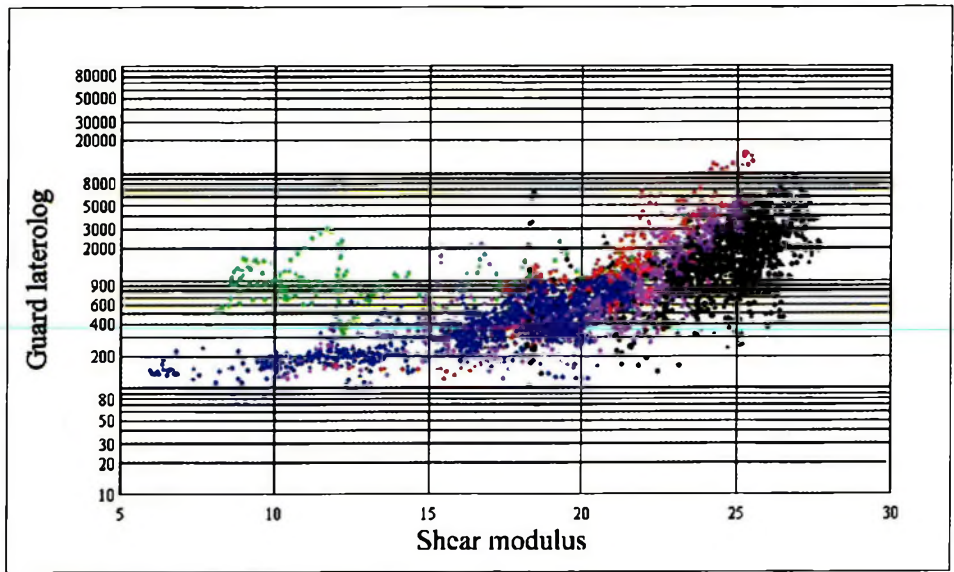


Fig. 18. Relationship between the shear modulus and electric resistivity in borehole Üh-22

Legend: The depth intervals are marked with different colours, viz. Green: 53–103.4 m,

Red: 103.4–187 m, Blue: 187–309 m, Lilac: 309–390 m, Black 390–500 m

18. ábra. A nyírási modulus és az elektromos ellenállás közti kapcsolat az Üh-22 fúrásban

Jelmagyarázat: A színek különböző mélységintervallumokat jelölnek; zöld: 53–103,4 m,

vörös: 103,4–187 m, kék: 187–309 m, lila: 309–390 m, fekete: 390–500 m

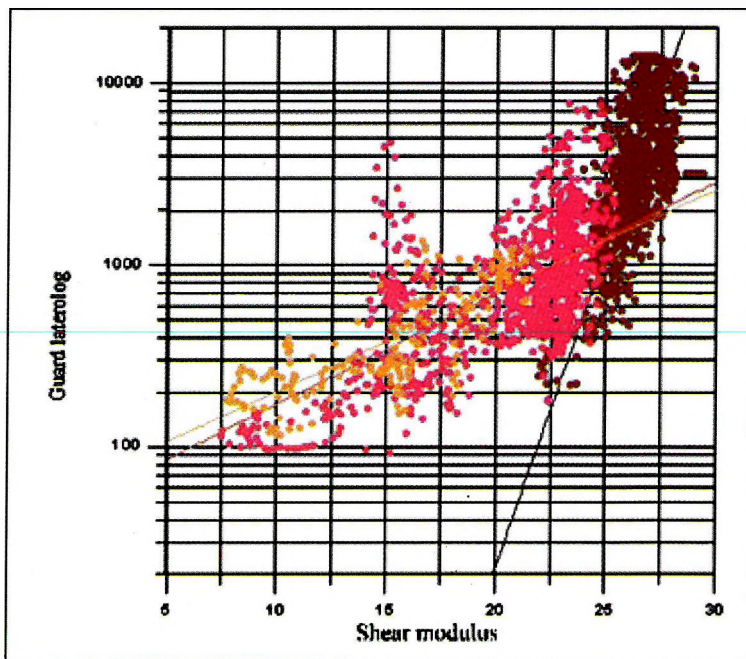


Fig. 19. Relationship between shear modulus and electric resistivity in borehole Űh-3
Legend: The depth intervals are marked with different colours, viz. Orange: 85–100 m.
 Red: 105–200 m, Brown: 200–300 m

19. ábra. A nyírási modulus és az elektromos ellenállás közti kapcsolat az Űh-3 fúrásban
Jelmagyarázat: A színek különböző mélységintervallumokat jelölnek; narancs: 85–100 m,
 vörös: 105–200 m, barna: 200–300 m

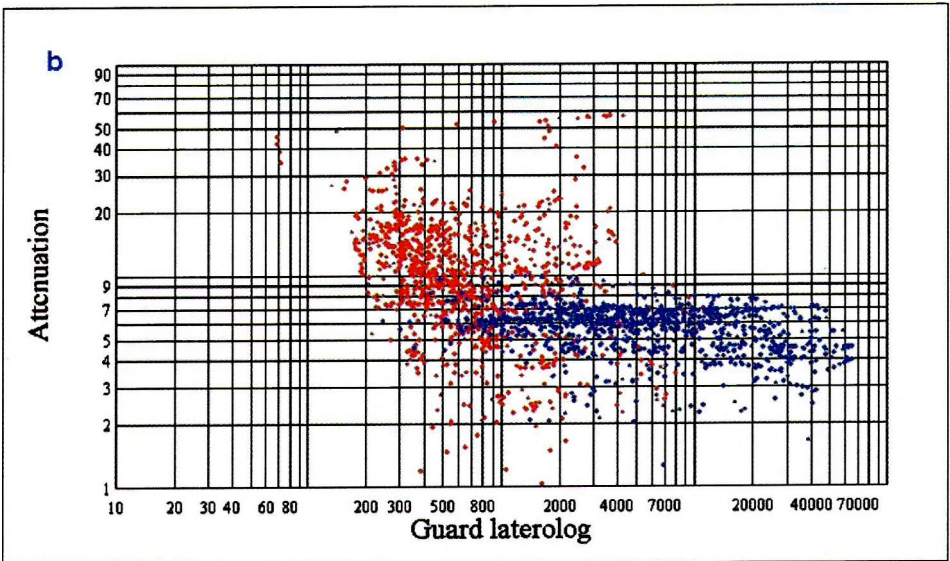
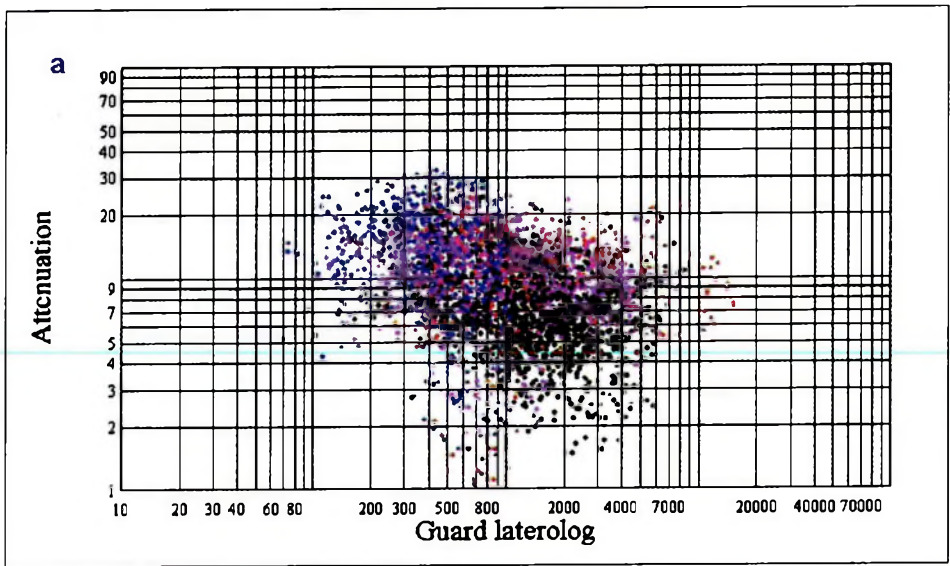


Fig. 20. Relationship between electric resistivity (guard laterolog) and acoustic attenuation in boreholes Üh-22(a) and Üh-23(b)

Legend: The depth intervals are marked with different colours, viz.

Üh-22: Red: 103.4–187 m, Blue: 187–309 m, Lilac: 309–390 m, Black 390–500 m
 Üh-23: Red: 91–199 m, Blue: 199–300 m

20. ábra. Az elektromos ellenállás (guard laterolog) és az akusztikus csillapítás közti kapcsolat az Üh-22(a) és az Üh-23(b) fúrásokban

Jelmagyarázat: A színek különböző mélységintervallumokat jelölnek:

Üh-22: vörös: 103,4–187 m, kék: 187–309 m, lila: 309–390 m, fekete 390–500 m
 Üh-23: vörös: 91–199 m, kék: 199–300 m

which is basically considered proportional to the specific surface of micro-fissuring; thus, the higher the resistivity the higher the scattering of attenuation. In the case of well Üh–22 (Fig. 20a) besides the existence of inverse proportionality the scattering is much greater than in well Üh–23 (Fig. 20b). This is primarily due to the higher sensitivity of the guard laterolog to microfracturing.

4.1. Methods to determine the dip of fractured zones which are probably faults

Generally tectonic faults are represented on the borehole wall by fractured zones. Not every fracture zone represents main tectonic planes, frequently they are only second or third order fissure systems attached to the primary fault. On a large scale we have only limited information on a tectonic plane and moreover they are not planes but nearly plano-parallel plates in the strict geometrical meaning. These fractured zones may contain many elementary fissure planes. Their orientation represents the true tectonic dips and azimuths only in the statistical meaning. In some disadvantageous cases, e.g. large cavities, only the edge of a highly fractured zone or some accompanying fissures represent the true orientation.

In view of the above the reliability of determination increases if the dip of a fracture zone can be determined by various, independent methods. Tectonic dipping was determined at the Üveghuta site utilizing two kinds of measurement, viz. acoustic waveform and acoustic borehole televiewer image, in three basically independent ways. In contrast with the dip values we can determine the dip direction based only on the BHTV measurement according to two principles — statistics and individual fissure direction interpretation.

In what follows we discuss reflections obtained from the acoustic waveform; the direction statistics from the BHTV; finally, the edges of the fractured zones detected by the BHTV.

4.2. Dip determination by reflections from the acoustic waveform without azimuth

In the acoustic waveform, in addition to the compressional (P), shear (S) and tube waves, reflections obtained from the larger fracture surfaces — usually at the end of a fractured zone identifiable in the acoustic waveform and in the electric resistivity log, which shows maximum frac-

turing — can also be observed (*Fig. 21*). The reflection time increases with the distance from the intersection of the reflecting plane and the borehole, thus a straight line section appears in the acoustic waveform enclosing a certain angle with the depth axis; this represents a section of the travel time–distance curve and starts from the first arrival. These straight line sections are produced by the interference between the wave reflected from the fracture plane and other waves. Mostly two straight line sections are considered because we obtain reflections above and below the reflecting plane as well, therefore we can see a V-form in the acoustic waveform.

Knowing the propagation velocity of an acoustic wave characteristic of given rock the dip of the fracture zone can be computed from the position of the straight line section. The most frequent dips are around $45\text{--}50^\circ$ and $70\text{--}80^\circ$ (e.g. the reflections that can be seen in *Fig. 21* represent dips of 44 and 66°). This is consistent with the average dip values detectable by BHTV measurement. Dips of around 20° can also be detected; for smaller dips than these, however, the inaccuracy is too large, i.e. we cannot characterize them quantitatively. The reliability of dips identifiable from acoustic waveforms is better than that of data obtained by other measuring devices or core analysis because the information is obtained from the immediate vicinity of the borehole, its disadvantage is that being a circular symmetric measurement no dip direction belongs to it.



Fig. 21. Reflection in the acoustic waveform in borehole Űh–23
 21. ábra. Reflexió az akusztikus hullámképen az Űh–23 fűrásban

4.3. Directional statistics of acoustic borehole televiewer

Fissure direction statistics have been constructed based on BHTV measurements and we have made an attempt to determine the position of the major fracture zones which supposedly exist further away from the borehole, too. Directional distribution of dip azimuths have been plotted in a circular diagram (also known as a rose diagram). For plotting purposes the circle is divided into segments of a certain angle. The radius of the coloured segment is proportional to the number of azimuths falling in the direction of the segment normalized to the total number of azimuths within the given depth interval. In our rose diagrams we generally used a division of 10° , at small amount of data of 20° . In this representation dip values are not taken into account. (In contrast to the diagrams used in geology, it is not the strike that is plotted in the obtained rose diagrams but the dip of fissures, therefore the diagrams are not symmetrical.) If a definitely distinguishable frequency maximum falls into one or into two neighbouring segments, it is called a *characteristic direction*. If the frequency maximum occupies several segments, i.e. it is smeared over a certain angle interval, then we use the term *more characteristic direction* sector. The fissure system of a larger block can also be characterized by the direction statistics, information on the existence or possibility of a connection between them can be obtained by comparing them with the position of fractured zones. The classification of fissures was given in section 2.1. of this study.

In well Üh-22 (Fig. 22) the most frequent characteristic direction of closed fissures in the granite body is north, the westerly direction is separated as a definite frequency maximum, but with a relatively small weight. According to the directional statistics of open fissures, fissures with a northerly direction are also frequent in borehole Üh-22. Real dominant directions (NNW and SW) exist for the thin fissures providing incomplete sinusoids only in the upper part of the solid granite. In the lower zone the directions are more scattered and the two most frequent directions are W and NNE. The characteristic direction of the thick fissures providing an incomplete sinusoidal curve is unambiguously N in the uppermost section, while in the lower one a strong easterly direction appears as well.

According to the rose diagrams constructed based on the above considerations and shown in Fig. 23 the majority of all fissures in the 168–185 m interval of well Üh-23 fall into the NW segment. The most frequent direction of open fissures is NW (this coincides with the direction de-

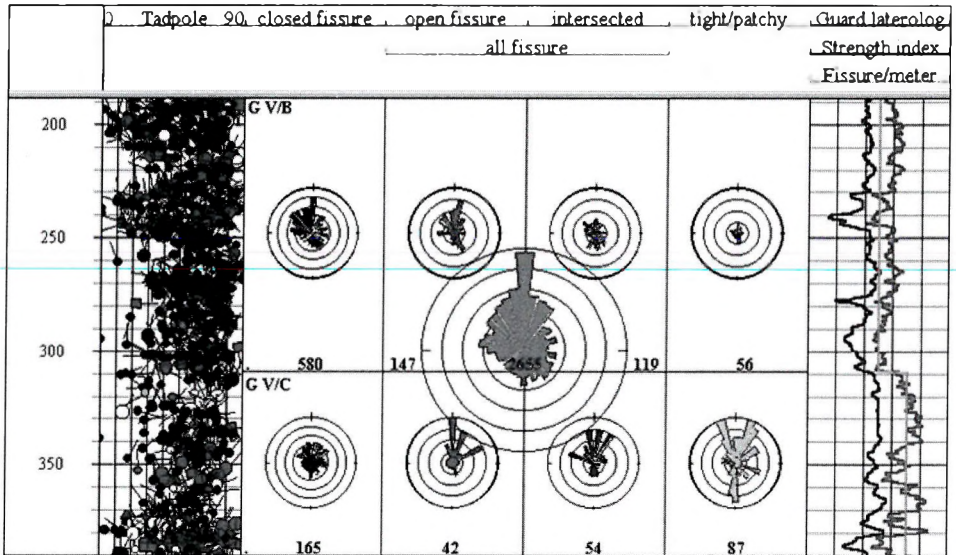


Fig. 22 Dip direction statistics of two blocks (two depth intervals) in borehole Üh-22
 22. ábra Két blokk (két mélység szakasz) dőlésirány statisztikája az Üh-22 fúrásban

terminated from the individual fissure edges for zone T3), the second most frequent direction is SE.

4.4. Edge of the fractured zones detected by acoustic borehole televiewer

Those depth intervals where a large number of wide, open fissures can be seen in the borehole televiewer record that frequently converge are called a *fractured section*. In contrast with the other sections these cannot be correctly characterized based on the fissure density because the fissure planes frequently do not provide a complete sinusoidal curve in the record.

From among the fractured zones in the reflection time image of the borehole televiewer those sections are called *probable faults* which contain many open fissures, for which the real dip can be determined relatively unambiguously. In *Table I* the probable faults of borehole Üh-22 are listed. The dips representing probable fracture, being within the most heavily fissured sections, were not marked on a statistical basis because determination of the fissure plains is uncertain, thus the statistics constructed from them do not satisfactorily characterize the depth interval.

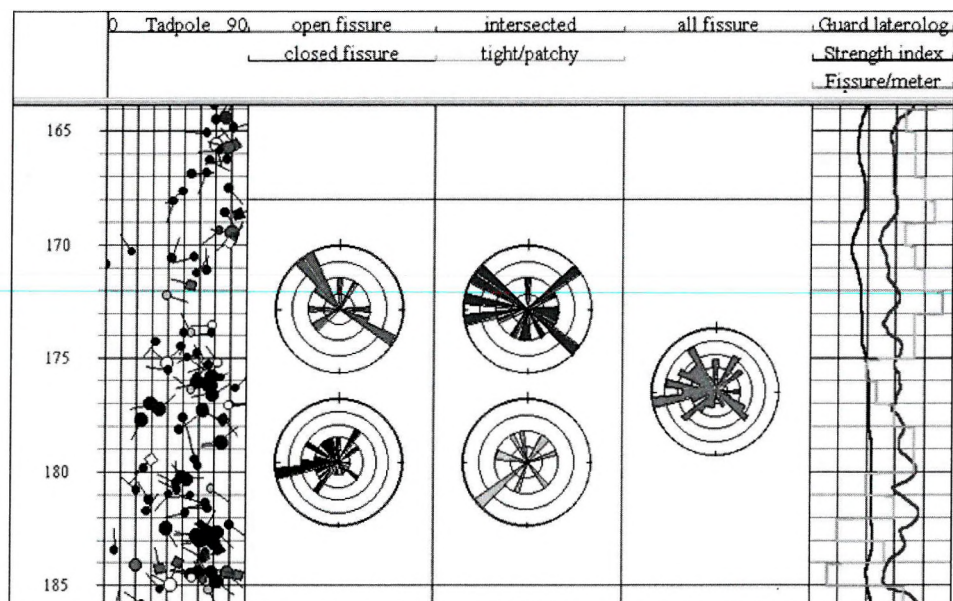


Fig. 23. Dip direction statistics of a block (one depth interval) in borehole Üh-23
 23. ábra. Egy blokk (egy mélységszakasz) dőlésirány statisztikája az Üh-23 fúrásban

The most reliable position data can be determined at the edge of the selected zone, at the boundary between the fresh rock and the crushed zone. When this was not possible, a sinusoid seeming to be a definite direction — possibly repeated several times above 214 m — was chosen close to the boundary of the crushed zone (*Fig. 24*).

The main aspects of selection were the following:

I. How sharply the edge of the crushed zone is delimited from its vicinity. In contrast with zones marked *T* in Table I. — in the marking off of which acoustic waveform and electric resistivity play a role, too — in this case the edge of the crushed zone means strictly the edge of the zone consisting of open fissures which can be seen in the BHTV image.

II. How perfectly can a sinusoid be fitted to the selected fissure, i.e. how much it represents a plane?

III. Is the direction obtained repeated in the close vicinity (within 1–2 m)?

IV. Does the direction obtained coincide with the direction of other fractured zones? (This criterion is based on the assumption that if a direc-

Üh-22					
depth of well [m]		dip [°]	dip direction [°]	main criterion of selection	
T1 below the top	90.8		42	246	A ³ E
T3 fk top	156.7		71	154	A ³ E
T3 k top	170.6		64	335	B ⁴ E
T3 below the top	178.4	(178.4–178.8)	59	350	A ⁴
T3 bottom of a larger zone (lack of data above it)	186.8		52	18	D ²
T4	239.7	(239.7–241.7)	74	1	D ³
T4 middle	241.5		73	0	D ¹
T5 top	276.5	(276.5–278.0)	62	145	A ³
T6 middle	295.8	(293.8–295.7)	59	6	C ⁴
T7 top	381.0		63	5	B ¹ E

Table 1. Dips and azimuths representing a possible fault

Legend: Marks T1, T3, etc. serve to identify the fractured zone. The numbers in the upper index show the quality of sinusoid curve fitting, i.e. reliability of the individual interpretability, increasing from 1 to 5. (For the selection criteria, see text.) For categories C and D the edges of the fractured zones observable on the acoustic borehole televiewer image are highlighted

1. táblázat. Egy lehetséges vető jellemző dőlés és azimut értékei

Jelmagyarázat: T1, T3, stb. a repedezett zónát jelentik. A felső indexben szereplő számok a szinusz görbe illeszkedésére jellemzőek, azaz az egyedi értelmezhetőség megbízhatóságára.

1-től 5-ig terjedő skálán. (A kiválasztási feltételeket lásd a szövegben). A C és D kategóriáknál az akusztikus lyukfaltelevízió képen megfigyelhető repedezett zóna széleit emeltük ki

tion is really characteristic of an area, then it can also appear in the direction of more fissured zones.)

The tectonic directions selected on the basis of these criteria and representing the selected possible fault are ranked into the following categories:

A) Fissure edge: sharp, and a sinusoid can closely be fitted to it on the laid out cylinder-jacket.

B) Fissure edge: a less sharp, sinusoid can less closely be fitted to it, but its direction is repeated several times.

C) Edge of the fractured zone: less sharp, but a sinusoid can closely be fitted to it, and the obtained direction is repeated at several fissures.

D) Edge of the fractured zone: less sharp, a sinusoid cannot be well fitted to it, the obtained direction is similar to the direction of other zones.

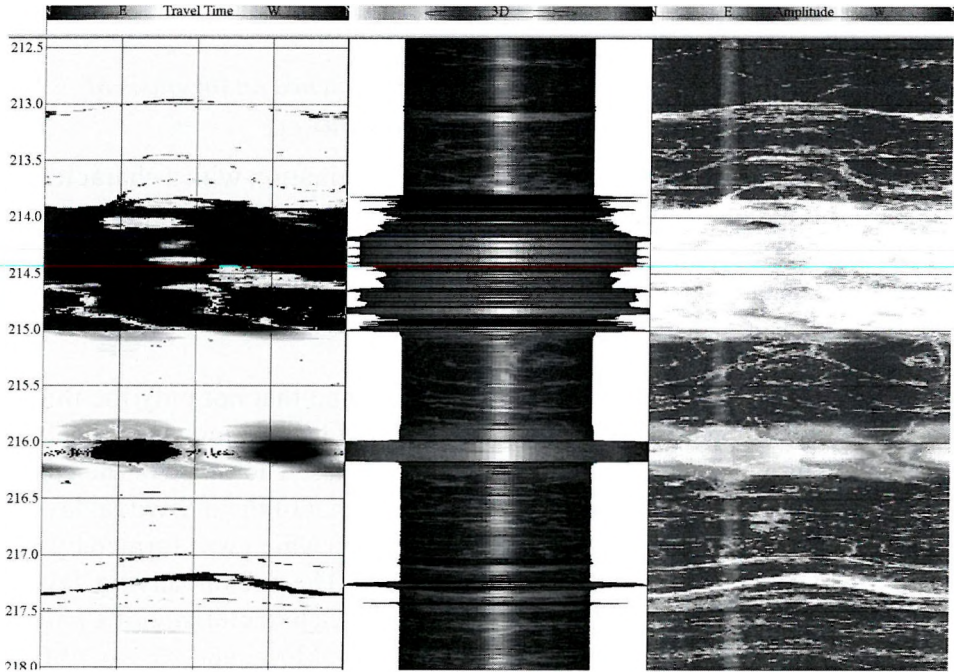


Fig. 24. A possible fault and its vicinity in BHTV images

24. ábra. Egy valószínű vető és környezete az akusztikus lyukfal televízió képen

E) In the close vicinity of selected fissure (0.1–0.2 m) there is no continuous fractured zone and this is taken into account as an independent condition.

The fissure edge or edge of the fractured zone may be an easily identifiable sharp line, but the sinusoid can be fitted to it — although imperfectly — if the fissure plane is curved. It is marked separately where the place of determination is within the fractured zone. In Table I. the numbered zones marked with *T* are the fractured zones which are not interconnected. Each fractured belt is part of a zone with a definite depth trend in fracturing determined on the basis of a resistivity and an acoustic measurement.

5. Correlation between wells

5.1. Correlation within the Quaternary sequence on the basis of well-logging measurements

Well-logs reflect the evolution history of formation with a characteristic pattern which characterizes the given sedimentary formation.

In general, the curve pattern takes shape at the vicinity of the formation boundary and it can be considered a characteristic identification mark; thus by means of well-logs the question as to whether it is over- or underlying stratigraphically can be answered as well.

When correlating paleosoils it is fundamental that not only the thickness and spatial position of soils are considered but the log shape itself is also taken into account at the individual anomalies. The shape of the curve is characteristic not only of the whole sequence but of the individual layers as well. It can be considered an individual pattern which was formed by the natural process that brought it into existence. The accompanying layers and the structure within the individual layers are characteristic of a paleo-soil stratum: they formed this individual pattern. Moreover, we can obtain more information by measuring the magnetic susceptibility with a sonde length of 20 cm and a sampling interval of 10 cm. Taking into account the disturbing effect of landslide, erosion correlation is more reliable if paleosoils are not considered separately, but as parts of a certain period because the possibly omitted soil horizons or those appearing to be surplus can more easily be classified.

Summarizing, we accept the pattern provided by the resistivity and magnetic susceptibility curve groups as a basis for identification because due to its richness in detail it is such an individual feature of a sequence which may be suitable for identifying a simultaneous sequence of events taking into account the nature of eolic sedimentation.

Correlation between wells is aimed at matching the already mentioned sequences marked A, B, C, D, E and within them the paleosoils. In Table I. the elevation of correlatable sequences and paleosoils can be seen. Correlation between the wells is shown in *Fig 25* and *Fig 26*.

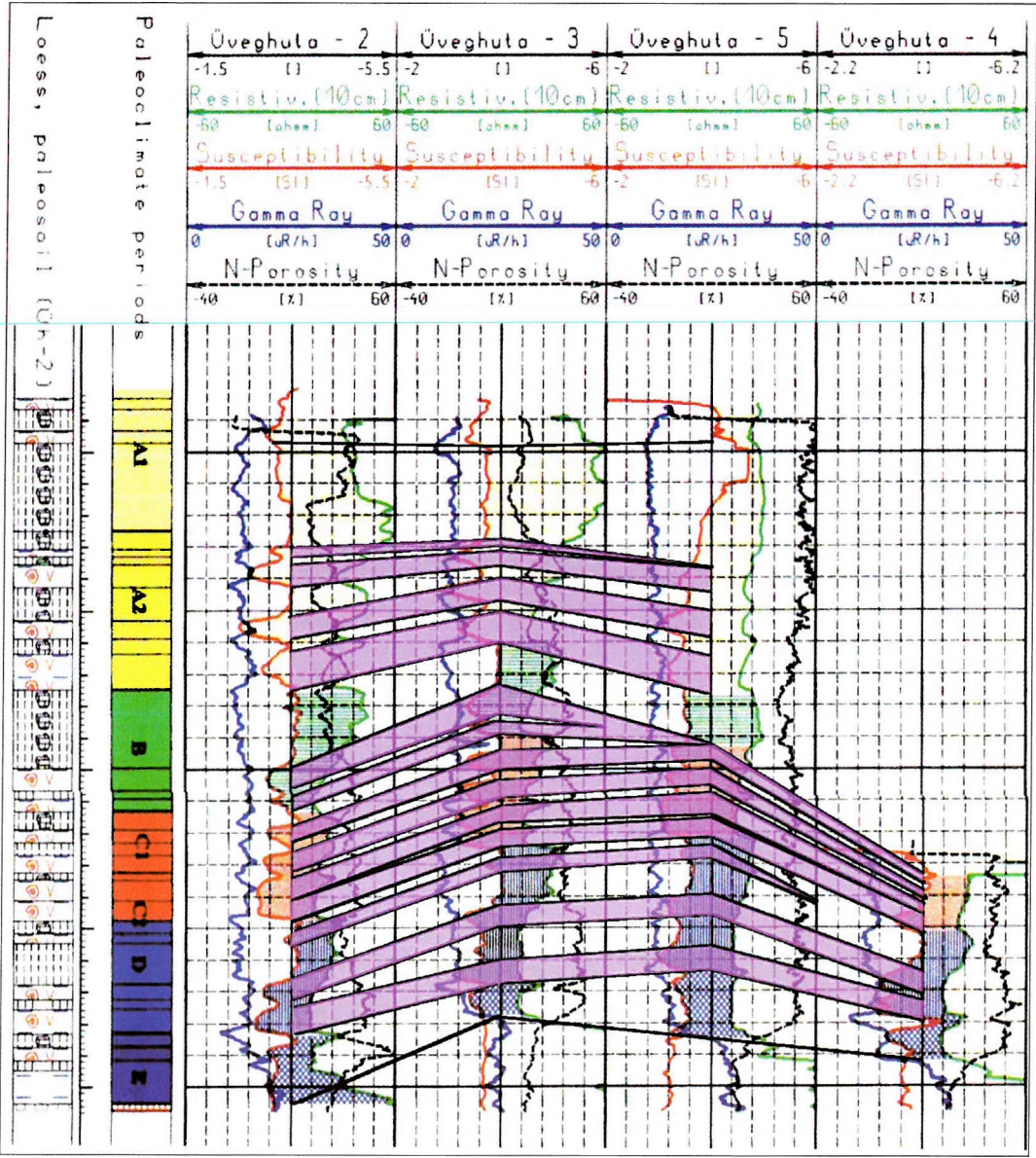


Fig. 25. Correlation plot along the closed profile of boreholes Üh-2, Üh-3, Üh-5, Üh-4.
The red layers are the paleosols

25. ábra. Korrelációs szelvény az Üh-2, Üh-3, Üh-5, Üh-4 fúrások alkotta zárt vonal mentén. A vörös sávok a paleotalajokat jelelik

Leese, potesall (U4-5)

Potential waste periods

Uveghuta - 5	Uveghuta - 22	Uveghuta - 2	Uveghuta - 23	Uveghuta - 6
Resistivity 10 cm (ohm-cm)				
Susceptibility (SI)	Susceptibility (SI)	Susceptibility (SI)	Susceptibility (SI)	Susceptibility (SI)
Gamma Ray (GR/k)				
N-Porosity (%)	N-Porosity (%)	N-Porosity (%)	N-Porosity (%)	N-Porosity (%)

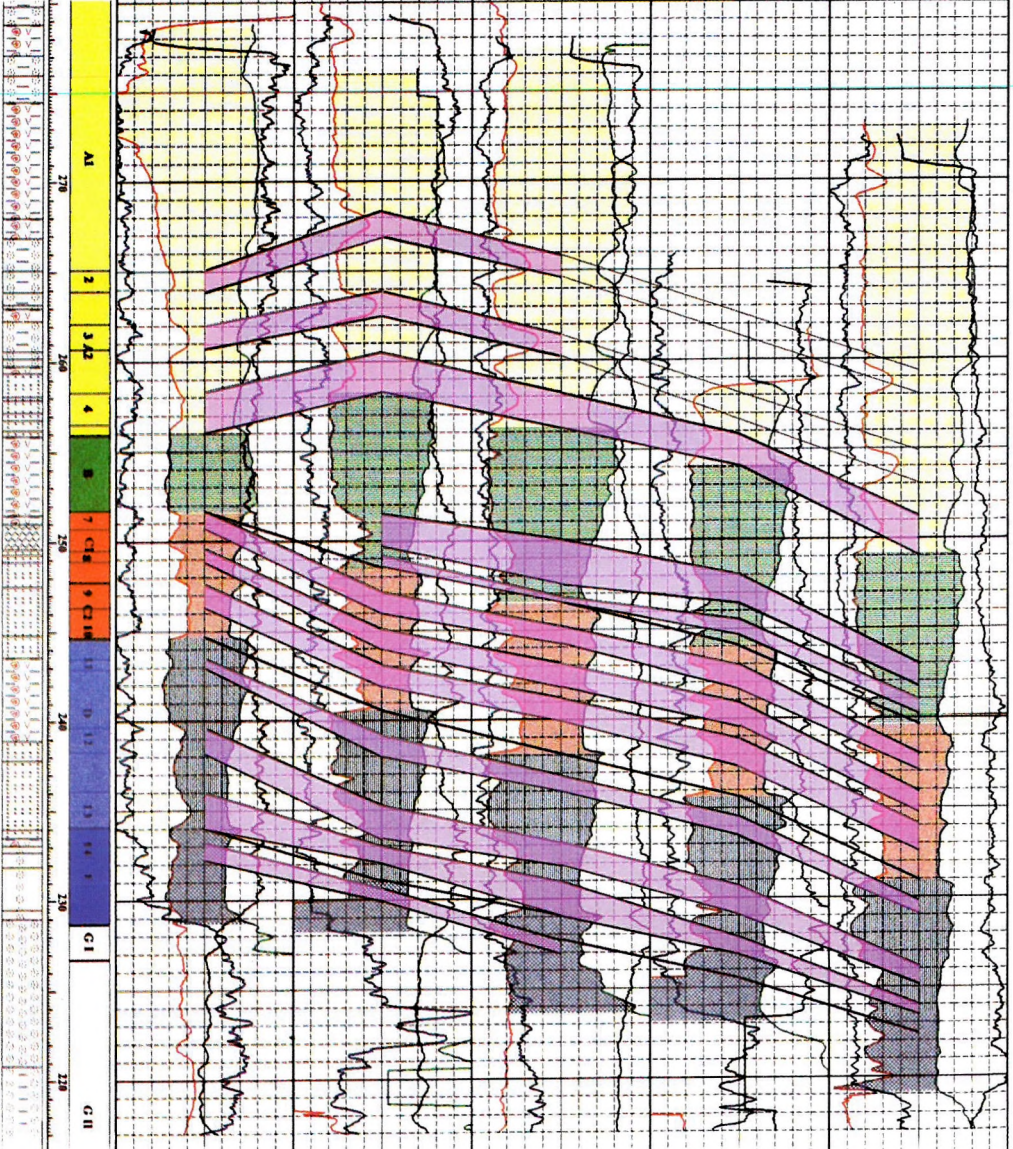


Fig. 26. Correlation plot along South–North profile (Üh–5, Üh–22, Üh–2, Üh–23, Üh–6).
The red layers are the paleosoils

26. ábra. Korrelációs szelvény az Üh–5, Üh–22, Üh–2, Üh–23, Üh–6 fúrások mentén. A
vörös sávok a paleotalajokat jelölik

5.2. Principles of the correlation attempts within granite

Naturally the altered crust of granite is not a stratified medium, but because of the existence of the depth trends of the physical parameters in connection with the surficial effects the parts of it might be described as pseudo layers.

The basis for the correlation was the electrolog and the acoustic log because the degree of alteration of rock is indicated in different ways by them. The electrolog shows the changes in specific surface and therefore it cannot distinguish the disintegrating detritus and the highly fractured and chemically altered granitoid rocks. Interpretation of surface geophysical measurements is frequently controversial in the weathered zone of the granite body. In our opinion, the key to solving the contradictions can be provided by the integrated study of geophysical acoustic and electrical well-logging measurements. The largest differences between, on the one hand, the shape of the logs of acoustic parameters and the parameters derived from that, and, on the other hand, the shape of logarithmically plotted resistivity logs are in the upper part of the weathered zone (**G I**, **G II**) (Fig. 27.). In the waveforms shown in the figure, compressional wave velocity (V_p) and electric logs of four wells are plotted in the weathered zone of granite. From experience it is known that a jump-like increase in electrical resistivity indicates the top of the sequence consisting of granite material, while from the acoustic point of view the boundary between the brecciated granite (**G II**) and chemically altered solid rock (**G III**) can be considered the boundary of the granite body. The most probable explanation for this is that zone **G III** is a difficult formation for acoustic measurement whereas **G II** is not, therefore it is the depth of strongest change for sonic measurement, while the strongest change of specific surface can be found at the top of zone **G I** because the granite gravel is coarser than its covering sediments.

6. 3-D axonometric representation of the selected site

We have constructed — and represented axonometrically — from available well-logging, engineering geophysical sounding and refraction seismic observation data a spatial model of the vicinity of the selected site of Üveghuta [ZILAHÍ-SEBESS, LENDVAY 1998] using the program 3-D

View for Windows developed by Petrosoft Ltd. (Hungary). The primary aim of 3-D representation was the spatial representation of units within the sedimentary sequence overlying the granite and the stratification of the granite's alteration cover. The model can be viewed from different visual angles, and computer-programmed arbitrary sections can be made from it.

We considered the surface of fresh granite, four layers within the granite's alteration zone [ZILAHÍ-SEBESS et al. 1998], and seven overlying layers overlying the granite surface in the model. In the model, the thickness of the granite's alteration zone determined in wells drilled in the valleys was also used. Because the loess horizons were identified only in the wells drilled on the hilltops, the thickness of the lowest loess horizon depends on changes in the granite's surface: its top is nearly horizontal and the stratification above it intersects the valley walls. We closed the model with a plane taken arbitrarily (at a depth of 200 m). *Fig. 28* shows the shape of layer boundaries extrapolated to the area; for clarity the surface representing the present relief is also shown.

The most important result of 3-D representation — also taking into account the construction of the geological model — is that the lower layers of loess do not follow the surface of granite, but an equalizing level above it, after the formation of which there were no tectonic movements within the site, only a tilt of smaller scale can be imagined. The **E** horizon of loess stratigraphy fills in the depressions in the granite, and based on the interpretation of refraction seismic profiles it is very likely that the zone had already formed before the development of unit **D**, i.e. the first real loess horizon. Because the Tengelic Red Clay identifiable with unit **E** is a pre-glacial formation, the formation of rubble may also be older than the Ice Age.

We can conclude from this that the granite was already covered before the period of loess formation. It is difficult to detect the Tengelic Red Clay with well-logging measurements because its properties make it similar to the lower loess sequence, but its presence in all descriptions has been verified geologically [CHIKÁN et al. 2000, MARSÍ 2000].

7. Conclusion

It is a complex exploration task to make a decision on the geological suitability of a site for a radioactive waste deposit. In view of this a wide

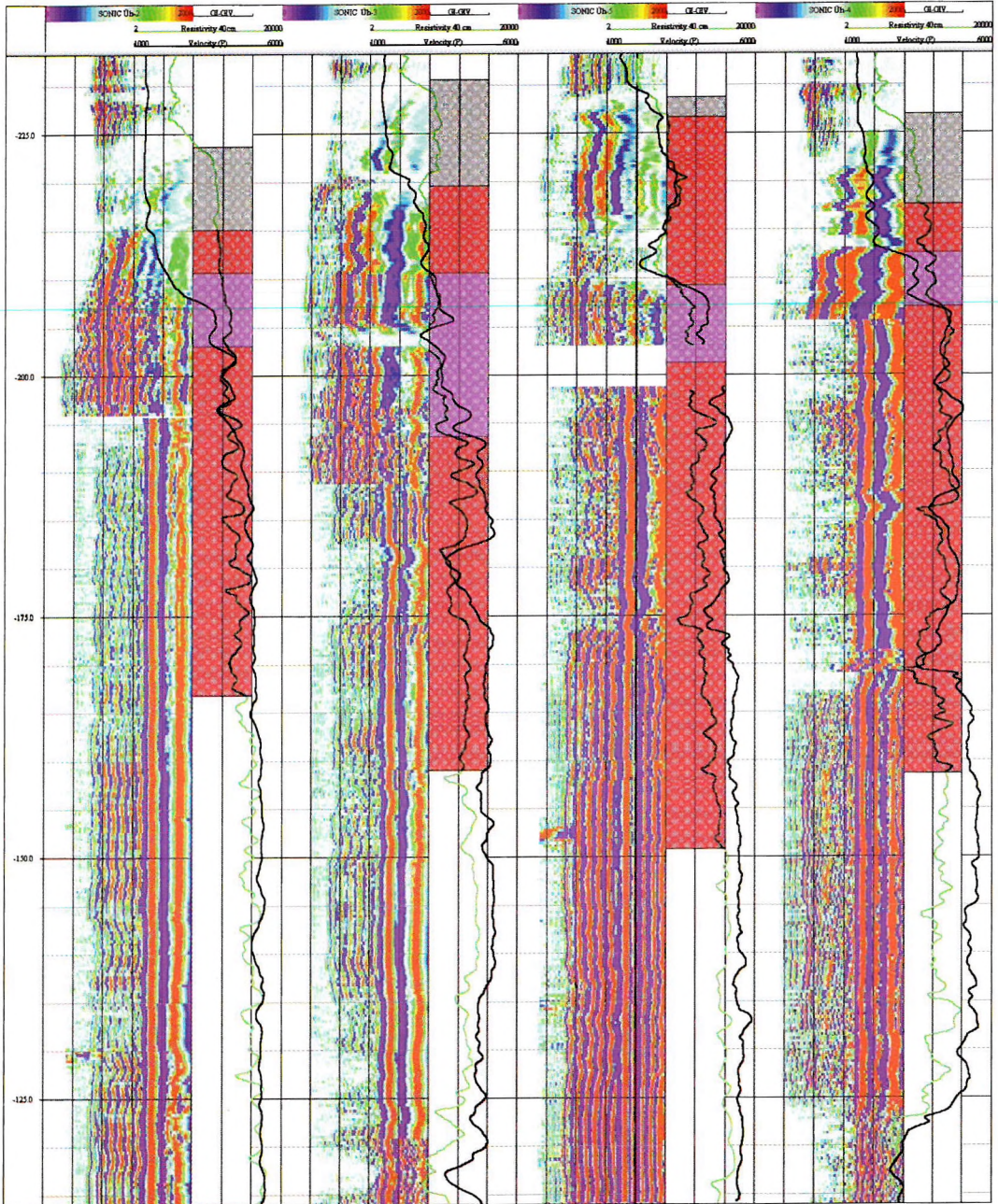


Fig. 27. Correlation plot along the closed profile Üh-2, Üh-3, Üh-5, Üh-4. The zones of weathering crust are marked with different colours in each borehole

27. ábra. Korrelációs szelvény az Üh-2, Üh-3, Üh-5, Üh-4 fúrások alkotta zárt vonal mentén. A mállási kéreg zónáit különböző színek jelölik az egyes fúrásokhoz tartozó litológiai oszlopokban

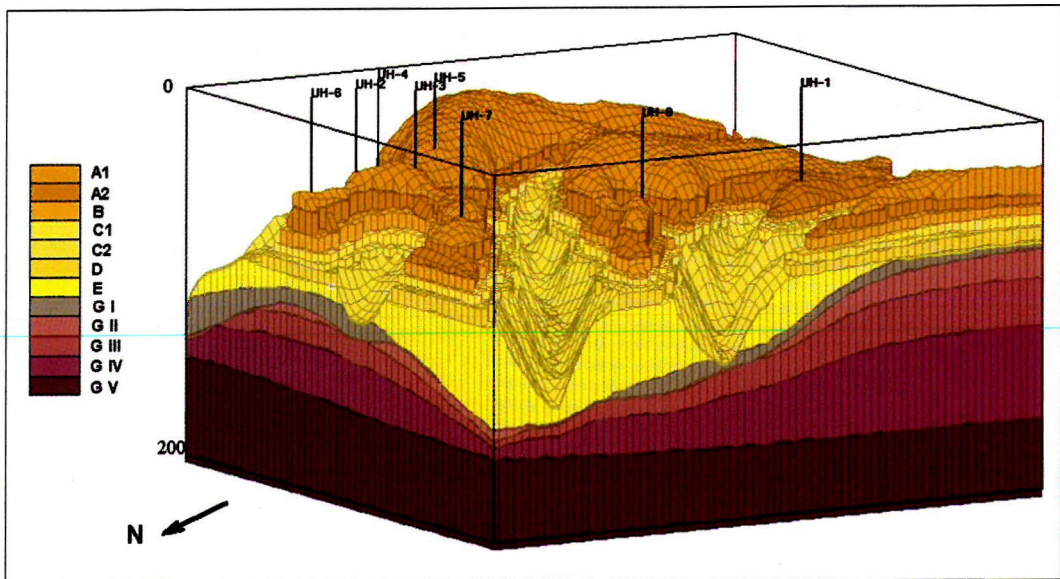


Fig. 28. Geological section of the area in 3-D representation

28. ábra. A terület 3-D földtani metszete

range of geological, geophysical, laboratory and hydrological investigations were used. Well logging has proved to be very effective among them. Integrated measurements were performed in seven boreholes deeper than 300 m deep and in about twenty boreholes of depths 10–50 m. It is obvious that lithological and geotechnical interpretation of each borehole can only be done using the well logs and making correlations between the boreholes. In addition, basic data were provided by well logging and production tests for the surface geophysical methods, crosswell logging, core orientation, packer location for hydrological tests.

The most important results of interpretation are:

—*identification and correlation of the sediment cycles in relation to quaternary paleoclimatic changes*

To identify the larger units of correlation electrical resistivity measurements are the most effective. Soil genetic horizons **A** and **B** can be detected by means of magnetic susceptibility measurement, horizon **C** does not differ from the other parts of loess.

—*dividing of weathered zone in granite*

Different parts of the granite's weathered zone can be distinguished based on geophysical well-logging measurements, primarily by means of acoustic waveform and electrical resistivity logs. Distribution of physical parameters within the weathered zone may play a significant role in interpreting surface measurements, too. Seismic refraction indicates the top of the solid rock in zone **G II**. For surface electrical and electromagnetic methods zone **G I** — i.e. the top of the formations of granite material — means the top of the granite body, whereas the top of **G V** is the top of fresh rock free of surface effects.

The two upper zones practically behave as coarse, hardly cemented sediment from the viewpoint of acoustic wave propagation, shear waves are not generated in them. Resistivity only slightly changes at the boundary between **G II** and **G III** because the specific surface of rock also changes only slightly. These two zones cannot be studied utilizing the acoustic borehole televiewer.

The lower part of the weathered zone consists of hard, fissured and altered rocks, in which shear waves can be generated. Electrical resistivity showed a crucial change at the bottom of zone **G III**. Due to the unevenness of the borehole wall no information could be obtained from zone **G III** using the BHTV: such measurements are feasible only downwards from the top of zone **G IV**.

—*location of fluid inflows*

Resistivity measurement is sensitive to the fissure system with argillaceous alteration which is imperfectly filled in with calcite veins, and to the hydrologically certainly inactive one which is filled in with ion-rich bound water.

—*detection of fractured zones*

From acoustic waveform measurement, in addition to the detection of fractured zones, velocities of the longitudinal wave (V_p) and transversal wave (V_s) and from these elastic rock parameters can be determined. Based on the BHTV measurements it can be identified which of the fractured zones marked out on the basis of acoustic and resistivity measurements contain open fissures, thus they are potential water conductors.

—*the quality of connection between the inflows and fracture system*

The inflow does not take place at each fissure and the degree of inflows is not always closely connected with fissure size.

—*quantitative characterization of small inflows*

The heat pulse flow measurement indicates places of inflow in the individual wells with good reliability and satisfactory details and the associated yields. Reliability of the yield values is generally good. Heat pulse flow measurements provide a good means of completing the short and long term packer and interference investigations. Their main advantage is that they are relatively quick and they also uniformly map the whole well.

—*evaluation of the true orientation of major faults*

Fissure direction statistics have been constructed based on BHTV measurements and we have made an attempt to determine the position of the major fracture zones which supposedly exist further away from the borehole, too.

Acknowledgement

I should like to thank all of the support in this study to Zoltán Balla for providing the opportunity of taking part in the geological exploration of 'Final disposal of reactor-generated low and intermediate level radioactive waste'. The complexity of this exploration not only provided well log analysts with a good chance to develop a means of evaluating nearly all of the methods but it was also a good way to introduce new methods. Moreover it

enabled us to gain more experience on fractured rocks. Grateful thanks are extended to Gábor Szongoth, Zoltán Kasza and István Tóth of Geo-Log Ltd. for the excellent measurements and support of this study.

REFERENCES

- BUCSI SZABÓ L., DRAHOS D., LENDVAY P., SZONGOTH G., ZILAHÍ-SEBESS L.: 1997: Well-logging investigations in a geological survey with the objective of locating a radioactive waste deposit site (in Hungarian). Annual Report of the Geological Institute of Hungary, 1996/II, 1997. pp. 307–312
- CHIKÁN G., PRÓNAY Zs., ZILAHÍ-SEBESS L.: Geological interpretation of the Üveghuta–24 (Üh–24) well. MÁFI Annual Report, 2000 (in press)
- CLAVIER C., COATES G., DUMANOIR J.: 1977: The theoretical and experimental basis for the 'dual water' model for the interpretation of shaly sands. Soc. Pet. Eng., AIME, paper No. 6859
- FLORINDO F., ZHU R., GUO B., YUE L., PAN Y., SPERANZA F.: 1999: Magnetic proxy climate results from the Duanjiao loess section, southernmost extremity of the Chinese loess plateau. *Journal of Geophysical Research* **104**, B1, pp. 645–659
- MARSI I.: 2000: Geology of overlying beds of granites in the eastern part of the Mórággy Hills. Annual Report of the Geological Institute of Hungary 1999, 2000, pp. 149–162
- MAZAUD A., LAJ C., BARDE E., ARNOLD M., TRIC E.: 1999: A geomagnetic calibration of the radiocarbon time-scale. (*In*: WALLACE E. B. ed. *The Last Deglaciation: Absolute and Radiocarbon Chronologies*. Broecker Series I: Global Environmental Change, Vol. 2)
- MESKÓ A.: 1995: Elastic waves in the Earth. Akadémiai Kiadó, Budapest, 184 p.
- O'REILLY W.: 1984: Rock and mineral magnetism. Blackie, New York, 220 p.
- ZILAHÍ-SEBESS L.: 1999: Well log interpretation of Üh–22 and Üh–23 and the feasibility of correlation between Üh–2, Üh–3, Üh–4, Üh–5 and Üh–6 wells (in Hungarian). Report commissioned by the Geological Institute of Hungary in the framework of the PHARE Project R4. 09/94 'Final disposal of reactor generated L/IL radioactive waste'. Manuscript. Eötvös Loránd Geophysical Institute of Hungary, Budapest
- ZILAHÍ-SEBESS L.: 1999: Well logging (in Hungarian). *In*: BALLA Z., DUDKO A., GYALOG L., HORVÁTH I., KOVACS-PÁLFFY P., MAROS Gy., MARSI I., PALOTÁS K., MOLNÁR P., TUNGLI Gy., BRADLEY Gr., MACDONALD B., HERMANN L., PRÓNAY Zs., TOROS E., ZILAHÍ-SEBESS L., SZONGOTH G.: 1999: Reposition of low and intermediate nuclear waste deposits. 1999 Volume I. Manuscript. Eötvös Loránd Geophysical Institute of Hungary, Budapest
- ZILAHÍ-SEBESS L., KASZA Z., TÓTH I.: 1998: Correlation based on well logs in the sedimentary cover of granite and possibilities for correlation in granite (in Hungarian). Report commissioned by the Geological Institute of Hungary in the framework of the 'Final disposal of reactor generated L/IL radioactive waste, Site exploration and suitability assessment'. Manuscript, Eötvös Loránd Geophysical Institute of Hungary, Budapest
- ZILAHÍ-SEBESS L., LENDVAY P.: 1998: Three-dimensional geological model of the Üveghuta study area (in Hungarian). Report commissioned by the Geological Institute of Hungary in the framework of the 'Final disposal of reactor generated L/IL radioactive

waste. Site exploration and suitability assessment'. Manuscript, Eötvös Loránd Geophysical Institute of Hungary, Budapest

ZILAHÍ-SEBESS L., LENDVAY P., SZONGOTH G. 2000: Division of Quaternary formations and their characterisation based on physical properties at the Üveghuta site (in Hungarian). Annual Report of the Geological Institute of Hungary 1999, 2000, pp. 171–184

ZILAHÍ-SEBESS L., MÉSZÁROS F., SZONGOTH G. 2000: Characterisation of fracture zones in granite, based on well-logging data (in Hungarian). Annual Report of the Geological Institute of Hungary 1999, 2000, pp. 253–266

ZILAHÍ-SEBESS L., RIGLER Gy., SZONGOTH G. 2000: Division of the weathering crust of Üveghuta granite based on well logging data (in Hungarian). Annual Report of the Geological Institute of Hungary 1999, 2000, pp. 209–224

ZILAHÍ-SEBESS L., SZONGOTH G. 1999: Well logging methods in investigation of a granitic site for radioactive waste. 61st EAGE Conference & Technical Exhibition, 7-11 June 1999 Helsinki, Extended Abstracts p. 585

Mélyfúrás-geofizikai módszerek a gránitba telepített radioaktív hulladék-tároló vizsgálatára

ZILAHÍ-SEBESS László

A jelen tanulmány a mélyfúrás geofizikai módszerek alkalmazási lehetőségeit mutatja be kis és közepes radioaktivitású veszélyes hulladék elhelyezésére irányuló földtani kutatás során. A gránitot fedő üledékekben a gránit mállási kérgében és az üde gránitban egyaránt történtek mélyfúrás-geofizikai vizsgálatok. A hagyományos mérések mellett két, Magyarországon az olajiparon kívül, új mérési módszert — az akusztikus lyukfaltelevíziót (BHTV) és a hőimpulzusos áramlásmérést (HPF) — is bemutatunk. A gránitot fedő üledékes összletben az elektromos ellenállás ciklikus változása a múltbeli éghajlat-változásokkal kapcsolatos. A lösz összleten belül a paleotalajok kimutatása a mágneses szuszeptibilitás mérésen alapul. A gránit mállási kéregbeli bontottságának fokát a közetrugalmassági jellemzőkkel kapcsolatban levő geofizikai paraméterek, mint a V_p és V_s valamint az elektromos ellenállás mélység trendjeivel írhatjuk le. Az üde gránit repedezett zónáit és mállási kérgének alsó részét a fizikai paraméterek és a BHTV repedés indikációk statisztikai és térbeli eloszlásával jellemezzük. Az egyes fúrásokban hőimpulzusos áramlásmérővel ki lehet mutatni az áramlásmérő szonda érzékenységi küszöbe alatti kis vízbeáramlásokat (l/lmin alatt) is. A fúrások közti földtani korrelációt a negyedidőszaki üledékes összletben és a gránit mállási kéregben végeztük el. A mállási kéregbeli korreláció kevésbé jellemző a fúrások közti térre, mint az üledékekben, mivel a zónái nem valódi rétegek, így nincs éles és térben lassan változó határfelületük és ezért a vastagságuk két fúrás közt tág határok közt változhat.



ABOUT THE AUTHOR

László Zilahi-Sebess graduated in geophysics at ELTE in 1980. He has been working with ELGI since 1980. He is principally engaged in the interpretation and methodological research related to well logging. He is one of ELGI's chief well log analysts. In 1991 he took a further degree and graduated as a well logging engineer from Miskolc University. From 1992 to

1996, he worked at the Petroleum Research Center in Tripoli, Libya. Since 1996 he has taken part in the geological–geophysical site exploration for low and intermediate nuclear waste disposal. Ever since the early 1980's, he has been dealing with the petrophysical properties of sediments under compaction.

Theoretical and statistical investigation of elemental concentration distributions determined by laser-induced plasma atom emission spectra on geological samples

László ANDRÁSSY*, László ZILAHÍ-SEBESS* and Levente VIHAR**

The principal objectives in utilizing laser-induced plasma spectroscopy (LIPS) for studying geological samples were to determine the mineral composition of pulverized drill cores and to study the inhomogeneities deriving from mineral (grain) distribution. Experimental measurements on selected samples with the LIPS instrument as well as theoretical model calculations were carried out during the three-year-long project. Concentrations were determined by calibration functions computed from LIPS measurements on experimental calibration standards and laboratory measurements by inductively coupled plasma atom emission spectroscopy (ICP AES). Parameters of the calibration functions were calculated from the peak amplitudes of spectrum-lines characteristic of the element in question. The amplitudes were determined from emission spectra induced by single or repeated laser shots (average spectra) at points selected by a sampling strategy characterized by sampling intervals. Statistical calculations were directed towards determining the accuracy of elemental concentrations. Statistical tests were carried out to describe the stability and reliability of the LIPS instrument. The relative stability error belonging to a given elemental concentration was determined from the energy distribution of the Nd:YAG laser energy source and the amplitudes read from 50 emission spectra of extra-pure Al and Cu samples, as well as the calculated concentrations.

The areal distribution of elements in drill-cores were studied by concentration maps constructed from LIPS measurements along parallel profiles. Tests on the penetration depth of repeated laser shots and mineral composition changes with depth were carried out by means of positioned measurements on thin sections. Comparisons were made of the concentration results of LIPS measurements with those of chemical analysis.

Keywords: laser methods, plasma emission spectroscopy, element oxide concentration, calibration, statistical testing

1. Instrumentation and methodology of laser-induced plasma spectroscopy in the literature

One can find many publications on the application of laser technology in geology and environmental protection. They report, however, mainly on

* Eötvös Loránd Geophysical Institute of Hungary, H-1145 Budapest, Kolombusz u. 17–23

** OPLAB kft. H-1221 Budapest, Arany János u. 115

Manuscript received: 8 Nov. 2000.

results of experimental measurements in laboratories. For determining the elemental concentration of compressed pulverized (homogenized) drill-cores and soil samples the following methods are available: chemical analysis, atom absorption spectrometry (AAS), inductively coupled plasma atom emission- (ICP AES) and mass-spectroscopy (ICP MS). Although they require long, complicated and expensive sample preparation all these methods provide high accuracy and low-detectability thresholds (ppm, ppt).

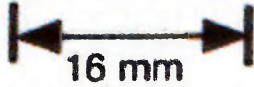
The laboratory method of laser-induced fluorescence was developed by KWANG [1989] to determine trace elements such as uranium, europium and samarium. The fluorescence emission spectra were detected by an Yvon-3 spectrofluorimeter and a nitrogen laser was used as source. To foster fluorescence induction, some agents were used in solution form.

A laboratory laser-induced micro-analytical method (LMA) was developed by MOENKE et al. [1989] for the determination of elemental composition of iron-manganese concretions of the Baltic Sea. For plasma induction in atom emission spectrometry (AES) a Q-switched ruby laser was applied. The solid samples were placed on the objective table and the induced spectra were studied by a PGS2 spectrograph.

Recently, two publications report on the development of field instruments using laser spectroscopy for the quick determination of the elemental composition of untreated metal- and soil samples [YAMAMOTO et al. 1996 and CHINNI et al. 1998]. A research team has planned to send in 2002 such an instrument to Mars, where — with the help of the Pathfinder robot and remote sensing technology — they hope to be able to analyse the elemental composition of surrounding rocks within a 19 m radius circle (see *Fig. 1*, reproduced from PINI [1999]).

In Hungary, geological and environmental application of laser-induced plasma atom emission spectroscopy started in 1993, sponsored by the Hungarian Scientific Research Fund (OTKA) [ANDRÁSSY et al. 1993 and 1998]. Research was carried out partly in the laboratories of Janus Pannonius University, Pécs, using an OSMA spectrometer, and partly in ELGI, Budapest, by constructing a portable laser-induced plasma spectrometer (LIPS) [ANDRÁSSY et al. 1995/a and 1995/b]

The basic problems of using laser-induced plasma atom (ion) emission spectrometry on geological samples are the 'micro' mineral composition of rocks and the point-like ablation effect and laser induction of the Nd:YAG laser (KIGRE Inc.). This means that during measurements the plasma and



Laser plasma is formed on a soil sample in a surrounding atmosphere of 5 t CO₂ to simulate the conditions on Mars. Courtesy of Dave Cremers.

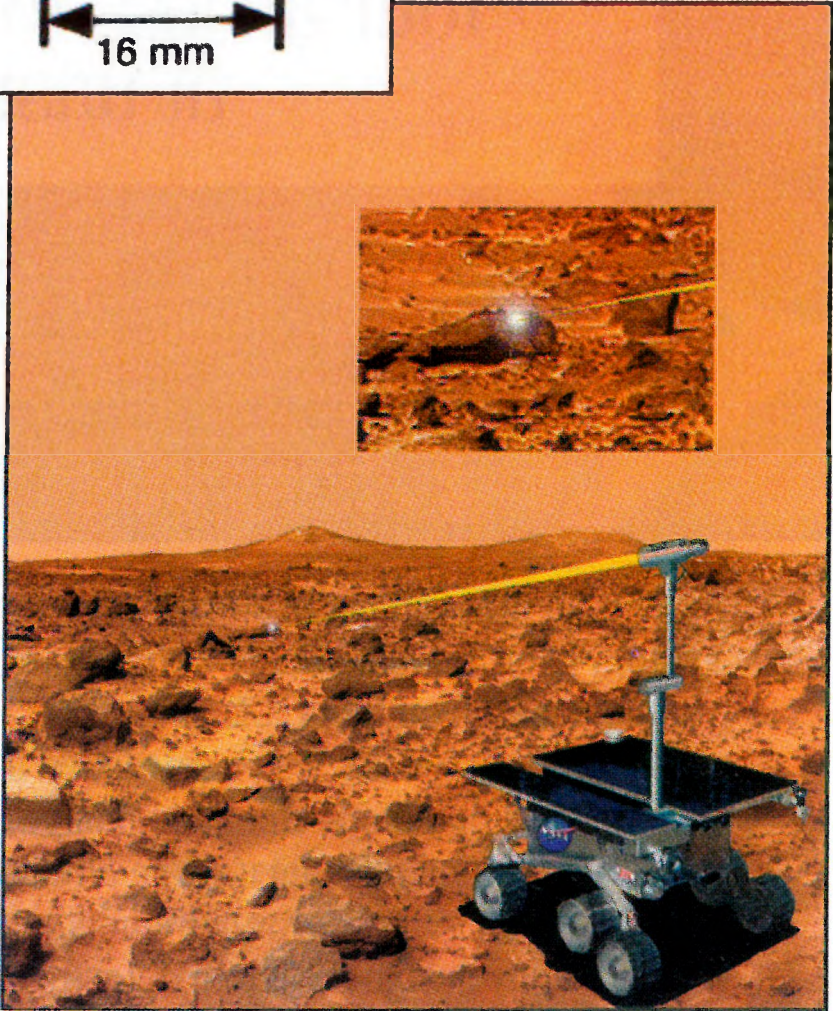


Fig. 1. Laser plasma and planned Mars experiment, figure taken from [PINI 1999]

1. ábra. Lézer plazmakeltés talajmintán. 5 t CO₂-t tartalmazó légkörben, a Marson található feltételek szimulálására [PINI 1999 nyomán]

the subsequent emission give information solely on the mineral ingredient hit by the laser ray, and not on the bulk mineral composition. Therefore our main task in our three-year research project was to study the elemental composition of pulverized drill cores and the inhomogeneities deriving from the distribution of mineral grains.

2. Theoretical model calculations for pulverized homogenized samples

Since only small volumes are analysable with laser-induced plasma spectroscopy, a sampling strategy — based on theoretical model calculations — is necessary to make the results representative. Geological samples, in spite of their pulverized homogenized form, are inhomogeneous to some extent — depending on the grain distribution. Frequently the target matter is represented by larger grains of higher density than the rock matrix, e.g. the majority of sulphide contamination. As the photomicrograph of a homogenized sulphide standard (*Fig. 2*) shows, the distribution of the target matter is not uniform. To determine the elemental concentration rep-

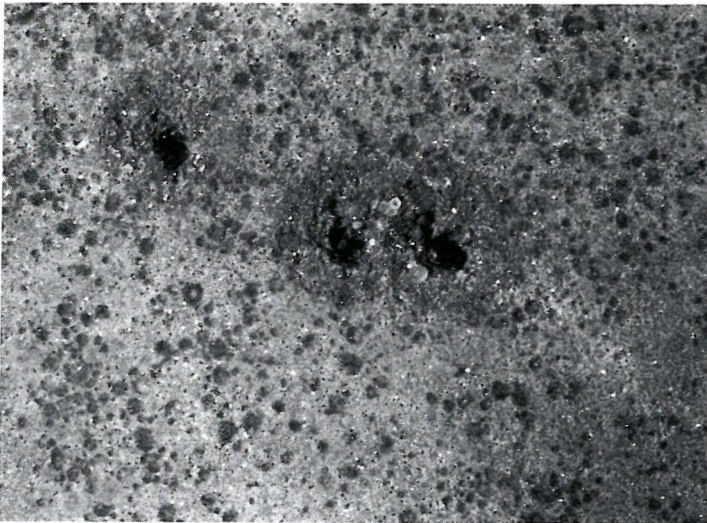


Fig. 2. 16-fold magnified photo of a sulphide standard. The black spots are the laser craters, while the darkened rings around them show their melting effect

2. ábra. Szulfid etalon 16-szoros nagyítású mikroszkópikus felvétele. A fekete foltok a lézer kráterek, az ezeket körülvevő elsötétített gyűrű az olvasztó hatás elterjedését jelzi

representing the whole sample, we have to set up distribution models which take into consideration the inhomogeneities and the size of the volume, in order to provide directives for an appropriate sampling strategy.

For setting up a sampling (laser shot) strategy the probability of a single-shot hit versus concentration is examined. The concept of *probability of hit* is used because the target matter is linked to grains in irregular distribution. To set up the theoretical model, the photomicrograph of Fig. 2 taken after LIPS measurements on the sulphide standard, was used. It shows the pyrite grain distribution and the geometry of the craters caused by the laser shots. The absorbed laser energy, locally heating the rock, causes melting and emission of steam, resulting in superficial recession and creation of craters. These craters are somewhat elongated with their diameter between 0.2 and 0.5 mm (average: 0.35 mm), whereas the diameter of the pyrite grains scatter between 0.06 and 0.18 mm (average: 0.12 mm). The average diameter of the craters being about three times that of the pyrite grains is favourable from the aspect of representative sampling.

The high-temperature, plasma-state matter torn from the crater melts the surrounding rock. This melted rock appears in the photograph by changed colour. The width of the alteration ring is about 1 mm, meaning the area of the crater is only 1/9 part. In the computation of the sampling strategy this alteration ring is not taken into account.

According to experience the pyrite grains can be found in irregular distribution on the surface of the sample, on the periphery of smaller or greater polygons (see Fig. 3). The inner diameter of these polygons is between 0.6 and 1.2 mm — 0.6 mm being the more frequent — meaning the diameter of the empty area within the polygon. In the case of low concentrations, this diameter is on average about double that of the craters. It is presumed that the larger grains are driven out from among the smaller ones, and — similarly to cryoturbation and to the formation of polygon soils — form characteristic polygons. The size of the polygons is thought to depend mainly on the concentration of pyrite grains in the sample and on the mean grain size. We have modelled the polygons by hexagons. In the model calculations the size of the polygons is determined from photomicrographs, supposing that only the visible grains contain the target elemental species.

In the pyrite-containing sample, the shortest distance between grains is 0.06 mm, and the diameter of the largest area of 100 % hit is about 1 mm, with a coverage of 50 % by pyrite grains. The width of the zones separating the polygons is about 0.1 mm, with a coverage of 70 % by pyrite grains.

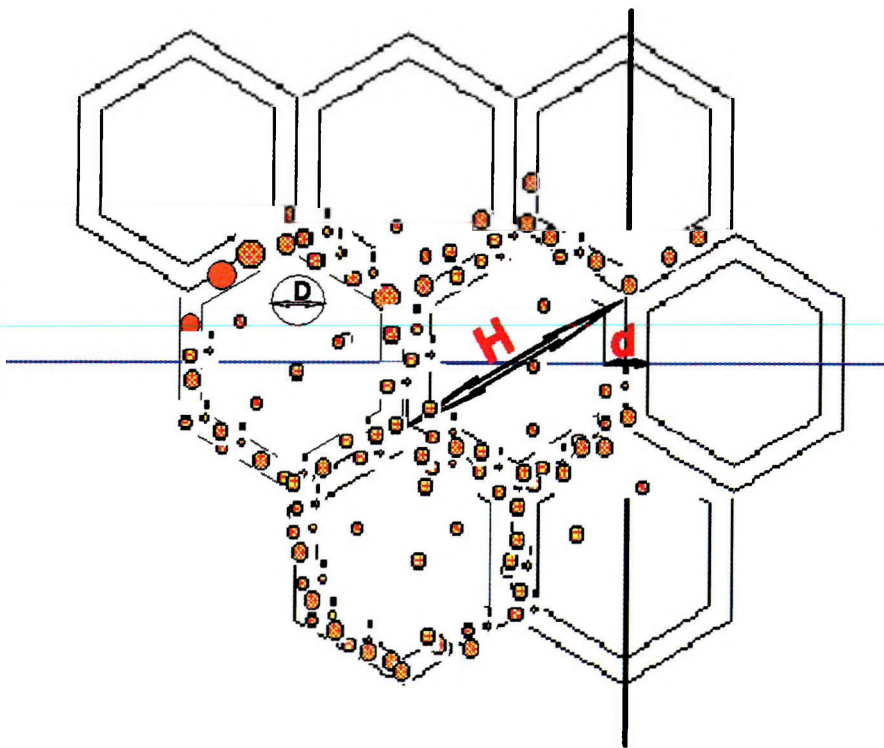


Fig. 3. Model of polygon arrangement of the ore particles on the surface of pulverized and compressed samples

H — average diameter of polygons; *d* — average width of the strips containing prevalent part of the ore particles; *D* — diameter of crater caused by the laser shot

3. ábra. Ércszemcsék elhelyezkedésének poligon elrendezésű modellje porított és préselt minta felületén

H — a poligonok átlagos átmérője; *d* — az ércszemcsék döntő részét tartalmazó sávok átlagos szélessége; *D* — a lézerlövés okozta kráter átmérője

As presumed, the diameter of polygons — in the case of two components (matrix and ground target element) — is proportional to the concentration of the target material. Accordingly, the effective concentration can be calculated from the period-length of concentration-variation along the line of measurement. An important question is whether the target element is present only in the big grains clustered along the periphery of the polygons. To answer this question, the zero level of the target element has to be determined. Our preliminary knowledge is limited to knowing that a part of the big grains contains the target element. Thus a mean concentration (C_{00}) can be computed for the material in polygonal patterns from the peaks of distributions detected along the line of measurement. Absolute concentration can be calculated from the average size of the polygons. As the real content of the grains is not known, the results of laser spectroscopy provide information on the size of polygons. Supposing the polygon system to consist of hexagons, let us mark their largest diameter with H and let d be the width of dividing zones containing the grains of the target element. Consequently, the relative area of the zone along the periphery of polygons is

$$1 - (H - d/\cos 30^\circ)^2 / H^2 = C_{10},$$

which marks the effective concentration if the concentration within the dividing zone is 100%. The absolute concentration (C_{11}) can be given as the product of the concentration within the dividing zone and the coverage:

$$C_{11} = C_{00} * C_{10} .$$

If we have no other information except that received from spectroscopy, the intervals between shots have to be reduced along the line of measurement. This operation has to be repeated until the difference between the mean values is reduced below a given threshold. Thus we get a mean value along the line of measurement, which still does not represent the real concentration. It is necessary to carry out the measurements in at least two directions because of the limited size of the sample and the anisotropy deriving from the polygon system. In the case of an entirely hexagonal system, the extreme cases of directional concentrations are, if $d \ll H$

$$C_{00max} = (H + 4.62d) / 3H \quad \text{and} \quad C_{00min} = d / (H * \cos 30^\circ)$$

If $d \geq 0.2165H$, there exists a straight line along which the maximum concentration will be found. This means that if the large grains forming the polygons contain statistically uniformly the target element, it is possible to

measure the concentration existing within the limiting zones of the polygons.

If only a few grains fall on the line of measurement, reducing the intervals between shots we can reach a concentration of $C_{00max}/3$, meaning one side of a polygon coincides with the line of measurement.

The limit of the minimum concentration is 0 if d tends to 0. If $d = H/10$, the minimum measured concentration will be $C_{00min} = 0.115C_{00}$.

It can be concluded that a line of measurement in one direction will not represent the concentration distribution (nor its mean value) even if uniform grains were to form uniform hexagons. In reality the size of the hexagons varies. Therefore it is expedient to work out a sampling strategy for a given shot number, by which — and using multidirectional measurements — the concentration values will be representative for the sample.

The above observations hold for pulverized and homogenized samples. Real geological samples (cores) need a different sampling strategy as their inhomogeneities are much higher.

The spectrum line peak amplitudes belonging to a given elemental species and the concentration values computed from them should be normalized to the spectrum of the matrix. As a result of normalization the error caused by the thermal noise of the plasma-state radiating material will be reduced. In laser spectroscopy the proportion of concentration values calculated for different elemental species may be characteristic of the material (mineral, compound), supposing that the given elements occur together. This supposition may hold with high probability because in geological samples the size of the crater is generally smaller than the size of the mineral.

3. Experimental measurements

3.1. Sample preparation

Cores do not need any preparation. Measurements can be carried out either on the superficies of the core or on its vertical cross section.

In the case of pulverized samples a simple preparation is necessary by which tablets of 20 mm diameter are produced. The dried samples are ground, homogenized and put into a cylindrical sample holder. The grist is then subjected to 10 MPa pressure by a hydraulic press (Zeiss product). All

sample preparations necessary for our experiments were carried out by the Analytical Laboratory of the Geological Institute of Hungary (MÁFI).

3.2. *Creation of standards independent of rock matrix*

Our first task was to calibrate the instrument. To this end, we needed standards containing the elemental species in question in varying concentration. Here we would acknowledge the support of the Geological Institute of Hungary for providing us with a series of bauxite, marl, metasomate and polymetallic sulphide standards, all in pulverized form. The elemental compositions of these standards were determined by X-ray diffraction and thermal analysis. From these samples we prepared with the technology described above four standards, which were complemented by two soil standards prepared by ALUTERV-FKI Ltd, in 1994. Thus six standards were at our disposal whose elemental (element oxide) concentrations were known from ICP AES laboratory measurements.

3.3. *Processing of emission spectra*

Colour plotting and qualitative as well as quantitative interpretation of emission spectra measured by a portable laser-induced plasma spectrometer were carried out by the easy to handle and flexible *Wskrom 2000* program developed by our research group. Its arithmetic features make it possible to simultaneously plot several emission spectra in the whole wavelength range (250–575 nm), and to determine the composition of the samples as well as their elemental concentration.

For a large number of measurements, the user is linked to a database to enable the necessary data processing to be carried out. The flowchart of the program is presented in *Fig. 4*.

In *Fig. 5* in the configuration of the periodic system those elements are marked with green which can be successfully determined by LIPS. Elements marked in yellow represent those whose determination is ambiguous at present; it is hoped, however, that there will be improvement in the near future as a result of instrument development. Elemental concentration is a more difficult task to determine, consequently fewer elements are amenable to it (these are marked with brown in the lower half of the figure). Because the majority of these elements are very common in rocks, their detection is important in geological exploration.

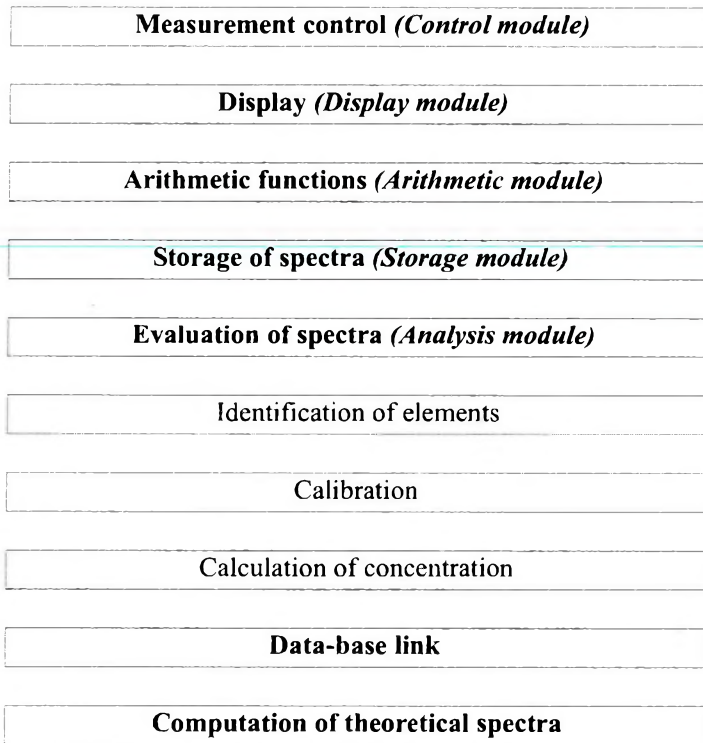


Fig. 4. Flowchart of Wskrom 2000 program
 4. ábra. A Wskrom 2000 program felépítése

For identifying the matrix- and heavy metal elements, and to calculate their concentration, a prerequisite is to know their interference-free emission spectrum lines of maximum amplitude. Comparison of the wavelengths belonging to the peak amplitudes determined by plasma atom emission spectroscopy of extra-pure metal standards with those found in published spark and plasma libraries, made the selection of the most characteristic spectrum lines possible. In *Tables I. and II.* the wavelengths of the strongest spectrum lines of spark measurements published by HARRISON [1980] and those of LIPS are compared for the major matrix elements and certain heavy metals.

3.4. Calibration technology and calculation of concentration

Quantitative analysis requires a calibration function to be determined for each element. The spectra of a minimum of three samples of varying

H																		He
Li	Be											B	C	N	O	F	Ne	
Na	Mg											Al	Si	P	S	Cl	Ar	
K	Ca	Sc	Ti	V	Cr	Mn	Fe	Co	Ni	Cu	Zn	Ga	Ge	As	Se	Br	Kr	
Rb	Sr	Y	Zr	Nb	Mo	Tc	Ru	Rh	Pd	Ag	Cd	In	Sn	Sb	Te	J	Xe	
Cs	Ba	La	Hf	Ta	W	Re	Os	Ix	Pt	Au	Hg	Tl	Pb	Bi	Po	At	Rn	
Fr	Ra	Ac																

H																		He
Li	Be											B	C	N	O	F	Ne	
Na	Mg											Al	Si	P	S	Cl	Ar	
K	Ca	Sc	Ti	V	Cr	Mn	Fe	Co	Ni	Cu	Zn	Ga	Ge	As	Se	Br	Kr	
Rb	Sr	Y	Zr	Nb	Mo	Tc	Ru	Rh	Pd	Ag	Cd	In	Sn	Sb	Te	J	Xe	
Cs	Ba	La	Hf	Ta	W	Re	Os	Ix	Pt	Au	Hg	Tl	Pb	Bi	Po	At	Rn	
Fr	Ra	Ac																

Fig. 5. In the periodic system those elements are marked with green which can be successfully detected by our present LIPS instrument, with yellow those which are hopefully detectable in the future and with brown those whose elemental concentration can be determined too

5. ábra. A periódusos rendszerben zölddel jelöltük a LIPS műszerünkkel kimutatható elemeket, sárgával azokat, amelyek a műszer továbbfejlesztésével kimutathatók lesznek, barnával pedig azokat, amelyeknek a koncentráció értékei is meghatározhatók

Al		Ca		Fe		Mg	
LIPS	Spark	LIPS	Spark	LIPS	Spark	LIPS	Spark
309.3	309.271	393.6	393.367	260.0	259.940	279.4	279.553
Mn		K		Si		Ti	
LIPS	Spark	LIPS	Spark	LIPS	Spark	LIPS	Spark
403.3	403.307	404.5	404.414	288.2	288.158	335.0	334.903

Table I. Wavelengths (in nm) of highest-amplitude spectrum lines of published spark- [HARRISON 1980] and LIPS-measurements for matrix elements

I. táblázat. Matrix elemek irodalomban publikált szikra- [HARRISON 1980] és a LIPS-mérésekkel meghatározott legerősebb spektrumvonalainak hullámhossz értékei (nm-ben)

Ag		Ba		Cu		Cd	
LIPS	Spark	LIPS	Spark	LIPS	Spark	LIPS	Spark
328.0	328.068	455.2	455.404	328.0	327.396	361.4	361.051
Hg		Pb		Sr		Zn	
LIPS	Spark	LIPS	Spark	LIPS	Spark	LIPS	Spark
366.1	366.328	406.2	405.782	407.7	407.771	328.0	327.396

Table II. Wavelengths (in nm) of highest-amplitude spectrum lines of published spark- [HARRISON 1980] and LIPS-measurements for certain heavy metals

II. táblázat. Nehézfémek irodalomban publikált szikra- [HARRISON 1980] és a LIPS-mérésekkel meghatározott legerősebb spektrumvonalainak hullámhossz értékei (nm-ben)

concentration are necessary for calibration, but to increase its reliability, it is expedient to use more. To create a calibration function we can use a minimum of one, a maximum of 20 emission spectrum peaks characteristic of the elements in the standards (at present we work with the single highest-amplitude peak). Either the selected peak amplitudes or the amplitudes of the second derivatives can be the input data for the regression. It is possible to mark out a distinctive peak, which belongs to the element present in all samples in about the same quantity. With its use many disturbing factors can be eliminated.

The target function of the regression, i.e. the calibration function, is:

$$I = A * C^k * \exp (B * C)$$

where I is the intensity of the spectrum line (its amplitude, amplitude of 2nd derivative, peak area, etc.), A , k , B are the parameters to be determined by calibration, and C is the concentration.

The dimensions of the A , k , B parameter-vectors are equal to the number of peaks. If we have three standard samples, we can compute these parameter-vectors by an equation system of three unknowns. If the number of known concentrations is higher than three, the parameter-vectors are determined by regression according to the least squares method. The unknown concentration is determined by solving the calibration function if one peak is used, and by regression if more than one peak is involved. The calculations are carried out by the *calibration* function of the Wskrom 2000 program (see Fig. 4).

For quantitative evaluation as mentioned above we needed standards containing the same elements in varying concentration, to determine the parameters of the calibration function. In the standards used for the calibration of the LIPS instrument the concentration values of the occurring matrix and heavy metal elements are respectively listed in *Tables III.* and *IV.*

Standards	Marking	Al %	Ca %	Fe %	Mg %	Mn %	K %	Si %	Ti %
Calcareous soil	Et11	11.10	7.0	4.3 0	1.80	0.1400	2.20	57.50	0.80
Acidic soil	Et13	13.00	1.2	4.40	1.30	0.1500	2.50	66.70	1.00
Bauxite	Bau	50.72	0.67	22.59	0.52	0.1300	0.04	6.63	2.49
Marl	Mar	5.96	35.78	3.23	1.70	0.0670	1.07	19.85	0.32
Metasomatite	Met	15.67	0.37	3.50	0.86	0.0530	11.30	63.35	0.55
Sulphide	Sulet	6.11	4.50	12.50	0.96	0.1800	1.99	50.03	0.29

Table III. Concentrations of matrix elements occurring in standards used for calibration of the LIPS instrument

III. táblázat. A LIPS-műszer hitelesítésére szolgáló etalonokban előforduló matrix elemek koncentráció értékei

Standards	Marking	Ba ppm	Cu ppm	Pb ppm	Sr ppm	Zn ppm
Calcareous soil	Et11	0	98	93	98	238
Acidic soil	Et13	0	98	97	98	238
Bauxite	Bau	0	45	0	140	98
Marl	Mar	470	15	16	410	95
Metasomatite	Met	685	64	11	87	82
Sulphide	Sulet	0	4500	38800	0	46400

Table IV. Concentrations of heavy metals occurring in standards used for calibration of the LIPS instrument

IV. táblázat. A LIPS-műszer hitelesítésére szolgáló etalonokban előforduló nehézfémek koncentráció értékei

As one can see from Table IV, the concentration values of heavy metals are above the detection threshold of the instrument only in the sulphide (Cu, Pb and Zn), marl (Ba, Sr) and metasomatite (Ba) standards. Thus we do not have the necessary series of standards of varying concentration of the same element.

To solve the problem, series of experimental standards were created in MÁFI's laboratory from ground sulphide ore and barite (BaSO_4) mixed with quartz sand in varying proportion. The concentration values of the thus prepared standard series are presented in Table V.

Standards	Cu ppm	Pb ppm	Zn ppm	Standards	Ba ppm
Sul1	45	388	464	Ba6	589
Sul2	113	970	1160	Ba7	1177
Sul3	225	1940	2320	Ba8	2943
Sul4	450	3880	4640	Ba9	5886
Sul5	1125	9700	0.11	Ba10	11771
Sulet	4500	38800	46400	BaSO ₄	588566

Table V. Concentrations of elements occurring in sulphide and BaSO_4 standard series used for calibration of the LIPS instrument

V. táblázat. A LIPS-műszer hitelesítésére szolgáló szulfid és BaSO_4 etalon sorokban előforduló elemek koncentráció értékei

As an example for calibration the calibration curve of Al is presented in Fig. 6, which was determined using the peak amplitudes of the 309.3 nm spectrum lines, detected in the standards of Table III, and an extra-pure aluminium metal standard. The peak-amplitude values of low-concentration elements are strongly disturbed by thermal noise and the matrix effect. Figure 7a presents the effect of thermal noise on the peak-amplitudes in the 460–500 nm range of the Zn 482.1 nm spectrum line in the sulphide standard. It can be seen that the peak-amplitude values do not follow the expected trend — due to varying thermal noise.

To solve this problem, two possibilities are at hand: *i*) the first solution is a graphic one, when the measured spectra are shifted to a common reference point, and the so-called corrected peak amplitudes are read from the diagram. This is shown in Figure 7b, where the reference point is on the right-side of the highest peak (at 483 nm wavelength). As a result, the corrected amplitude values already show the expected trend. Using these amplitude values, the calibration will be of higher accuracy. The drawback of

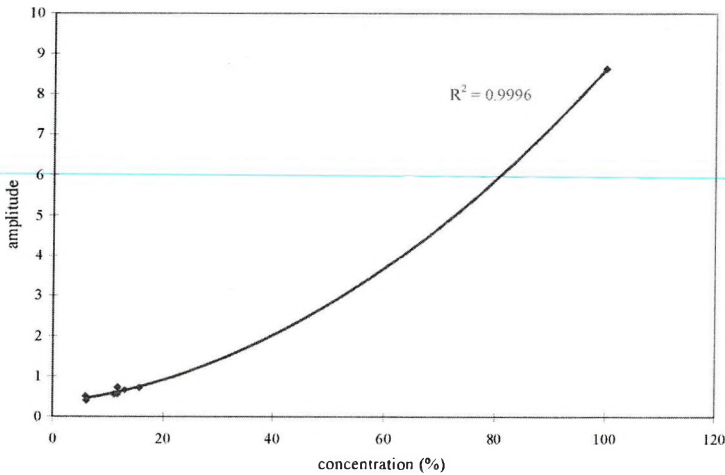


Fig. 6. Calibration curve of the LIPS instrument for Al
 6. ábra. A LIPS műszer hitelesítő görbéje Al elemre

this method is that the data processing program cannot carry out the graphic shifting and the marking out of the reference point.

ii) The second solution is the use of the second derivatives in the calibration process. The program enables the computation and use of the second derivatives, which are independent of thermal noise. All these data are presented in *Table VI*.

Standards	Concentration (ppm)	Zn amplitude measured	Zn amplitude corrected	Zn 2nd derivative of measured	Zn 2nd derivative of corrected
Sul1	464	0.3108	0.2808	0.0019	0.0019
Sul2	1160	0.3424	0.3124	0.0073	0.0073
Sul3	2320	0.3475	0.3275	0.0111	0.0111
Sul4	4640	0.3384	0.3384	0.0151	0.0151
Sulet	46400	0.3978	0.3978	0.0215	0.0215

Table VI. Comparison of measured amplitudes with those of second derivatives determined on sulphide standards

VI. táblázat. Szulfid etalonokon mért amplitúdó- és második derivált amplitúdó értékek összehasonlító táblázata

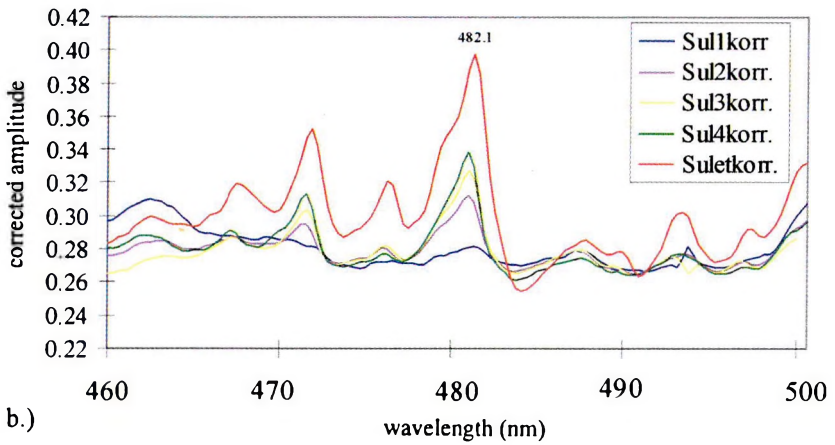
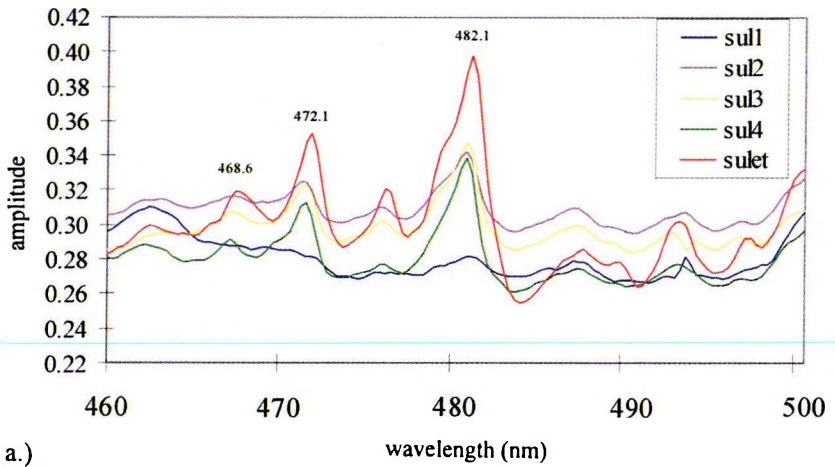


Fig. 7. Variation of peak amplitudes belonging to Zn 482.1 nm wavelength: a) as determined on a sulphide standard series, and b) their variation after correction

7. ábra. Zn 482.1 nm hullámhosszhoz tartozó csúcsamplitúdók változásai szulfid etalonsoron: a) mért értékek. b) korrigált értékek

4. Statistics of the accuracy of concentration values determined by LIPS measurements

4.1. Sampling strategy

The measurements on the samples can be regarded as a statistical set which is representative if it accurately reflects the whole of the population. To satisfy this condition we carried out the measurements on cores and pulverized standards according to a sampling strategy, including the sampling system and the sampling rate. Within the sampling systems, from the six possibilities [BÁRDOSSY 1997] we used three:

- a) random sampling,
- b) sampling along traverses,
- c) random stratified grid sampling.

Let us discuss their characteristics and our experiences.

In *random sampling*, selection of all sampling (measurement) points has the same probability. Although this is a statistically correct starting point, up to now there is no method which would guarantee the sampling points to be of totally equal rank.

As this type of sampling cannot take the mineral composition into consideration, we only used it on pulverized and homogenized BaSO_4 standard samples to check the homogeneity of the standards. These standards are two-component systems where the BaSO_4 is mixed with SiO_2 (quartz sand) to modify the ratio of the two substances. As the grain size of the two components and their distribution cannot be expected to be uniform in the samples, we get a measure on the homogeneity of the standard samples by the different sampling systems.

In the random sampling system we located randomly 5, 10 and 20 measuring points on the surface of the standard. With statistical data processing we determined the average amplitudes, their standard deviation and confidence limits. The results for standard Ba6 are presented in *Table VII*, those for standard Ba8 in *Table VIII*.

The system of *sampling along traverses* is most suitable for examining cores, where the profiles can be located on their cylindrical surface (superficies), in the vertical direction, or perpendicularly, on the horizontal top (kerf) or bottom of the cylinder, with a given sampling interval. When locating the profiles an unavoidably subjective decision has to be made regarding the visible mineral composition.

	20 points		10 points		5 points		20 points	10 points	5 points
	Si	Ba	Si	Ba	Si	Ba	Ba/Si	Ba/Si	Ba/Si
Mean μ_0	0.4602	0.7825	0.4298	0.7065	0.4245	0.7124	1.6571	1.6452	1.6333
S. dev. σ_0	0.0707	0.2545	0.0505	0.1576	0.0494	0.1503	0.4379	0.3214	0.2100
Conf. limits	0.0310	0.1150	0.0313	0.0977	0.0433	0.1317	0.1919	0.1992	0.1641

Table VII. Results of statistical analysis of amplitudes determined at randomly selected points of Ba6 standard (589 ppm Ba)

VII. táblázat. Ba6 etalonon (589 ppm Ba) véletlenszerűen kiválasztott mérési pontokban mért amplitúdó értékek statisztikus feldolgozásának eredményei

	20 points		10 points		5 points		20 points	10 points	5 points
	Si	Ba	Si	Ba	Si	Ba	Ba/Si	Ba/Si	Ba/Si
Mean μ_0	0.4652	0.9305	0.5459	1.1369	0.5067	0.9523	1.9948	2.0268	1.8868
S. dev. σ_0	0.0928	0.2643	0.0547	0.4698	0.0480	0.0569	0.3751	0.2956	0.0907
Conf. limits	0.0407	0.1158	0.0959	0.2912	0.0422	0.0499	0.1644	0.1832	0.0795

Table VIII. Results of statistical analysis of amplitudes determined at randomly selected points of Ba8 standard (2943 ppm Ba)

VIII. táblázat. Ba8 etalonon (2943 ppm Ba) véletlenszerűen kiválasztott mérési pontokban mért amplitúdó értékek statisztikus feldolgozásának eredményei

We carried out measurements with 1, 2 and 4 mm sampling intervals, in the system of sampling along traverses, on the same two BaSO₄ standards as with random sampling. As the diameters of the standards are 20 mm, with the given sampling intervals we had 20, 10 and 5 points of measurement, respectively. The results of statistics (average amplitude, standard deviation and confidence limits) are given in Tables IX and X. To decrease the noise level, we have computed at each point the Ba/Si amplitude ratio, too, in both sampling systems. These figures provide more realistic data on the elemental concentration.

Commenting on the results, it can be seen that both sampling systems provide for both standards — and for all numbers of measurements — Si and Ba amplitude averages as well as Ba/Si ratio values within the confidence intervals determined for 10 points (accepting the confidence limits computed for 10 points as reference — see Tables VII, VIII, IX and X). Accordingly, in the calibration process we can accept the averages of 5 meas-

	1 mm 20 points		2 mm 10 points		4 mm 5 points		1 mm 20 p.	2 mm 10 p.	4 mm 5 p.
	Si	Ba	Si	Ba	Si	Ba	Ba/Si	Ba/Si	Ba/Si
Mean μ_0	0.4067	0.6271	0.4034	0.6141	0.4316	0.6758	1.4983	1.5102	1.5644
S. dev. σ_0	0.0721	0.2420	0.0586	0.1368	0.0441	0.0821	0.3118	0.1380	0.0840
Conf. limits	0.0316	0.1061	0.0363	0.0848	0.0387	0.0360	0.1366	0.0855	0.0736

Table IX. Results of statistical analysis of amplitudes determined at points along a profile of Ba6 standard (589 ppm Ba)

IX. táblázat. Ba6 etalonon (589 ppm Ba) szelvény mentén kiválasztott mérési pontokban mért amplitúdó értékek statisztikus feldolgozásának eredményei

	1 mm 20 points		2 mm 10 points		4 mm 5 points		1 mm 20 p.	2 mm 10 p.	4 mm 5 p.
	Si	Ba	Si	Ba	Si	Ba	Ba/Si	Ba/Si	Ba/Si
Mean μ_0	0.4584	1.0244	0.4643	1.0184	0.4488	0.9274	2.2234	2.1659	2.0830
S. dev. σ_0	0.0849	0.2583	0.0903	0.2782	0.0322	0.0794	0.3253	0.2490	0.3181
Conf. limits	0.0372	0.1132	0.0560	0.0172	0.0282	0.0698	0.1426	0.1543	0.2788

Table X. Results of statistical analysis of amplitudes determined at points along a profile of Ba8 standard (2943 ppm Ba)

X. táblázat. Ba8 etalonon (2943 ppm Ba) szelvény mentén kiválasztott mérési pontokban mért amplitúdó értékek statisztikus feldolgozásának eredményei

urements as characteristic of the standards. For details of statistical calculations see Section 4.2.

The standard deviation values depend not only on the accuracy of the measurements, they reflect the inhomogeneities of the standards, as well. We can see from Tables VII, VIII, IX and X that in both sampling systems and at all sampling rates the standard deviation values are lower for Si than for Ba. This phenomenon can be explained by the more uniform distribution of Si than that of Ba in the standards.

With *random stratified grid sampling* we try to approximate the regular network. Similarly to sampling along traverses, we located several parallel profiles vertically. The profiles were marked out on the base circle in equal lengths of arc distances. The centre of the base circle coincides with the axis of the cylinder which is taken as the origin. The sampling intervals along the profiles are the same.

With these measurements an opportunity presents itself for determining the areal distribution of Si and Ba elements. We carried out the meas-

urements along four profiles with 2 mm profile distance and 2 mm sampling interval. In the recorded emission spectra the amplitudes of the highest Ba (455.2 nm) and Si (288.2 nm) peaks were determined, and the amplitude maps (Figs. 8 and 9) constructed with the SURFER program.

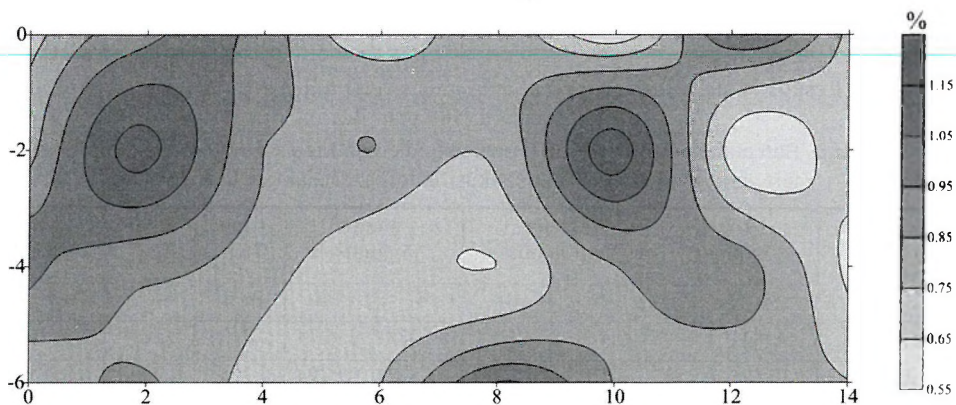


Fig. 8. Areal distribution of Ba amplitudes computed from LIPS measurements along parallel profiles on BaSO₄ standard marked Ba8

8. ábra. Ba8 jelű BaSO₄ etalonon szelvénymenti LIPS mérésekből számított Ba amplitúdó értékek területi eloszlása

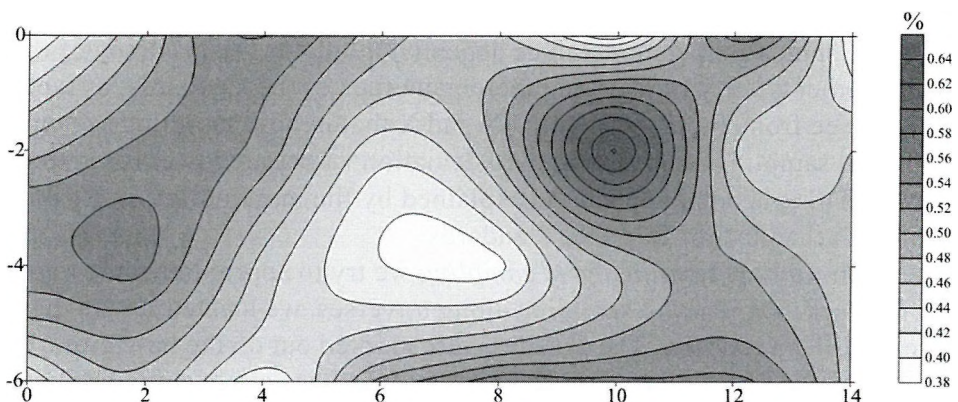


Fig. 9. Areal distribution of Si amplitudes computed from LIPS measurements along parallel profiles on BaSO₄ standard marked Ba8

9. ábra. Ba8 jelű BaSO₄ etalonon szelvénymenti LIPS mérésekből számított Si amplitúdó értékek területi eloszlása

4.2. Statistical investigation of Nd:YAG energy source and LIPS instrument stability

If we want to assess the accuracy of our measurements, we have to appraise every element of the procedure which provides at the end the quantity of interest. Accuracy includes not only the effects of random errors but also any bias due to uncorrected systematic error. In carrying out this assessment we used the tools of statistics [MIKHAIL, GRACIE 1981 or VINCZE 1975]. Before analysing our measurements, it is necessary to review the basic ideas and formulae of statistics.

In the following, as a matter of convention, random variables are represented by capital letters, and the numerical values they take on are represented by lower-case italic letters. The random event that X takes on the specific numerical value x is represented mathematically by the expression $X=x$, and the probability of this random event occurring, represented mathematically by $P[X=x]$, is given by the function $p(x)$, i.e.,

$$p(x) = P[X=x]$$

Here, X is a random variable and $p(x)$ is its *probability function*. The random variable and its probability function constitute what is known as a *probability model*. But this is not the only kind of function associated with a random variable. Another function with comparable importance is

$$F(x) = P[X \leq x] \quad \text{for all } x.$$

$F(x)$ is known as the *probability distribution function* of X , or simply the *distribution function*. It is to be interpreted as the probability of the event that the random variable takes on a value that is equal or less than x . The probability model can be given as well by the random variable and its distribution function. In either case, the model is known as a *probability distribution*.

The following properties apply to distribution functions:

$$P[a < X \leq b] = F(b) - F(a)$$

$$0 \leq F(x) \leq 1 \quad \text{for all } x$$

$$F(a) \leq F(b) \quad \text{for } a < b$$

$$F(-\infty) = 0$$

$$F(\infty) = 1$$

In the case of a continuous probability distribution, it is more convenient to use another function — the probability density function $f(x)$, which

is mathematically defined as the first derivative of the distribution function, i.e.,

$$f(x) = F'(x)$$

Keeping in mind the properties of $F(x)$, we can see that

$$P[a < X \leq b] = F(b) - F(a) = \int_a^b f(x) dx$$

which provides the means for evaluating the probability that the random variable X takes on a value between a and b . This also means that the probability of this event is represented by the area under the density function between a and b .

Now let us examine the case of normal distribution because it has widespread application in science and technology. The density function of the normal distribution is:

$$f(x) = \frac{1}{\sigma \sqrt{2\pi}} \exp\left\{-\frac{(x - \mu)^2}{2\sigma^2}\right\} \quad \text{for } -\infty < x < \infty$$

The parameters of the distribution, μ and σ are called the *mean* and the *standard deviation*, respectively.

The distribution function of the normal distribution is

$$F(x) = \int_{-\infty}^x f(u) du = \frac{1}{\sigma \sqrt{2\pi}} \int_{-\infty}^x \exp\left\{-\frac{(u - \mu)^2}{2\sigma^2}\right\} du.$$

It is necessary to change the variable of integration (to u , in this case), since x is one of the limits of integration.

A convenient way of evaluating probabilities associated with any normal distribution is introducing the variable

$$Z = \frac{X - \mu}{\sigma}$$

This transformation is called standardization, resulting in a simplified form of the density function:

$$f(z) = \frac{1}{\sqrt{2\pi}} \exp\left\{-\frac{z^2}{2}\right\} \quad \text{for } -\infty < z < \infty$$

Even though it is just as impossible to integrate $f(z)$ directly as it is $f(x)$ for the normal distribution there is but one $f(z)$ to integrate. The resulting function is

$$P[Z \leq z] = \Phi(z) = \frac{1}{\sqrt{2\pi}} \int_{-\infty}^z \exp\left\{-\frac{u^2}{2}\right\} du \quad \text{for } -\infty < z < \infty$$

As this integral is impossible to solve directly, it was evaluated by approximate means, and values of $\Phi(z)$ tabulated (see *Table XI* after VINCZE 1975).

z	$2\Phi(z)-1$
1	0.68269
1.5	0.86638
2	0.95450
2.5	0.98758
3	0.99730
3.5	0.99953
4	0.99994

Table XI. Values of the standard normal distribution function, i.e. probabilities that z lies within a symmetric interval around the expected value

XI. táblázat. A normális eloszlású változó várható értéke körüli szimmetrikus intervallumba esés valószínűség értékei

If X is a discretely distributed random variable, with possible values $x_1, x_2, x_3, \dots, x_n$, the probability function of X is given by $p(x_i), i=1, 2, \dots, n$. The weighted sum of all possible values, where the weights are the corresponding probabilities, is called the *expected value* of X , which is equal to the mean of X commonly represented by μ :

$$E[X] = \sum_{i=1}^n x_i p(x_i) = \mu$$

Replacing X by $(X-\mu)^2$, we obtain

$$E[(X - \mu)^2] = \sum (x_i - \mu)^2 p(x_i) = \sigma^2$$

This is called the *variance* of X , and is commonly denoted by σ^2 . The positive square root of the variance, denoted by σ , is called the *standard deviation*. The standard deviation is also a measure of the spread of the probability distribution.

For continuous probability distributions, the mean and variance are defined in terms of integrals instead of sums:

$$\sigma^2 = E[(X - \mu)^2] = \int_{-\infty}^{\infty} (x - \mu)^2 f(x) dx$$

For symmetrical distributions, such as the normal distribution, the mean is the central value about which the symmetry exists, and the parameters μ and σ found in the density function of the normal distribution have the meaning of expected value and standard deviation, respectively.

Now let us examine the instruments at our disposal. The most important question is whether the variance of measurements is a random variable, i.e. the variance has a normal distribution or not — called *statistical testing*— and if the answer is yes, we are looking for an interval in which the observed data occur with a specified probability (*confidence level*), called *interval estimation*.

To characterize our Nd:YAG laser source, the plot of Fig. 10/a serves best, which shows the 100-shot test of the producer (KIGRE Inc.) for the determination of average energy (19.4 mJ). By digitizing this plot, and using the above formulae, we calculated both the standardized density function and the distribution function of the 100-shot test of the laser source (Figs. 10/b and c). The mean was found: $\mu = 19.48$ mJ, and the standard deviation: $\sigma = 0.61$ mJ.

As these latter figures may reassure us that the energy distribution data of the laser source constitute a normal distribution, let us start with interval estimation, in other words we are looking for an (α_1, α_2) interval which contains the μ expected value with high probability:

$$P(\alpha_1 < \mu < \alpha_2) = 1 - \epsilon \quad (1)$$



KIGRE, INC.

100 Shot Test
K08760@ 1/3 Hz

a)

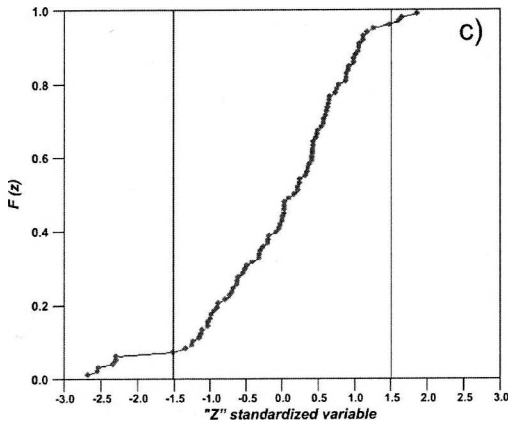
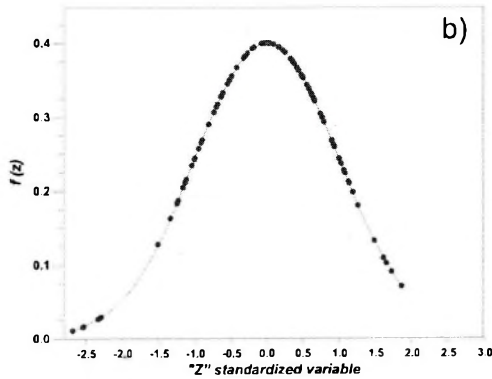
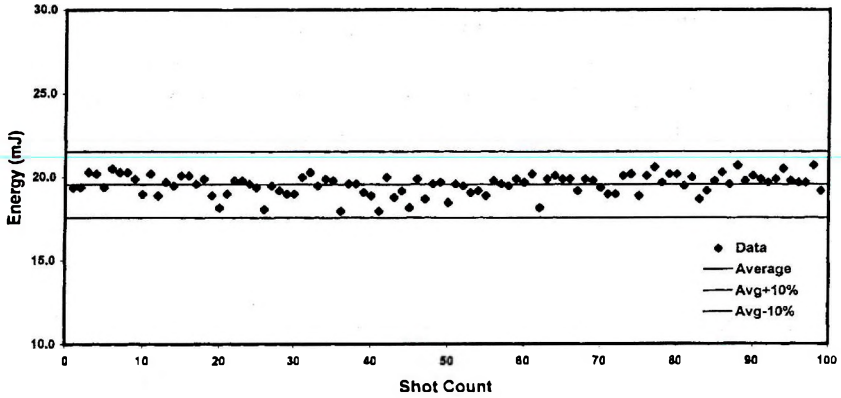


Fig. 10. Energy distribution of

Nd:YAG laser source

a) A 100-shot test by KIGRE

Inc.; b) Standardized density

function

c) Standardized distribution

function

10. ábra. Nd:YAG lézerforrás

energia eloszlása

a) A gyártó KIGRE Inc.

100-lövéses teszt-mérése;

b) Standardizált

sűrűség-függvény;

c) Standardizált

eloszlás-függvény

where ε is a small number and the values of α_1 and α_2 probability variables are determined by our measurements. If Eq. (1) holds, the (α_1, α_2) interval is called the confidence interval of $(1-\varepsilon)$ confidence level, regarding μ .

If a random sample of size n is drawn from a normally distributed population with mean μ and variance σ^2 , the sample mean \bar{X} has a normal distribution with mean μ and variance σ^2/n . Thus, the quantity

$$Z = \frac{\bar{X} - \mu}{\sigma / \sqrt{n}} \quad (2)$$

has a standard normal distribution with zero mean and unit variance, and it follows that

$$P \left[-z < \frac{\bar{X} - \mu}{\sigma / \sqrt{n}} < z \right] = 2\Phi(z) - 1 \quad (3)$$

where $\Phi(z)$ is the value of the standard normal distribution function, obtainable from Table XI.

Rearranging the inequality inside the brackets of Eq. (3), we get:

$$P \left[\bar{X} - \frac{z\sigma}{\sqrt{n}} < \mu < \bar{X} + \frac{z\sigma}{\sqrt{n}} \right] = 2\Phi(z) - 1 \quad (4)$$

which means: the probability that μ lies between $\bar{X} - (z\sigma / \sqrt{n})$ and $\bar{X} + (z\sigma / \sqrt{n})$ is $2\Phi(z)-1$. When a specific numerical value \bar{x} is provided for \bar{X} , the foregoing probability statement becomes a confidence statement. The values $\bar{x} - (z\sigma / \sqrt{n})$ and $\bar{x} + (z\sigma / \sqrt{n})$ are known as *confidence limits*, the interval between them is known as a *confidence interval*, and $2\Phi(z)-1$ is known as the degree of confidence, or *confidence level*, often stated as a percentage. The construction of a confidence interval for a particular distribution parameter, such as μ , is known as *interval estimation*.

It is often desirable to ascertain from a sample whether or not a population has a particular probability distribution. The usual course of action that is taken is to make a statement about the probability distribution of the population, and then test to see if the sample drawn from the population is consistent with the statement, called a statistical hypothesis. For every hy-

pothesis H_0 (null hypothesis) there is a complementary alternative H_1 (alternative hypothesis).

Under certain conditions we may expect the mean μ of a probability distribution to have a specific value μ_0 . Applying the above-described statistical test to the 100-shot test of the laser source, the null hypothesis to be tested is:

$$H_0 : M(X) = \mu_0 = 19.48$$

If H_0 holds, the probability variable z is of $N(0,1)$ normal distribution. Let us choose some confidence levels from Table XI, and calculate — with the help of Eq. (4) — those (α_1, α_2) intervals in which variable z of normal distribution occurs with a probability of $(1-\varepsilon)$. The results of this calculation are given in Table XII for the 100-shot test of our laser source.

n	μ_0 (mJ)	σ_0	$1 - \varepsilon$	z	$z\sigma/\sqrt{n}$	α_1	α_2
100	19.48	0.61	0.86638	1.5	0.0915	19.39	19.57
100	19.48	0.61	0.95450	2	0.1220	19.36	19.60
100	19.48	0.61	0.98758	2.5	0.1525	19.33	19.63
100	19.48	0.61	0.99730	3	0.1830	19.30	19.66
100	19.48	0.61	0.99953	3.5	0.2135	19.27	19.69

Table XII. Statistical evaluation of the 100-shot test (carried out by KIGRE Inc.) of Nd:YAG laser source

XII. táblázat. Nd:YAG lézerforrás 100 lövésés energia eloszlásának statisztikai feldolgozása a KIGRE Inc. mérései alapján

As can be seen from Figs. 10/b and c, accepting the null hypothesis was a correct decision because 90 % of the data occur within the $z=\pm 1.5$ zone, at a probability of $(1-\varepsilon)=0.86638$.

The mean, μ_0 , computed from the measurement data of Fig.10/a can be found within the confidence interval of

$$19.39 < \mu_0 < 19.57$$

at a probability of $(1-\varepsilon)=0.86638$. This confidence level equals a 4.7 % relative error, which means that the energy variation of our laser source causes a relative stability error of 4.7 % in our measurements.

This error is but one part of the total stability error caused by the whole measurement system. To calculate the total stability error, we carried out 50 laser shots in the same position at regular intervals on extra pure Al and

Cu standards and determined the peak-amplitudes of the $\lambda = 309.3$ nm spectrum line for Al and the $\lambda = 328$ nm for Cu. Similarly to the statistical computations shown above, we examined the standard deviation and confidence level of these peak amplitudes. The computations were carried out in two versions.

In the first version we grouped the data in a growing number of measurements ($n=5, 10, 15, \dots$), and computed the group means and their standard deviations (see *Table XIII*). The results of the respective statistical computations are shown in *Table XIV*.

Using the expected values and standard deviations of *Table XIV*, the respective null hypotheses are:

$$H_0 : M(X) = \mu_0 = 1.3067 \text{ for Al,}$$

$$H_0 : M(X) = \mu_0 = 0.9712 \text{ for Cu.}$$

We find that variable z is of $N(0,1)$ normal distribution as the μ_0 values fall within the

$$1.2235 < \mu_0 < 1.3899$$

$$0.9344 < \mu_0 < 1.0080$$

No. of shots n	Al metal standard		Cu metal standard	
	Mean μ_0	S. dev. σ_n	Mean μ_0	S. dev. σ_n
1-5	1.3513	0.1284	1.0071	0.0482
1-10	1.3790	0.1823	0.9891	0.0748
1-15	1.2854	0.2242	0.9945	0.0741
1-20	1.3030	0.2274	1.0005	0.0746
1-25	1.3435	0.2129	1.0102	0.0733
1-30	1.3462	0.2179	0.9945	0.0768
1-35	1.3410	0.2074	0.9867	0.0784
1-40	1.3267	0.2032	0.9751	0.0673
1-45	1.3190	0.1871	0.9733	0.0893
1-50	1.3067	0.1962	0.9712	0.0867

Table XIII. Results of LIPS measurements on extra-pure Al and Cu standards (first version)

XIII. táblázat. Nagy tisztaságú Al és Cu fém etalon mintákon elvégzett LIPS-mérések eredményei (első megadás)

Al metal standard							
n	μ_0	σ_0	$1 - \varepsilon$	z	$z\sigma_0/\sqrt{n}$	α_1	α_2
50	1.3067	0.1962	0.86638	1.5	0.0416	1.2651	1.3483
50	1.3067	0.1962	0.95450	2	0.0555	1.2512	1.3622
50	1.3067	0.1962	0.98758	2.5	0.0693	1.2374	1.3761
50	1.3067	0.1962	0.99730	3	0.0832	1.2235	1.3899
Cu metal standard							
n	μ_0	σ_0	$1 - \varepsilon$	z	$z\sigma_0/\sqrt{n}$	α_1	α_2
50	0.9712	0.0867	0.86638	1.5	0.0184	0.9528	0.9896
50	0.9712	0.0867	0.95450	2	0.0245	0.9467	0.9957
50	0.9712	0.0867	0.98758	2.5	0.0307	0.9405	1.0019
50	0.9712	0.0867	0.99730	3	0.0368	0.9344	1.0080

Table XIV. Statistical evaluation of LIPS measurements on extra-pure Al and Cu standards (first version)

XIV. táblázat. Nagy tisztaságú Al és Cu fém etalon mintákon elvégzett LIPS-mérések eredményeinek statisztikai feldolgozása (első megoldás)

confidence intervals at a confidence level of $(1-\varepsilon)=0.99730$. Thus, accepting the null hypothesis was a correct decision.

In the second version we made groups of ($n=5$) data and computed the group means and their standard deviations (see Table XV). The results of the respective statistical computations are shown in Table XVI.

In this case the same null hypotheses are to be tested:

$$H_0 : M(X) = \mu_0 = 1.3067 \quad \text{for Al,}$$

$$H_0 : M(X) = \mu_0 = 0.9712 \quad \text{for Cu.}$$

If H_0 holds, the probability variable z representing the variance is of $N(0,1)$ normal distribution. But, contrary to the first version, we find that some of the measurement data are beyond the confidence interval of

$$1.2355 < \mu_0 < 1.3779$$

$$0.9418 < \mu_0 < 1.006$$

Thus, if the null hypothesis was accepted when H_0 is false, the outcome is known as a *Type II error*, which is characterized by a δ error, by which the expected value of $M(X)$ will be within the $(\mu_0 - \delta, \mu_0 + \delta)$ interval. We take this δ error to be equivalent with the total stability error of the method characterizing the observed amplitude variations.

No. of shots <i>n</i>	Al metal standard		Cu metal standard	
	Mean μ_0	S. dev. σ_0	Mean μ_0	S. dev. σ_0
	1-5	1.3513	0.1284	1.0140
6-10	1.2845	0.2168	0.9643	0.0906
11-15	1.2205	0.2806	1.0053	0.0715
16-20	1.3555	0.2289	1.0183	0.0732
21-25	1.5059	0.1550	1.0491	0.0525
26-30	1.3596	0.1605	0.9158	0.0324
30-35	1.3096	0.1258	0.9398	0.0715
36-40	1.2265	0.1333	0.8940	0.1024
41-45	1.2572	0.1706	0.9590	0.1028
46-50	1.1956	0.0741	0.9597	0.0544
Mean	1.3067	0.1680	0.9712	0.0693

Table XV. Results of LIPS measurements on extra-pure Al and Cu standards (second version)

XV. táblázat. Nagy tisztaságú Al és Cu fém etalon mintákon elvégzett LIPS-mérések eredményei (második megoldás)

Al metal standard							
<i>n</i>	μ_0	σ_0	$1 - \varepsilon$	<i>z</i>	$z\sigma_0/\sqrt{n}$	α_1	α_2
50	1.3067	0.1680	0.86638	1.5	0.0356	1.2711	1.3423
50	1.3067	0.1680	0.95450	2	0.0475	1.2592	1.3542
50	1.3067	0.1680	0.98758	2.5	0.0594	1.2473	1.3661
50	1.3067	0.1680	0.99730	3	0.0712	1.2355	1.3779
Cu metal standard							
<i>n</i>	μ_0	σ_0	$1 - \varepsilon$	<i>z</i>	$z\sigma_0/\sqrt{n}$	α_1	α_2
50	0.9712	0.0693	0.86638	1.5	0.0147	0.9565	0.9859
50	0.9712	0.0693	0.95450	2	0.0196	0.9516	0.9908
50	0.9712	0.0693	0.98758	2.5	0.0245	0.9467	0.9957
50	0.9712	0.0693	0.99730	3	0.0294	0.9418	1.006

Table XVI. Statistical evaluation of LIPS measurements on extra-pure Al and Cu standards (second version)

XVI. táblázat. Nagy tisztaságú Al és Cu fém etalon mintákon elvégzett LIPS-mérések eredményeinek statisztikai feldolgozása (második megoldás)

Let us consider the different types of errors involved. Above we determined the stability error of the laser source Nd:YAG of $\mu_0 = 19.48$ mJ average energy as $S_e = \pm 4.7\%$.

The stability of the measuring system is also influenced by the relative stability error of reliability S_k , which is a function of the average amplitudes. As deduced from stability measurements on Al and Cu standards, their values are $\pm 5.449\%$ and $\pm 3.027\%$, respectively. Total stability error can be calculated — according to error propagation — as

$$\delta = \sqrt{S_e^2 + S_k^2}$$

Substituting the above values, we get the total stability error δ

for Al: $\pm 7.2\%$,

for Cu: $\pm 5.6\%$.

Supposing that the total stability error is independent of the object of measurements, in the following we use the average of these figures ($\delta_{av} = 6.4\%$) for our further calculations.

4.3. *Statistical analysis of elemental concentration distributions on a crystalline drill core*

When applying LIPS measurements for determining mineral composition or mineral distribution, the accuracy of results has to be determined as well. To this end, in addition to the total stability error (δ) the calibration error (k) of the element in question has to be known. In the case of a given concentration value, the calibration error originates from the deviation between input data and the regression curve. The relative error of concentration (τ) will be the square sum of the relative total stability error and the relative calibration error:

$$\tau = \sqrt{\delta^2 + k^2}$$

For determining this concentration error, a practical example is presented. A drill core of Üveghuta–3 borehole was used for stability tests. At point 30 of profile No. 5, 30 laser shots were executed in 2-minute intervals, and resultant error τ was determined for matrix elements Al, Ca, Fe, K, Mg, Si and Ti. The percentage accuracy of concentration Δc can be calculated from τ and average values μ_0 by the relation:

$$\Delta c = \mu_0 \tau / 100.$$

The percentile results of concentration means (μ_0), average of relative total stability error (δ_{av}), relative calibration error (k) and resultant relative error (τ) as well as the accuracy of concentration (Δc) computed from the latter are all presented in *Table XVII*. It has to be mentioned that the standard deviation of regression depends on concentration, therefore the deviation curve of the target function is indispensable for the calculation of τ .

	Al %	Ca %	Fe %	K %	Mg %	Si %	Ti %
μ_0	17.8	1.84	3.02	4.23	1.68	70.71	0.72
δ_{av}	6.4	6.4	6.4	6.4	6.4	6.4	6.4
k	-4	5	0	0	1	-0.5	-5
τ	7.54	8.12	6.4	6.4	6.47	6.4	8.12
Δc	1.35	0.15	0.19	0.27	0.11	3.20	0.06

Table XVII. Errors calculated from statistical evaluation of stability measurements on a core from borehole Üveghuta-3

XVII. táblázat. Az Üveghuta-3 mélyfúrásból származó fúrómagon elvégzett stabilitás mérések statisztikai feldolgozásának eredményeiből számított hiba értékek

We have also studied the distribution of concentration values of Al, in steps of its relative concentration error ($\Delta c = \pm 1.35$), starting from the average concentration ($\mu_0 = 17.8$). The results are presented in *Table XVIII*. It can be

Concentration range %	Frequency
11.05-12.39	0
12.40-13.74	1
13.75-15.09	4
15.10-16.44	3
16.45-19.14	13
19.15-20.49	4
20.50-21.84	5
21.85-23.19	0

Table XVIII. Frequencies of occurrence for Al calculated from statistical evaluation of stability measurements on a core from borehole Üveghuta-3

XVIII. táblázat. Az Üveghuta-3 mélyfúrásból származó fúrómagon elvégzett stabilitás mérések statisztikai feldolgozásból számított gyakorisági értékek Al-ra

stated that the occurrence frequencies follow a normal distribution with good approximation in spite of the outstanding value in the 20.5–21.84 interval. This can be attributed to the mineral inhomogeneity of the sample, as the consecutive laser shots deepen the crater by several microns.

5. Detailed analysis of a drill core of Üveghuta–3 borehole

To test LIPS measurements by comparing their results with geological and chemical analysis data, a test area had to be chosen. The best available was that of Üveghuta, where a radioactive waste disposal project is in progress. The granite body, partly covered by loess, was explored in a near-regular grid by drill holes, all penetrating the granite by continuous coring. In the analysis of cores all the most up-to-date equipment of MÁFI was used.

5.1. Areal distribution of element oxide concentrations

LIPS measurements are suitable for the study of mineral composition over the cylindrical superficies of a drill core or on the kerf of a drill core cut in half. We chose the latter, and carried out our measurements over a random stratified grid. Laboratory analysis by ICP AES as well as theoretical model calculations provide the percentage volume and weight of element oxides, therefore in the following we also use the matrix element oxide concentration values.

The set of points marked out on the set of parallel profiles can be regarded as an irregular network. The sampling rate on each profile was the same. The smooth cut surface of an area of 55×20 mm made it possible to locate seven parallel profiles with 2 mm distance between them. Along the profiles the sampling interval was 5 mm.

By interpreting the emission spectra of LIPS measurements we could carry out the computations for element oxides. With the help of calibration functions, the concentration values of matrix element oxides were calculated at each measurement point. These data were plotted as isoline maps and presented in *Figures 11, 12, 13, 14, 15 16 and 17.*

For petrological interpretation it was found more convenient to map the ratio of certain element oxides, as these can be connected to some min-

erals. As examples the $\text{SiO}_2/\text{Al}_2\text{O}_3$, the SiO_2/CaO and the SiO_2/MgO ratios have been mapped and presented in *Figures 18, 19 and 20*.

The crystalline rocks of Üveghuta show extreme variation: white and pink, microcline-containing porphyroblastic granite, amphibole-rich rocks (restite), microgranite and pegmatite. Microcline usually contains biotite, plagioclase and quartz inclusions. One can find their detailed description in [BUDA and PUSKÁS 1997].

To interpret the isoline maps of element oxides and their ratios, we have to know the percentage element oxide concentration of the rock-forming minerals or their element oxide ratios. Based on our investigation and the published data on granite-forming minerals (*Table XIX*), the weight

Mineral	Formula
Microcline	$\text{K} [\text{Al Si}_3\text{O}_8]$
Albite	$\text{Na} [\text{Al Si}_3\text{O}_8]$
Anortite	$\text{Ca} [\text{Al}_2\text{Si}_2\text{O}_8]$
Oligoclase	10–30 % Anortite + 90–70 % Albite
Andesine	30–50 % Anortite + 70–50 % Albite
Labradorite	50–70 % Anortite + 50–30 % Albite
Bytownite	70–90 % Anortite + 30–10 % Albite
Quartz	SiO_2
Biotite	$\text{K}(\text{Mg}, \text{Fe})_3 [(\text{OH}, \text{F})_2 (\text{Al}, \text{Fe})\text{Si}_5\text{O}_{10}]$
Amphibole	$\text{Ca}_2\text{Na} (\text{Mg}, \text{Fe}, \text{Al}, \text{Ti})_3 \text{Si}_8\text{O}_{22} (\text{O}, \text{OH})_2$

Table XIX. Formulae of main minerals forming a common granite
XIX. táblázat. Az átlagos gránitot alkotó főbb ásványtípusok képletei

percentages of element oxides in the main minerals forming common granites are those given in *Tables XX/a and XX/b*, while those of element oxide ratios in *Table XXI*. Data of the first four rows of *Table XX/b* are taken from DEER et al. [1963]; the next three rows were computed by one of the present authors using theoretical stoichiometric formulae, and supposing the

Mineral	Al_2O_3 %	CaO %	FeO %	K_2O %	MgO %	Na_2O %	SiO_2 %	TiO_2 %
Microcline	18.35	-	-	16.90	-	-	64.75	-
Quartz	-	-	-	-	-	-	100.00	-
Biotite	10.07	-	25.72	9.28	11.94	-	35.55	-
Amphibole	5.02	7.17	4.27	-	3.87	4.86	61.42	7.68

Table XX/a. Element oxide weight percentages of the main minerals forming a common granite except plagioclase

XX/a. táblázat. Az átlagos gránitot alkotó főbb ásványtípusok elemoxid súlyszázalékos összetétele a plagioklászok kivételével

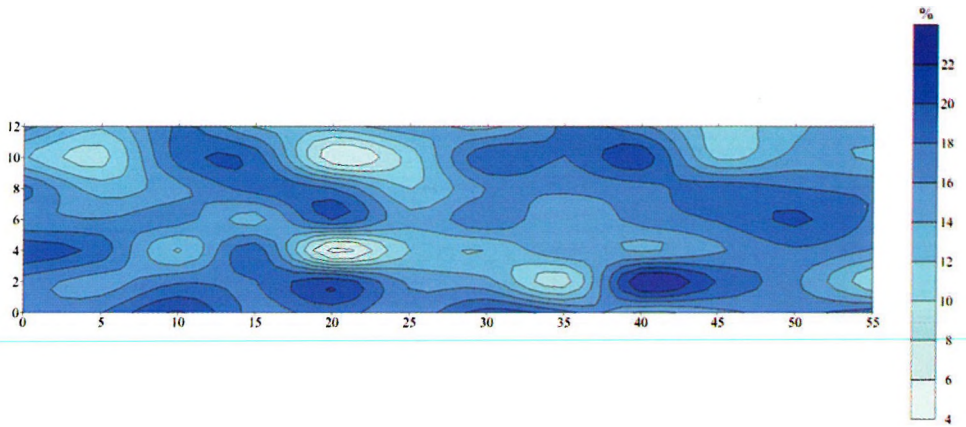


Fig. 11. Areal distribution of Al_2O_3 concentration as a result of LIPS measurements along parallel profiles on a drill core cut in half from Üveghuta-3 borehole

11. ábra. Üveghuta-3 fúrás félbevágott fúrómag mintaanyagán szelvénymenti LIPS-mérésekből számított Al_2O_3 koncentráció értékek területi eloszlása

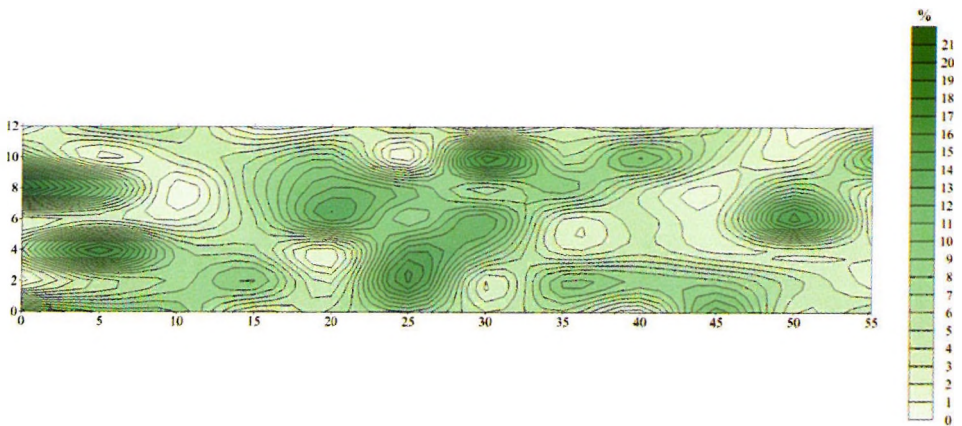


Fig. 12. Areal distribution of CaO concentration as a result of LIPS measurements along parallel profiles on a drill core cut in half from Üveghuta-3 borehole

12. ábra. Üveghuta-3 fúrás félbevágott fúrómag mintaanyagán szelvénymenti LIPS-mérésekből számított CaO koncentráció értékek területi eloszlása

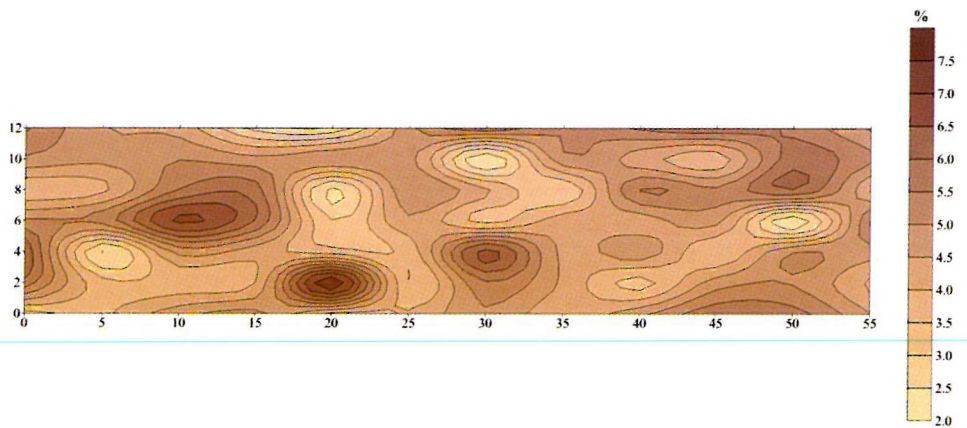


Fig. 13. Areal distribution of FeO concentration as a result of LIPS measurements along parallel profiles on a drill core cut in half from Üveghuta-3 borehole

13. ábra. Üveghuta-3 fúrás félbevágott fúrómag mintaanyagán szelvény menti LIPS-mérésekből számított FeO koncentráció értékek területi eloszlása

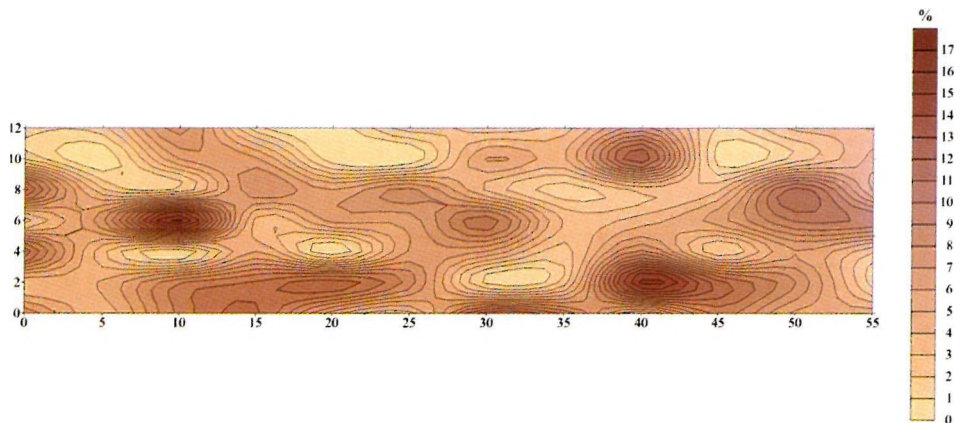


Fig. 14. Areal distribution of K_2O concentration as a result of LIPS measurements along parallel profiles on a drill core cut in half from Üveghuta-3 borehole

14. ábra. Üveghuta-3 fúrás félbevágott fúrómag mintaanyagán szelvény menti LIPS-mérésekből számított K_2O koncentráció értékek területi eloszlása

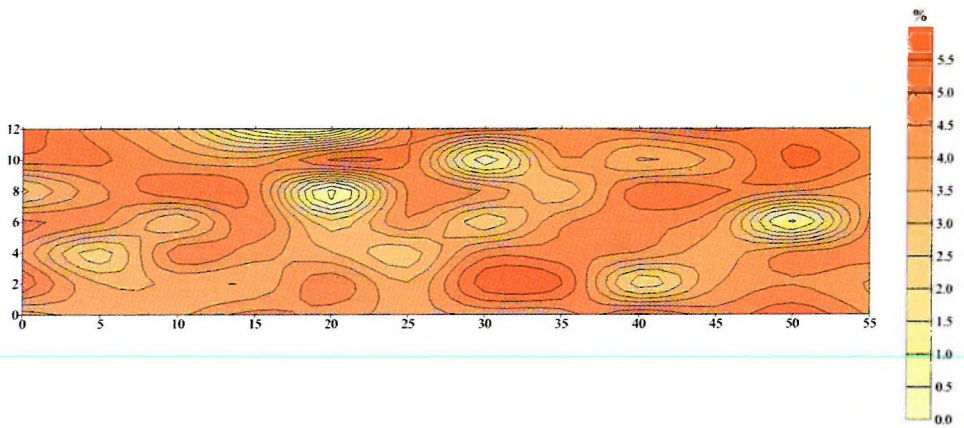


Fig. 15. Areal distribution of MgO concentration as a result of LIPS measurements along parallel profiles on a drill core cut in half from Üveghuta-3 borehole

15. ábra. Üveghuta-3 fúrás félbevágott fúrómag mintaanyagán szelvény menti LIPS-mérésekből számított MgO koncentráció értékek területi eloszlása

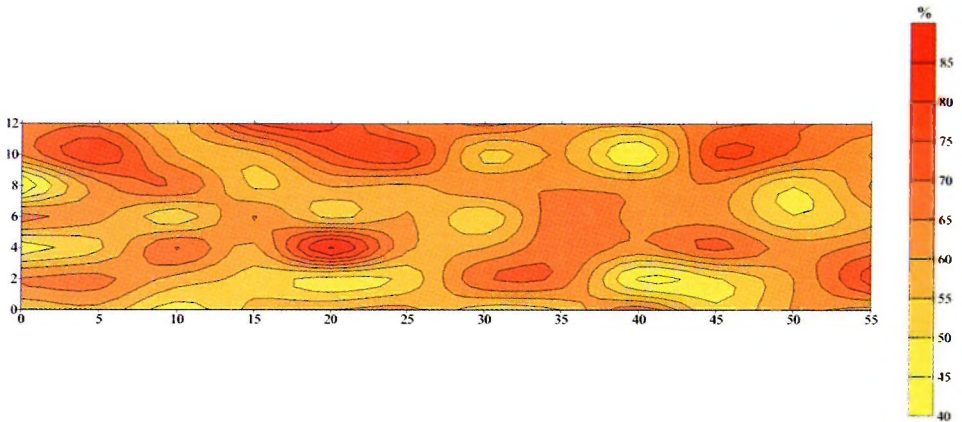


Fig. 16. Areal distribution of SiO₂ concentration as a result of LIPS measurements along parallel profiles on a drill core cut in half from Üveghuta-3 borehole

16. ábra. Üveghuta-3 fúrás félbevágott fúrómag mintaanyagán szelvény menti LIPS-mérésekből számított SiO₂ koncentráció értékek területi eloszlása

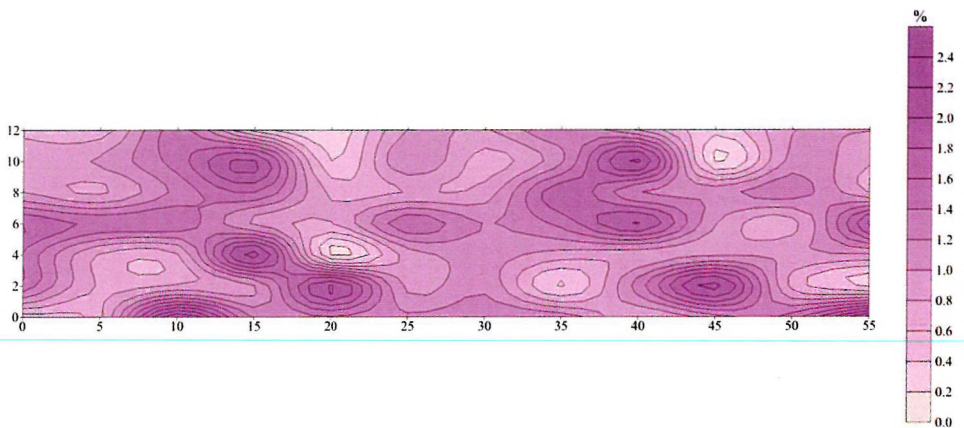


Fig. 17. Areal distribution of TiO_2 concentration as a result of LIPS measurements along parallel profiles on a drill core cut in half from Üveghuta-3 borehole

17. ábra. Üveghuta-3 fúrás félbevágott fúrómag mintaanyagán szelvény menti LIPS-mérésekből számított TiO_2 koncentráció értékek területi eloszlása

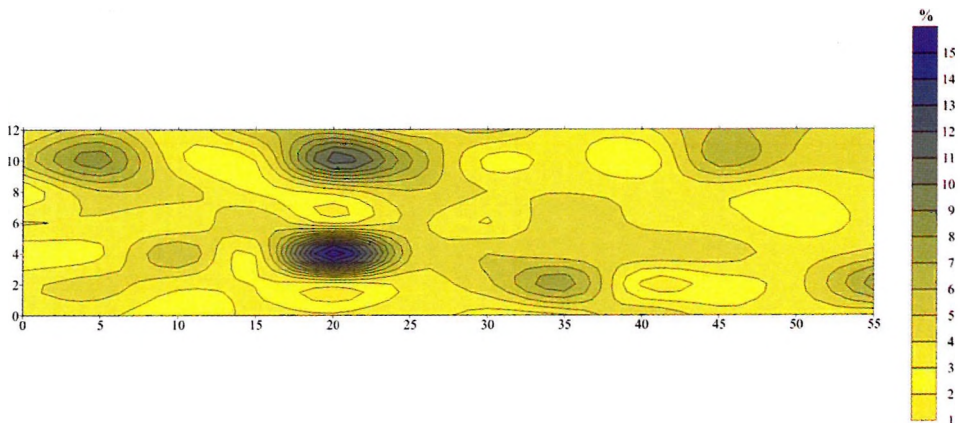


Fig. 18. Areal distribution of $\text{SiO}_2/\text{Al}_2\text{O}_3$ concentration ratio as a result of LIPS measurements along parallel profiles on a drill core cut in half from Üveghuta-3 borehole

18. ábra. Üveghuta-3 fúrás félbevágott fúrómag mintaanyagán szelvény menti LIPS-mérésekből számított $\text{SiO}_2/\text{Al}_2\text{O}_3$ koncentráció arány értékek területi eloszlása

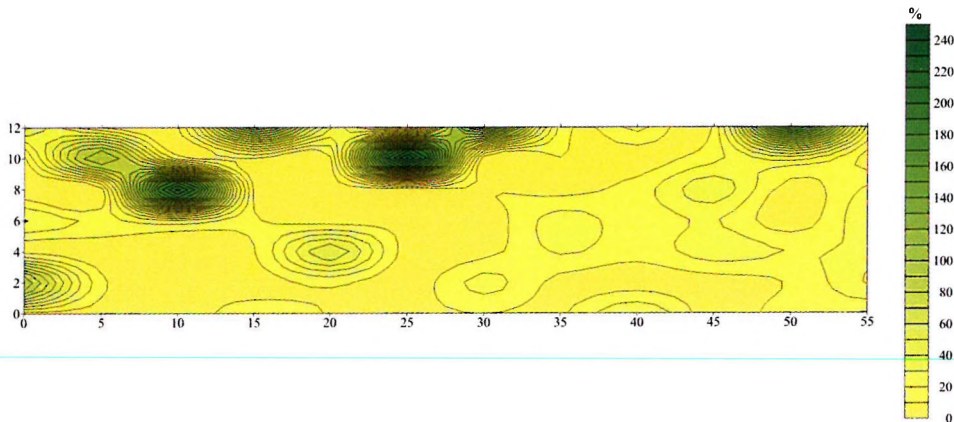


Fig. 19. Areal distribution of SiO_2/CaO concentration ratio as a result of LIPS measurements along parallel profiles on a drill core cut in half from Üveghuta-3 borehole

19. ábra. Üveghuta-3 fúrás félbevágott fúrómag mintaanyagán szelvény menti LIPS-mérésekből számított SiO_2/CaO koncentráció arány értékek területi eloszlása

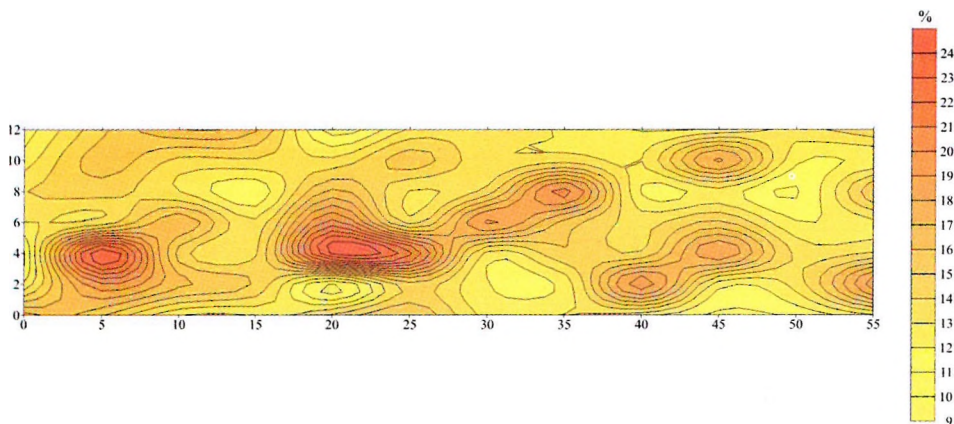


Fig. 20. Areal distribution of SiO_2/MgO concentration ratio as a result of LIPS measurements along parallel profiles on a drill core cut in half from Üveghuta-3 borehole

20. ábra. Üveghuta-3 fúrás félbevágott fúrómag mintaanyagán szelvény menti LIPS-mérésekből számított SiO_2/MgO koncentráció arány értékek területi eloszlása

gradual decrease of potassium-feldspar as inclusions in the Ab–An series. In the theoretical plagioclase series the composition of the minerals is expressed by the anortite content. The computed oxide weight percentages refer to the centre of the specified interval. The orthoclase content is assumed to change linearly from 5% to 0% in the Ab–An series.

From Table XXI it can be seen that in the case of large (larger than the laser ablation crater) homogeneous crystals it is possible to identify (or exclude) some of the minerals by examining one ratio, while if all three ratios are at our disposal, all main minerals can be identified. For crystals smaller than the laser ablation crater, the method has to be calibrated to mineral assemblages.

In our example, the yellow, yellow-greenish low values (1–5) of $\text{SiO}_2/\text{Al}_2\text{O}_3$ ratio in Fig. 17, suggest the presence of plagioclases (oligoclase, andesine) and microcline, while the dark green, blue high values (5–15) mark mafic minerals, first of all amphibole. The presence of amphibole is also supported by the orange-coloured high values (13–24) of the SiO_2/MgO ratio in Fig. 19.

5.2. Comparison of LIPS provided element oxide concentrations and laboratory data

The above-described measurements on the Üvegkuta crystalline sample were used for further statistical analysis in order to improve their reliability. For all seven profiles — with twelve points on each — we have calculated the element oxide concentration averages, and their averages for the whole area. The results are presented in *Table XXII*, together with their standard deviation values. We can see that except FeO and MgO, in the concentration values of all oxides there are larger dispersions than the limits given by their standard deviations. This phenomenon can easily be explained by the mineral inhomogeneity of the crystalline rock sample.

We have also tested the distribution of Al_2O_3 concentration values, calculated at the 84 measurement points in steps of 2% (double its standard deviation). The results are presented in *Table XXIII*. It can be stated that the occurrence frequencies follow a normal distribution with good approximation. From the 84 data 53, i.e. 63.1%, can be found within the limits of its standard deviation.

For comparing LIPS data with those of laboratory analysis, the analysis results of samples of 12 boreholes for the main element oxides are pre-

Mineral (An %)	Al₂O₃ %	CaO %	K₂O %	Na₂O %	SiO₂ %
Albite (0-10)					
No of samples	14	14	14	14	14
Sum	283.62	9.57	7.57	151.56	937.42
Mean	20.26	0.68	0.54	10.83	66.96
Standard deviation	0.75	0.51	0.57	0.72	0.94
Minimum	18.97	0.03	0.03	9.53	65.62
Maximum	21.72	1.54	2.14	11.72	68.71
Computed mean	20.30	0.96	0.803	10.406	67.43
Oligoclase (10-30)					
No of samples	14	14	14	14	14
Sum	319.62	53.82	9.16	124.96	883.68
Mean	22.83	3.84	0.65	8.93	63.12
Standard deviation	1.01	1.04	0.44	0.80	1.45
Minimum	20.72	2.18	0.05	7.38	60.85
Maximum	24.44	5.81	1.49	10.15	64.92
Computed mean	22.78	3.87	0.676	8.832	63.84
Andesine (30-50)					
No of samples	14	14	14	14	14
Sum	357.4	108.2	8.69	93.05	822.58
Mean	25.53	7.73	0.62	6.65	58.76
Standard deviation	1.28	1.04	0.32	0.70	1.71
Minimum	22.04	6.31	0.12	5.48	56.1
Maximum	27.66	9.7	1.1	8.12	62.94
Computed mean	26.16	7.81	0.507	6.69	58.82
Labradorite (50-70)					
No of samples	14	14	14	14	14
Sum	408.63	164	5.59	62.63	750.41
Mean	29.19	11.71	0.40	4.47	53.60
Standard deviation	0.99	0.96	0.26	0.65	1.28
Minimum	27.14	10.35	0.13	3.62	51.94
Maximum	30.22	13	1.02	5.57	56.18
Computed mean	29.60	11.84	0.338	4.51	53.71
Bytownite (70-90)					
No of samples	15	15	14	15	15
Sum	490.1	236.7	1.94	35.51	723.31
Mean	32.67	15.78	0.14	2.37	48.22
Standard deviation	1.08	1.31	7.35E-2	0.71	1.83
Minimum	30.99	13.83	0.03	1.18	45.16
Maximum	34.36	17.92	0.29	3.36	51.09
Computed mean	33.12	15.95	0.17	2.277	48.48
Anortite (90-100)					
No of samples	7	7	6	7	7
Sum	247.93	130.64	0.72	4.16	309.9
Mean	35.42	18.66	0.12	0.59	44.27
Standard deviation	0.70	0.70	0.15	0.296	0.829
Minimum	34.31	17.41	0	0.22	43.54
Maximum	36.18	19.53	0.42	0.98	45.88
Computed mean	35.80	19.08	0.042	0.573	44.50

Table XX/b. Element oxide weight percentages of main plagioclases forming a common granite (composition of plagioclases after DEER, HOWIE and ZUSSMANN [1963])



XX/b. táblázat. Az átlagos gránitot alkotó főbb plagioklászok elemoxid súlyszázalékos összetétele (a plagioklászok összetétele DEER, HOWIE és ZUSSMANN [1963] nyomán)

Mineral	SiO ₂ /Al ₂ O ₃	SiO ₂ /CaO	SiO ₂ /MgO
Microcline	3.53	-	-
Albite	3.32	67.00	-
Oligoclase	2.78	15.86	
Andesine	2.22	7.28	
Labradorite	1.79	4.42	
Bytownite	1.45	2.99	
Anortite	1.24	2.32	-
Quartz	-	-	-
Biotite	3.53	-	1.19
Amphibole	12.23	8.57	15.87

Table XXI. Element oxide ratios of main minerals forming a common granite
XXI. táblázat. Az átlagos gránitot alkotó főbb ásványtípusok elemoxid arányai

	Al ₂ O ₃ %	CaO %	FeO %	K ₂ O %	MgO %	SiO ₂ %	TiO ₂ %
Profile1	17.85	7.55	4.60	7.36	4.34	56.95	1.36
Profile2	16.60	6.77	4.62	7.41	4.19	59.27	1.12
Profile3	14.95	6.69	4.53	4.53	4.08	64.20	1.02
Profile4	16.82	6.31	4.58	7.48	3.85	59.58	1.39
Profile5	16.70	8.03	4.44	5.71	4.09	59.87	1.11
Profile6	14.62	6.53	4.53	3.98	4.44	64.80	1.10
Profile7	14.84	3.12	4.74	3.50	4.22	68.71	0.88
Mean	16.05	6.43	4.58	5.71	4.17	61.91	1.14
Δc	±1.15	±0.40	±0.40	±0.25	±0.30	±2.70	±0.08

Table XXII. Element oxide average concentrations according to LIPS measurements along a profile on a core cut in half from borehole Üveghuta-3

XXII. táblázat. Az egyes elemoxidok átlag koncentráció értékeinek eloszlása az Üveghuta-3 fúrásból származó félbevágott fúrómagon elvégzett szelvény menti LIPS-mérések alapján

Concentration range (%)	Frequency
3–4.99	0
5–6.99	2
7–8.99	0
9–10.99	4
11–12.99	8
13–14.99	13
15–16.99	20
17–18.99	22
19–20.99	10
21–22.99	4
23–24.99	1

Table XXIII. Frequencies of occurrence for Al_2O_3 calculated from statistical evaluation of LIPS measurements along a profile on a core cut in half from borehole Üveghuta–3

XXIII. táblázat. Üveghuta–3 fúrás félbevágott fúrómag mintaanyagán elvégzett szelvénymenti LIPS-mérések statisztikai feldolgozásából számított gyakoriság értékek

sented in Table XXIV (thanks to Gy. Maros). In Table XXV their mean values and those of LIPS measurements are compared. As in Table XXIV, FeO and Fe_2O_3 oxides appear in different rows; we have computed the Fe_2O_3 percentage concentration into FeO by the relation:

$$\text{FeO} (\%) = 0.56 \text{Fe}_2\text{O}_3 (\%).$$

When considering the relative deviations between the two data sets it should be borne in mind that they differ significantly: the 84 LIPS data originate from one drill core whereas the laboratory means are from 12 drill cores of 3 boreholes. Within the 12 drill cores, three types of granite were found, the greatest difference between the different types was in the SiO_2 and CaO content: in type I the SiO_2 varies between 48.8 and 54.4% (mean: 51.6%); in type II: between 57.00 and 60.8% (mean: 58.9%); the only representative of type III shows 70.10%. The relative deviation between types I and III is 26.4% much higher than the relative deviation between laboratory and LIPS means in Table XXV. As the main difference between granites is their acidic or mafic character, it is the SiO_2 content which is the dominant factor. Although the drill core used for LIPS experiments was not included in the laboratory program, based on its SiO_2 content it should be regarded as type II granite. In this case the 4.86% deviation between the laboratory mean for type II granite and the LIPS result is acceptable.

Sample	2/287	2/305	2/84	22/114	22/308	22/364	22/400	22/490	23/113	23/162	23/212	23/235	Mean
SiO ₂	53.90	59.80	57.00	60.80	70.10	53.60	51.50	54.40	53.60	53.50	49.70	48.80	55.56
TiO ₂	1.02	0.79	0.83	0.79	0.76	1.11	1.15	1.17	1.16	1.19	1.23	1.27	1.04
Al ₂ O ₃	15.30	15.30	15.30	16.90	13.80	16.90	16.30	16.00	15.90	15.10	18.00	17.80	16.05
Fe ₂ O ₃	0.86	0.96	2.11	0.61	0.82	1.29	1.36	4.49	1.51	1.07	2.17	1.27	1.54
FeO	4.45	3.85	2.31	3.03	2.78	4.21	4.77	1.27	4.58	4.66	4.88	5.89	3.89
MnO	0.12	0.09	0.08	0.07	0.02	0.09	0.10	0.09	0.10	0.09	0.11	0.12	0.09
MgO	4.64	3.58	3.16	3.74	2.16	5.33	6.54	5.28	6.01	5.92	5.26	5.77	4.78
CaO	6.54	4.35	4.48	3.29	0.65	4.60	5.53	5.51	4.93	5.39	6.87	7.41	4.96
Na ₂ O	2.51	2.45	2.03	2.55	3.67	2.53	3.13	3.27	2.79	2.00	2.68	2.59	2.68
K ₂ O	6.07	6.24	7.07	6.19	2.59	6.57	4.29	5.24	6.15	6.84	5.15	5.02	5.62
P ₂ O ₅	0.66	0.36	0.34	0.30	0.25	0.60	0.73	0.72	0.85	0.65	0.93	0.83	0.60
H ₂ O _p	1.97	1.13	2.75	0.78	2.02	2.36	2.60	1.46	1.74	2.64	2.02	2.09	1.96
H ₂ O _m	0.09	0.04	0.18	0.04	0.07	0.03	0.06	0.03	0.04	0.09	0.16	0.04	0.07
CO ₂	1.40	0.69	1.96	0.00	0.17	0.33	1.44	0.47	0.25	0.46	0.23	0.51	0.66
Total	99.53	99.64	99.60	99.08	99.87	99.55	99.51	99.40	99.61	99.60	99.38	99.41	99.51

Table XXII. Results of laboratory analyses of the cores of the Üveghuta exploration area (provided by Gy. Maros)
 XXIV. táblázat. Az üveghutai területen mélyített fúrásokból származó fűrőmag mintaanyagokon végzett laboratóriumi vizsgálatok
 eredményei (Maros Gy. adatai)

	Al ₂ O ₃ %	CaO %	FeO %	K ₂ O %	MgO %	SiO ₂ %	TiO ₂ %
LIPS Mean	16.05	6.43	4.58	5.71	4.17	61.91	1.14
Lab. Mean	16.05	4.96	4.74	5.62	4.78	55.56	1.04
Deviation	0.00	1.47	-0.16	0.09	-0.61	6.35	0.1
Rel. deviation	0.00	29.64	3.37	1.60	12.76	11.43	9.61

Table XXV. Comparison of average element oxide concentrations resulting from LIPS measurements along profiles and laboratory analyses

XXV. táblázat. Az egyes elemoxidok átlag koncentráció értékei szelvény menti LIPS mérések és laboratóriumi mérések alapján

The CaO concentration shows the highest deviation between laboratory and LIPS means. If we group the data again according to the three granite types, we get the following figures: type I: 5.85%; type II: 4.04%; type III: 0.65%. In other words, with growing SiO₂ content the CaO concentration decreases. As plagioclases and amphiboles are the two CaO-containing mineral groups, the reverse correlation between SiO₂ and CaO concentrations fits into the scheme. The cause of the high deviation in CaO concentration data may also be caused by the fact that amphibole often occurs as inclusions with a crystal size similar to that of the laser crater.

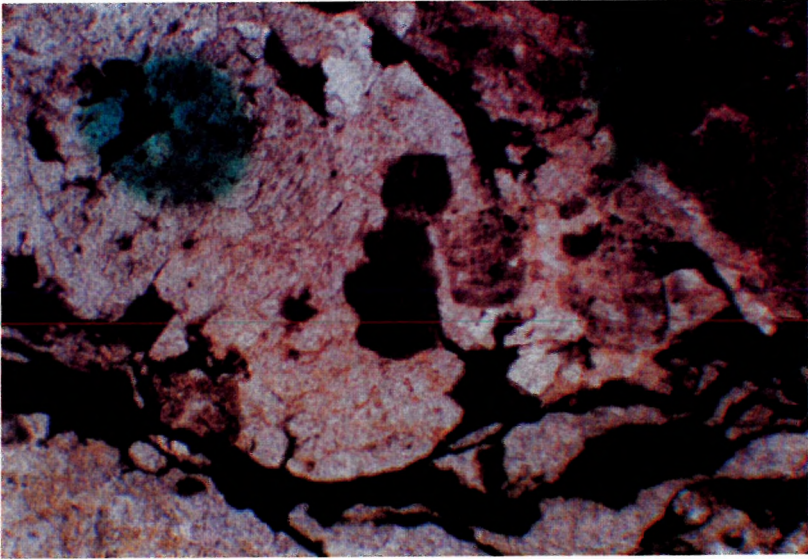
The zero deviation in Al₂O₃ concentration — as an element oxide to be found in all granite-forming main minerals — proves the high probability of hits of the laser shots in spite of the inhomogeneities of the rocks. Low deviations can be found in the case of K₂O and FeO, both mainly occurring in biotite, the former also in microcline. Besides the good agreement it is worth mentioning that these data can help in identifying these minerals.

The fair agreement in TiO₂ concentration data conveys the possibility of its occurrence not only in titanite, but as inclusions in other minerals (interpretation of Z. Balla).

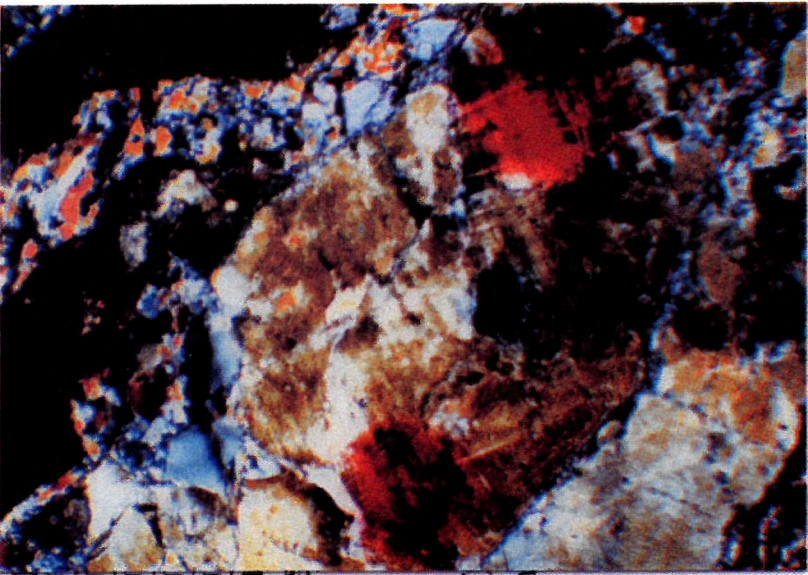
The above-presented comparison between LIPS and laboratory results is just the first step in determining the accuracy of LIPS measurements. It is planned that further studies will include comparison with other methods as well.

5.3. LIPS measurements on thin sections prepared from a drill core of borehole Üveghuta-3

The mineral content of drill cores cannot be determined with the necessary accuracy because of — among other factors — unpositioned and



a)



b)

Fig. 21. Locating the laser shot on a thin slide from a core of Üveghuta–3 borehole
a) green spot: location marked out for a laser shot. *b)* the black hole between red spots is
the location of a laser crater

21. ábra. Mintavételi hely kijelölése a lézer-lövés számára az Üveghuta–3 fúrás
mintaanyagából készült vékonycsiszolaton
a) a zöld jelzés lézer lövés helyének kijelölése. *b)* a piros jelölések közti fekete folt egy
lézer kráter

unreproducible sampling. The advantages of accurate positioning were studied on thin sections prepared of a drill core of Üveghuta-3 borehole. Since these thin sections (mounted on glass plates) are transparent, the laser source-lens system can be exactly focused on the desired point of measurement. *Figure 21* shows an example for marking out a sampling location in a microcline crystal (green spot). Measurements proved that exact positioning provides repeatable results.

Sometimes during the measurements, we were working with the average spectrum of several repeated laser shots, therefore the penetration depth of subsequent laser shots also had to be taken into consideration. The variation of mineral composition with depth of thin sections (their inhomogeneity) and the penetration of laser shots together predict the possibility of 3-dimensional laser spectroscopy. *Figure 22* presents an example of the

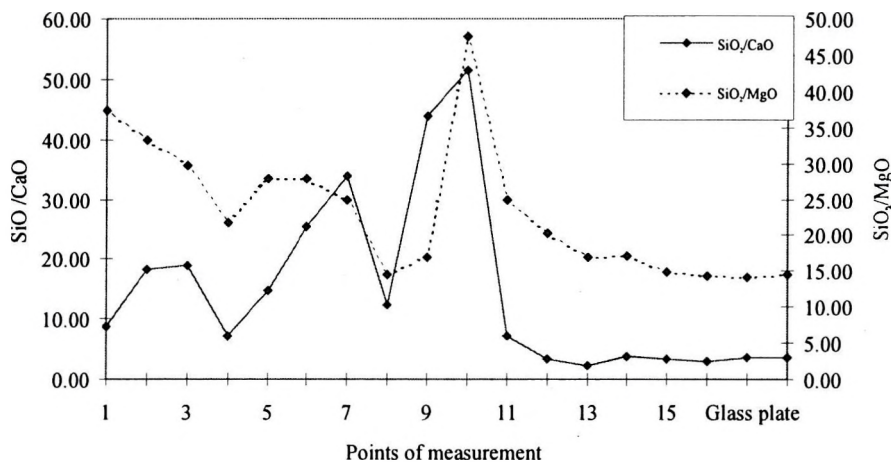


Fig. 22. Depth profiles of SiO₂/CaO and SiO₂/MgO ratios determined by repeated laser shots on a thin slide from a core of Üveghuta-3 borehole

22. ábra. Üveghuta-3 fúrás magminta anyagából készült vékonycsiszolaton ismételt lézer lövésekkel meghatározott SiO₂/CaO és SiO₂/MgO arányok mélységi szelvényei

variation of mineral composition with depth of a thin section. Measurements were carried out by 15 consecutive laser shots at a selected point. From the concentration values determined from emission spectra the SiO₂/CaO and SiO₂/MgO ratios were plotted versus serial number of measurements. Points 16 and 17 show results determined on the glass plate.

Thus it can be stated that the thin section has been penetrated by 12 laser shots. As the thickness of the thin section is 40 μ , the penetration of one laser shot is 3.34 μ .

5.4. Mineral composition of the drill core of Üveghuta–3 borehole

LIPS measurements carried out on drill cores and thin sections provide quick information on mineralogical composition. Deviations between LIPS results and those of petrological analyses derive from the fact that the main minerals forming granites do not occur alone but in mineral associations. These latter dominate the results of laser spectroscopy.

If we create a model of a common granite, the possibility of mineral associations can be included, and the respective element oxide weight percentages computed. These model calculations provide a basis for the quick determination of mineral composition by LIPS measurements on drill cores cut in half and on thin sections. The results of these calculations are given in *Table XXVI*. For the sake of completeness, the values of Na₂O weight percentages are also listed although we cannot detect Na, as its wavelengths of highest amplitudes (588.995 nm and 589.592 nm) are beyond the detection range of our present instrument.

We have carried out LIPS measurements at 5 points of a thin section originating from a drill core of Üveghuta–3 borehole, on a microcline crystal, according to mineralogical analysis. The element oxide concentrations

Mineral composition of common granite	Element oxide concentrations								
	%	Al ₂ O ₃ %	CaO %	FeO %	K ₂ O %	MgO %	Na ₂ O %	SiO ₂ %	TiO ₂ %
Microcline	28.8	5.28	-	-	4.87	-	-	18.65	-
Oligoclase	43.2	11.78	3.92	-	-	-	2.73	24.78	-
Quartz	18.0	-	-	-	-	-	-	18.00	-
Biotite	4	0.43	-	1.03	0.37	0.48	-	1.42	-
Amphibole	4	0.20	0.29	0.17	-	0.16	0.19	2.46	0.31
Titanite	0.5	-	-	-	-	-	-	-	-
Zirkon	0.5	-	-	-	-	-	-	0.16	0.50
Apatite	0.5	-	-	-	-	-	-	-	-
Aleurite	0.5	-	-	-	-	-	-	-	-
Sum	100	17.69	4.21	1.2	5.24	0.64	2.92	65.47	0.81

Table XXVI. Weight percentages of element oxides forming a common granite and also identifiable by LIPS measurements (after Z. Balla)

XXVI. táblázat. Az átlagos gránitot alkotó és a LIPS-mérésekkel is azonosítható elemoxidok súlyszázalékos összetétele (Balla Z. adatai alapján)

Point of measurement	No. of shots	Al ₂ O ₃ %	CaO %	FeO %	K ₂ O %	MgO %	SiO ₂ %	TiO ₂ ppm
Point 1	2	20.65	0.61	1.74	22.81	-	53.99	1845
Point 2	2	8.02	13.29	1.92	14.99	3.320	58.17	2972
Point 3	2	16.52	0.20	2.18	11.53	0.017	69.30	2533
Point 5	2	16.36	0.53	2.49	15.98	0.159	64.05	4384
Point 6	2	14.30	6.78	3.50	13.98	1.570	59.57	2940

Table XXVII. Element oxide concentrations calculated from LIPS measurements carried out on a thin section from Üveghuta-3 borehole

XXVII. táblázat. Az Üveghuta-3 mélyfúrás fűrőmag vékonycsiszolatán elvégzett LIPS-mérésekből számított elemoxid koncentráció értékek

provided by LIPS are presented in *Table XXVII*, by which the following description can be given to complement the mineralogical description:

The high values of K₂O, SiO₂ and Al₂O₃ concentrations and the low values of CaO and MgO at points 1, 3 and 5 show good agreement with the theoretical values of *Table XX/a*, calculated by stoichiometric formulae, thus supporting the presence of microcline. At point 6, the relatively higher concentrations of CaO, FeO and MgO suggest the joint presence of biotite and amphibole.

The concentration values determined at point 2 are ambiguous, absolutely not characteristic of microcline. The anomalous low value of Al₂O₃ and the high values of CaO and MgO concentrations suggest a crack-filling mineral association. As the FeO value is the lowest at this point, the presence of biotite and amphibole cannot be supposed. It is possible that because the thickness of the section is somewhat less at this point, the repeated laser shots reached the glass plate.

Let us compare the element oxide weight percentages determined by LIPS measurements on a vertical section of a drill core of Üveghuta-3 borehole (*Table XXII*) with those of model calculations for a common granite (*Table XXVI*). Analysing the data of *Table XXVIII*, we can see that in the case of Al₂O₃, K₂O and SiO₂ they agree within twice the value of their accuracy. The main carriers of FeO are amphibole and biotite (using the data of Z. Balla), thus the significant deviation between concentrations of FeO and MgO suggests a higher proportion of biotite in the Üveghuta granite than that of the common granite model.

	Al ₂ O ₃ %	CaO %	FeO %	K ₂ O %	MgO %	Na ₂ O %	SiO ₂ %	TiO ₂ %
LIPS Mean	16.05	6.43	4.58	5.71	4.17	-	61.91	1.14
Δc	± 1.15	± 0.40	± 0.40	± 0.25	± 0.30	-	± 2.70	± 0.08
Common granite	17.69	4.21	1.2	5.24	0.64	2.92	65.47	0.81
Deviation	-1.64	+2.22	+3.38	+0.47	+3.53	-	-3.56	+0.33

Table XXVIII. Comparison between weight percentages of element oxides determined by LIPS measurements along a profile of a drill core cut in half (Table XXII) of Üveghuta-3 borehole and that of a common granite (Table XXVI)

XXVIII. táblázat. Összehasonlítás az Üveghuta-3 fúrásból származó félbevágott fűrőmagon szelvénymenti LIPS-mérésekből számított (XXII. táblázat) és az átlagos gránitot alkotó (XXVI. táblázat) elemoxidok súlysúlyszázalékos arányai között

Lastly we can report on the comparison of LIPS measurements on a drill core cut in half with measurements on a pulverized samples of the same core. Table XXIX. comprises the element oxide concentrations of two randomly selected points of both the core and the pulverized sample. Accuracy (Δc) was calculated only for the first row. These results should be regarded as pilot experiments which did not take into consideration several factors influencing concentrations, first of all rock physical parameters such as density, porosity (moisture content), etc. The deviations, however, are greater than could be produced by these factors, therefore we consider that the mineral composition at the points of measurement must have been different.

Point of measurement	Al ₂ O ₃ %	CaO %	FeO %	K ₂ O %	MgO %	SiO ₂ %	TiO ₂ %
Core 1	16.59	4.02	4.58	4.43	4.37	64.15	1.741
Core 2	18.05	1.69	5.83	2.61	5.22	65.85	0.652
Pulver. 1	20.15	11.20	3.97	7.50	3.50	52.24	0.396
Pulver. 2	18.34	6.13	4.64	10.55	3.79	55.04	0.368
Δc	± 1.15	± 0.27	± 0.40	± 0.25	± 0.30	± 2.70	± 0.08

Table XXIX. Comparison of element oxide concentrations determined by LIPS measurements on cores with pulverized samples of the same cores

XXIX. táblázat. Az Üveghuta-3 fúrás maganyagán és az abból készített porított mintán elvégzett LIPS-mérésekből számított elemoxid koncentráció értékek

6. Conclusions

Although laser-induced plasma atom emission spectroscopy has proved its usefulness for rapidly determining the elemental composition (and that of element oxides, decisive in mineral identification) of rock samples, and — for some elements — even their concentration, there are several problems to solve.

Let us discuss these problems in two groups: theoretical and practical. In the first group we can list all those tasks we have to solve to make the method more accurate and reliable. These are:

- We have to learn much more of the physical processes taking place in the sample as a result of a laser shot, e.g. heating and melting, reflection and absorption parameters of the sample, etc.
- We have to find a mathematical solution for calculating the volume of vaporized material related to the geometrical parameters of the craters.

In terms of practical solutions

- We have to study those effects which may influence the accuracy of measurements, e.g. measurement geometry, rock matrix, porosity, and by introducing a matrix correction function for each elemental species increase the reliability of the method.
- The standard series at our disposal is not suitable for calibrating toxic elements important for environmental protection. By developing standard series for further matrix- (Mn, Na) and toxic elements (Cd, Cr, Ni, Mo), and determining their calibration functions, the method may develop into an important tool in environmental protection.
- To make the method also applicable for determining elements of low concentration, the signal-to-noise ratio has to be increased. In this respect the use of second derivatives is promising.
- In carrying out the measurements on drill cores, the most important task is to develop a positioning device and with it sampling in geometrically well defined, two perpendicular directions.

In that a rapid field method is a necessity for determining the mineral composition of rocks, it is to be hoped that funding for continuing the development along the above lines will be forthcoming.

Acknowledgements

We should like to express our thanks to all those who assisted us in our work, first of all to A. Bartha and R. Horváth for the laboratory analyses and the creation of standards, and to Gy. Maros for providing the rock samples and investigating the thin sections. Our thanks also go to F. Fenesi whose contribution was indispensable in preparing the standards and samples for our experiments.

We owe a debt of gratitude to the following institutions for their financial support in relation to the publication of our results:

- Pro Renovanda Cultura Hungariae Foundation
- Eötvös Loránd Geophysical Foundation
- Geo-Log Environmental and Geophysical Limited.

REFERENCES

- ANDRÁSSY L., KOZMA L., LENDVAY P., LUPKOVICS G., NÉMET B. 1993: Real time in situ application of the laser-induced plasma spectrometry. The field mode laser spectrometer LIPS-1-60. SPIE Vol. Optics as a Key to High Technology 1993/1005
- ANDRÁSSY L., LENDVAY P., LUPKOVICS G., KOZMA L., NÉMET B. 1995/a: Application possibilities of the laser-induced plasma atomic emission spectroscopy in geological prospecting and in environmental research (in Hungarian with English abstract). *Magyar Geofizika*, **36**, 1. pp. 68–74
- ANDRÁSSY L., MARA J., LUPKOVICS G., MOLNÁR G., VIHAR L. 1995/b: The portable laser-induced plasma spectrometer (in Hungarian with English abstract). *Magyar Geofizika*, **36**, 3. pp. 222–231
- ANDRÁSSY L., NÉMET B., VIHAR L. 1998: Theoretical and practical problems of the application of laser-induced plasma emission spectroscopy in geological prospecting. *OPTIKA '98* 5th Congress on Modern Optics. Proceedings of SPIE. Vol. 3573. pp. 343–346
- BÁRDOSSY Gy. 1997: Geomathematical problems as seen by a geologist (in Hungarian). *Magyar Geofizika*, **38**, 2. pp. 124–141
- BUDA Gy., PUSKÁS Z. 1997: Crystalline rocks of Üveghuta-1 borehole (in Hungarian). Annual Report of Hung. Geol. Inst. (MÁFI) 1996/II. pp. 95–98
- CHINNI R. C., CREMERS D. A., FERRIS M. J. 1998: The detection of contaminants on surface using a portable instrument based on laser-induced breakdown spectroscopy (LIBS). Winter Conference on Plasma Spectrochemistry, Scottsdale, Arizona, January 5-10. 1998. p. 186
- DEER W. A., HOWIE R. A., ZUSSMANN J. 1963: Rock-forming minerals. Vol. 4: Silicates. Longmans
- HARRISON G. R. 1980: Wavelength Tables. John Wiley and Sons, New York

- KWANG B. H. 1989: Application of laser-induced fluorescence for determination of trace uranium, europium and samarium. *Talanta*, **36**, 11. pp. 1095–1099
- MIKHAIL E. M., GRACIE G. 1981: Analysis and adjustment of survey measurements. Van Nostrand Reinhold Co. New York. 340 p.
- MOENKE L., JAHN K., BRÜGMAN L. 1989: Laser-micro-analytical studies on distribution pattern of manganese, iron and barium in Fe/Mn-accumulates of the Western Baltic Sea. *Chem. Erde* **49**, pp. 39–46
- PINI R. C. 1999: Laser sampler takes aim at Mars. *Photonics Technology World*. June 1999.
- VINCZE I. 1975: Mathematical statistics with industrial applications (in Hungarian). Műszaki Könyvkiadó, Budapest
- YAMAMOTO K. Y., CREMERS D. A., FERRIS M. J., FOSTER L. E. 1996: Detection of metals in the environment using a portable laser-induced breakdown spectroscopy instrument. *Applied Spectroscopy* Vol. 2. pp. 222–232

Geológiai mintákon mért lézer-indukált plazma atom emissziós spektrumokból számított elem koncentráció eloszlások elméleti és statisztikai vizsgálata

ANDRÁSSY László, ZILAHÍ-SEBESS László, VIHAR Levente

A lézer-indukált plazma spektroszkópia (LIPS) földtani alkalmazásának témaköréből a fűrőmagok (porított minták) ásványos összetételének és az ásványok (szemcsék) eloszlásából adódó inhomogenitások vizsgálata volt a három éves kutatási időszak fő feladata. A feladatok megoldásához elméleti modellszámításokat, és a LIPS mérőberendezéssel a kiválasztott mintákon kísérleti méréseket végeztünk. Statisztikai módszereket alkalmaztunk a mért spektrumok segítségével kiszámított csúcsmplitúdó és elem (elemoxid) koncentráció értékek eloszlásainak vizsgálatára. A koncentráció értékek meghatározása a kísérleti hitelesítő sor egyes etalon mintáin elvégzett LIPS mérések és a laboratóriumi indukált plazma atom emissziós spektroszkópiái (ICP AES) mérések eredményeinek ismeretében kiszámított kalibrációs függvények segítségével történt. A kalibrációs függvényekben szereplő paramétereket a vizsgált elemekre jellemző leg-erősebb spektrumvonalak csúcsmplitúdó (2. derivált amplitúdó) értékeinek ismeretében számítottuk ki. Az amplitúdó értékeket a szelvény menti (laza hálózati) mintavétellel és a mintavételi sűrűség értékekkel jellemzett mintavételi stratégia mellett kijelölt mérési pontokban egy (vagy több) lézer-lövessel gerjesztett emissziós spektrumok (átlag spektrumok) segítségével határoztuk meg. Statisztikai számításokat végeztünk az elem koncentráció értékek pontosságának meghatározására. Hipotézis vizsgálatokkal, és intervallumbecslésekkel a LIPS mérőműszer stabilitását és megbízható működését vizsgáltuk.

Egymással párhuzamos szelvénymérések eredményei alapján megszerkesztett fűrőmag térképek segítségével meghatároztuk az egyes elemek (elemoxidok) koncentráció értékeinek felületi eloszlását. A vékonyecsiszolatokon elvégzett pozicionált mérések segítségével több lézer lövés esetén a behatolási mélységet és az ásványos összetétel mélységi változásait tanulmányoztuk.

ABOUT THE AUTHORS



László Andrásy is a senior scientific researcher who graduated as a geophysical engineer from Miskolc Technical University of Heavy Industry (1960), which university also awarded him his doctorate (1975). He has been with ELGI since 1960, spending the first few years with well logging measurements and evaluation.

From 1968 to 1989 his research included further developing nuclear well logging; elaborating a system model for calibrating and testing measuring instrumentation; modelling neutron-fields by multi-group-diffusion and Monte-Carlo calculations for a given set of neutron sonde parameters and bore-hole geometry; developing equipment for measuring, 'in-situ', the

physical parameters of neutrons. Between 1984 and 1989 he founded and headed the Hungarian Metrological Station for Geophysical Well Logging and was involved in calibrating several kinds of probes (acoustic, induction and nuclear). Within the framework of Hungarian-Greek Bilateral Inter-governmental Scientific and Technological Co-operation, between 1990 and 1997 he was concerned with density and porosity model calibrations of geophysical well logging instruments.

The year 1992 saw him launching research on the application possibilities of laser induced plasma atomic emission spectrometry in geological prospecting and environmental research, and in developing a prototype of a portable laser-induced plasma spectrometer (LIPS).

His publications number more than thirty, including seven university lecture notes, and five inter-governmental research reports.

László Zilahi-Sebess for a photograph and biography, see this issue, p. 92.



Levente Vihar is the design & development manager of OpLab Ltd. He received his MSEE degree from the Technical University of Budapest in 1983. From 1983 to 1995 he worked as a design engineer for the Hungarian Optical Works, focusing on photometers, peripheral devices, etc. In 1995 he co-founded the OpLab Ltd.

Hobbies include amateur astronomy, fishing, philately.

Copyright

Authorization to photocopy items for internal or personal use in research, study or teaching is granted by the Eötvös Loránd Geophysical Institute of Hungary for individuals, instructors, libraries or other non- commercial organizations. We permit abstracting services to use the abstracts of our journal articles without fee in the preparation of their services. Other kinds of copying, such as copying for general distribution, for advertising or promotional purposes, for creating new collective works, or for resale are not permitted. Special requests should be addressed to the Editor. There is no charge for using figures, tables and short quotes from this journal for re-publication in scientific books and journals, but the material must be cited appropriately, indicating its source.

Az Eötvös Loránd Geofizikai Intézet hozzájárul ahhoz, hogy kiadványainak anyagáról belső vagy személyes felhasználásra kutatási vagy oktatási célokra magánszemélyek, oktatók, könyvtárak vagy egyéb, nem kereskedelmi szervezetek másolatokat készítsenek. Engedélyezzük a megjelentetett cikkek összefoglalóinak felhasználását referátumok összeállításában. Egyéb célú másoláshoz, mint például: terjesztés, hirdetési vagy reklám célok, új, összefoglaló jellegű anyagok összeállítása, eladás, nem járunk hozzá. Az egyedi kéréseket kérjük a szerkesztőnek címezni. Nem számolunk fel díjat a kiadványainkban szereplő ábrák, táblázatok, rövid idézetek más tudományos cikkben vagy könyvben való újrafelhasználásáért, de az idézés pontosságát és a forrás megjelölését megkivánjuk.

